

---

# Numerical Simulations of low-level convergence Lines over north-eastern Australia

Gerald Ludwig Thomsen

---



Munich 2006



---

# **Numerical Simulations of low-level convergence Lines over north-eastern Australia**

**Gerald Ludwig Thomsen**

---

Dissertation  
at the Faculty of Physics  
Ludwig-Maximilians-University  
Munich

by  
Gerald Ludwig Thomsen  
from Reinbek

Munich, 02 June 2006

First Examiner: Prof. Dr. Roger K. Smith  
Second Examiner: Prof. Dr. Ulrich Schumann  
Date of the oral examination: 28 July 2006

# Zusammenfassung

Im Gebiet des Carpentaria Golfes im Norden Australiens entstehen regelmäßig mesoskalige Konvergenzlinien in der unteren Troposphäre. Diese produzieren gegen Ende der Trockenzeit oft spektakulären Wolkenlinien, die auf Satellitenbildern zu sehen sind und je nach ihren Eigenschaften "Morning Glory" oder "North Australian Cloud Line" (NACL) genannt werden. Morning Glories sind glatte Wellenwolken während NACLs konvektive Wolkenlinien sind. Sie stehen unter dem Verdacht, später im Jahr, während der Australische Sommermonsun ruht, eine Reihe von Unwettern auszulösen, die ein bedeutendes Vorhersageproblem für diese Region darstellen. Des Weiteren stellt die einhergehende bodennahe Windscherung eine große Gefahr für tieffliegende Flugzeuge dar. Um die Entstehung dieser Konvergenzlinien mit bis dahin einmaliger Genauigkeit zu dokumentieren, wurde im Herbst 2002 die internationale Meßkampagne GLEX (Gulf Lines Experiment) durchgeführt. Das mesoskalige Modell der Pennsylvania State University und des National Center for Atmospheric Research, MM5, wird in dieser Arbeit für eine Untersuchung dieser Linien benutzt. Da die Linien intrinsisch nicht hydrostatisch sind, sollte das MM5 bei der geforderten hohen horizontalen Auflösung als nichthydrostatisches Modell in Vorhersage und Modellierung den für frühere Studien verwendeten hydrostatisch balancierten Modellen überlegen sein.

Den zunächst vorgestellten Fallstudien gingen Sensitivitätsstudien bezüglich der Grenzschichtparameterisierung und der Bodenfeuchte voraus, die aber aus Gründen der Lesbarkeit erst später beschrieben werden. Im Rahmen der Fallstudien werden Modellergebnisse mit Ergebnissen aus der Meßkampagne und verfügbaren Satellitenbildern verglichen, sowie weitere Charakteristika der sich bildenden Linien untersucht. Das Modell kann in der gewählten Konfiguration die Konvergenzlinien in noch nie da gewesener Detailliertheit reproduzieren und die Ergebnisse stimmen gut mit den Beobachtungen überein. Weitere Ergebnisse dieser Studie bestätigen früher aufgestellte Theorien, nach denen das nordöstliche Morning Glory und die NACL in Folge eines Zusammenstoßes zweier Seebriesen über der Kap York Halbinsel entstehen. Zum ersten Mal hat ein Modell zwei getrennte Konvergenzlinien produziert, die dem nordöstlichen Morning Glory und der NACL entsprechen. Als Trennungsmechanismus beider sich aus der Ostküstenseebriese entwickelnden Konvergenzlinien wird hier zunächst die Geometrie der Ostküste vorgeschlagen, die auf dem Breitengrad, auf dem die Trennung im allgemeinen erfolgt, einen ausgeprägten Knick aufweist. Für die Entstehung des südlichen Morning Glorys wird eine erst kürzlich aufgestellte Theorie bestätigt, in der die Kollision der südlichen Seebriese mit einer sich von Süden her nähernden Front als Mechanismus angenommen wird. Diese Front formiert sich am Abend entlang einer Troglinie, die ein klimatisches Merkmal Queenslands ist. In einigen der Fälle wurden Trockenlini-

en beobachtet, die auf das südliche Morning Glory folgten. Auch diese stimmen im Modell gut mit den Beobachtungen überein. Eines der seltener beobachteten südöstlichen Morning Glories kann leider nicht vom Modell reproduziert werden. Als Ursache wird vermutet, daß eine Troglinie im datenarmen Gebiet südlich des Golfs von Carpentaria nicht korrekt in den Anfangsbedingungen positioniert ist. Eine Untersuchung der Strömung hinter den Konvergenzlinien zeigt, daß Morning Glories Wellenphänomene sind. NACLs hingegen behalten den Dichteströmungscharakter der Seebriese bei.

Eine Sensitivitätsstudie bezüglich der Grenzschichtparameterisierung wird durchgeführt, weil sich die hier untersuchten Phänomene in der planetaren Grenzschicht abspielen. Eine Gruppe von Parameterisierungen stellt sich anderen als überlegen heraus und als Grund für diese guten Ergebnisse wird die Berücksichtigung der großräumigen Gradienten identifiziert, die in den schlechter abschneidenden Parameterisierungen fehlt. Als beste Parametrisierung wird das MRF Schema für alle weiteren Simulationen ausgewählt.

Eine Untersuchung der Sensitivität der Ergebnisse bezüglich der Bodenfeuchte zeigt, daß die Seebriesen um so schneller landeinwärts strömen, je trockener die Bodenverhältnisse sind. Die Erklärung hierfür ist, daß ein größerer Teil der eingehenden solaren Strahlung als fühlbare Wärme an die Atmosphäre abgegeben wird und so die Seebriesenzirkulation antreibt. Daraus resultiert, daß Morning-Glory Konvergenzlinien sowohl intensiver sind, als auch die Fortpflanzungsgeschwindigkeit größer ist wenn die Bodenfeuchte abnimmt. Ein solcher Zusammenhang konnte für die NACLs nicht bestimmt werden. Eine optimale Bodenfeuchte, mit der die Modelergebnisse am besten mit den Beobachtungen übereinstimmen, kann leider nicht ermittelt werden, da geeignete Methoden hierfür nicht zur Verfügung stehen. Die Güte der Ergebnisse bezogen auf die Boden- druck an den einzelnen Stationen des Experiments nimmt jedoch mit abnehmender Bodenfeuchte zu. Da aber die geringst möglichen Werte unrealistisch sind beziehungsweise keinen physikalischen Sinn haben und keine Meßdaten vorhanden sind, wird für alle weiteren Simulationen ein Wert für die Bodenfeuchte gewählt, wie er vom Australischen Wetterdienst benutzt wird.

Um einige der aufgezeigten Zusammenhänge noch gründlicher zu untersuchen, wurden noch einige Modellexperimente mit modifizierter Orographie durchgeführt. Diese zeigen, daß weder Morning Glories noch NACLs entstehen, wenn keine Seebriese vom Golf von Carpentaria landeinwärts strömt und mit der Ostküstenseebriese beziehungsweise der sich von Süden her nähernden Kaltfront kollidiert. Ein systematischer Zusammenhang zwischen Höhe der Orographie und der Intensität oder der Geschwindigkeit der sich bildenden Konvergenzlinien kann nicht festgestellt werden. Die im Rahmen der Fallstudie aufgestellte Hypothese für die Trennungsursache von NACL und nordöstlichem Morning Glory kann nicht bestätigt werden und die horizontale Windscherung über der Kap York Halbinsel wird stattdessen als Ursache vorgeschlagen. Diese Hypothese wird durch die Ergebnisse eines Experiments mit unformer Strömung in westlicher Richtung bestätigt. In diesem Experiment bildet sich nur eine Konvergenzlinie, die dem nordöstlichen Morning Glory entspricht und weit in das Gebiet hineinragt, in dem sich die NACL normalerweise befindet. Am zweiten Tag dieser Simulation entwickelt sich eine horizontale Windscherung, in der sich zwei unabhängige Konvergenzlinien bilden, die dem nordöstlichen Morning Glory und der NACL entsprechen.

# Contents

<b>1</b>	<b>Introduction</b>	<b>1</b>
1.1	Background and motivation . . . . .	1
1.2	Analytical modelling studies . . . . .	8
1.3	Numerical modelling studies . . . . .	8
1.4	Description of the MM5 model . . . . .	10
1.5	General model configuration . . . . .	13
<b>2</b>	<b>Case studies</b>	<b>15</b>
2.1	Five major events . . . . .	15
2.2	Model setup . . . . .	16
2.2.1	MesoLAPS simulations . . . . .	16
2.2.2	Medium resolution simulations, BOM . . . . .	16
2.3	03-04 October . . . . .	17
2.4	28-29 September . . . . .	34
2.5	08-09 October . . . . .	45
2.6	09-10 September . . . . .	57
2.7	29-30 September . . . . .	67
2.8	Summary . . . . .	73
<b>3</b>	<b>Sensitivity to boundary layer schemes</b>	<b>75</b>
3.1	Model configuration and experiments . . . . .	75
3.2	Land-surface schemes in MM5 . . . . .	77
3.3	Boundary layer schemes in MM5 . . . . .	78
3.3.1	Explicit . . . . .	78
3.3.2	Blackadar . . . . .	80
3.3.3	Mellor-Yamada-based schemes . . . . .	84
3.3.4	MRF . . . . .	89
3.4	Summary . . . . .	91
<b>4</b>	<b>Sensitivity to soil moisture</b>	<b>93</b>
4.1	The relevance of soil moisture in the Gulf of Carpentaria region . . . . .	93
4.2	Soil moisture treatment in the ECMWF model and in MM5 . . . . .	93
4.3	Model configuration and experiments . . . . .	94

4.4	Soil moisture impacts on the low-level convergence lines . . . . .	96
4.5	Finding the "optimum" soil moisture value . . . . .	102
4.6	Summary . . . . .	104
<b>5</b>	<b>The role of orography</b>	<b>105</b>
5.1	Motivation . . . . .	105
5.2	Model configuration and experiments . . . . .	105
5.3	The impact of the orography surrounding Mt. Isa and the Great Dividing Range	108
5.4	The impact of the Gulf of Carpentaria . . . . .	111
5.5	The impact of the shape of Cape York Peninsula . . . . .	113
5.6	Summary . . . . .	122
<b>6</b>	<b>Summary and conclusions</b>	<b>123</b>
<b>A</b>	<b>List of symbols</b>	<b>126</b>
<b>B</b>	<b>Table of <math>\sigma</math>-levels</b>	<b>128</b>
<b>C</b>	<b>Modified orography with MM5 and its preprocessors</b>	<b>130</b>

# Chapter 1

## Introduction

### 1.1 Background and motivation

One of the most spectacular atmospheric phenomena in northern Australia is the so-called "morning glory", the name given to a low-level roll cloud line or a series of such lines that occur early in the morning over the south-eastern part of the Gulf of Carpentaria and adjacent seaboard. These roll cloud formations often extend from horizon to horizon in a long arc as far as the eye can see. While the leading line is usually smooth, the subsequent lines are rather turbulent and often appear as scattered lines of inhomogeneous cumulus. The clouds are usually about 1000 m in depth with a base at about 400 m above ground level. The extent in length often exceeds 500 km and a typical width is around 4 km. In well-developed disturbances the horizontal separation between the leading cloud lines is typically between 3 and 14 km. Their typical propagation speed is between 5 m/s and 18 m/s (Christie 1989). Despite the foreboding appearance of the cloud formations, they seldom produce measurable precipitation, but they are always accompanied by an often intense, but transient wind gust which poses a serious threat to aircraft that may be landing or taking off. Morning glories are most frequently observed in the late dry season, typically from mid-September until the end of October. Morning glories have to date been observed to propagate into three main directions.

The most common cloud lines in the Gulf of Carpentaria region have a north-west to south-east orientation and move from the north-east: I refer to these as north-easterly morning glories. A closely related phenomenon is the North Australian Cloud Line (NACL), a long line of convective cloud that forms along the west-coast of the Cape York Peninsula in the late afternoon or early evening and moves westwards over the gulf during the night and the following day. A comprehensive list of references for both phenomena is contained in the review article by Reeder and Smith (1998). During breaks in the wet season, when easterly flow is temporarily re-established over the peninsula and when there is high moisture at low levels, the NACL may develop into a line of thunderstorms that

pose a significant forecasting problem to the gulf region.

A second and less common morning glory develops overnight to the south of the gulf or over the gulf, itself, and moves northward, or at least with a significant northwards component. The generation of these so-called southerly morning glories is less well understood than that of their north-easterly counterparts, but many appear to be associated with strong ridging to the south of the inland heat trough (Smith *et al.* 1982, 1985, 2005). This trough is a climatological feature of the region of north-western Queensland late in the year when morning glories are most common. These disturbances are discussed also in the review article by Reeder and Smith (1998) and the disturbances documented during GLEX are discussed by Smith *et al.* (2005).

The third and by far the least frequently observed occurring morning glory is the one approaching from the south-east. The origin of south-easterly morning glories are not yet understood, but assumed generation mechanisms are linked to the Great Dividing Range (Reeder *et al.* 1995) which is located along the east-coast of the continent.

Figure 1.1 shows the Japanese Geostationary Meteorological Satellite (GMS) image for the gulf region at 0630 EST on 04 October 2002. The positions of a southerly and a north-easterly morning glory and an NACL are indicated by arrows. Figure 1.2 shows a photograph of the north-easterly morning glory taken at Karumba on this day.

The morning glory cloud lines are the visible manifestation of large-amplitude, long nonlinear internal-boundary-layer wave disturbances which evolve asymptotically in time into a family of large amplitude solitary waves. Disturbances of this kind usually form on the low-level inversion. An extensive survey by Miles (1980) describes a solitary wave as a gravity wave consisting of a single elevation of finite amplitude that propagates without change of form. Its existence is a result of a balance between nonlinearity, which tends to steepen the wave front in consequence of the increase of wave speed with amplitude, and dispersion, which tends to spread the wave front as the wave speed of spectral components decreases with increasing wavenumber. Most extensively studied are solitary waves on the free surface of water, but there exist also internal solitary waves, as the balance between nonlinearity and dispersion may be possible in the absence of a free surface by virtue of any or all of stratification, shear, compressibility, and rotation. When the air is moist enough, clouds form at the crest of the waves. The upward motion at the leading edge and the downward motion at the trailing edge lead to the false impression that the cloud lines roll backwards as they advance, but this is not the case. The air parcels at the leading edge of a wave are lifted above their condensation level and form cloud. At the trailing edge, where subsidence prevails, the clouds evaporate as the air parcels move below their level of condensation. The narrow bands of ascent/descent at the edges of the waves correspond to horizontal convergence/divergence of the wind-field and I will henceforth use the term convergence line to describe morning glory and NACL phenomena in the model, either where marked by cloud lines or not. The terms morning glory and NACL always refer to

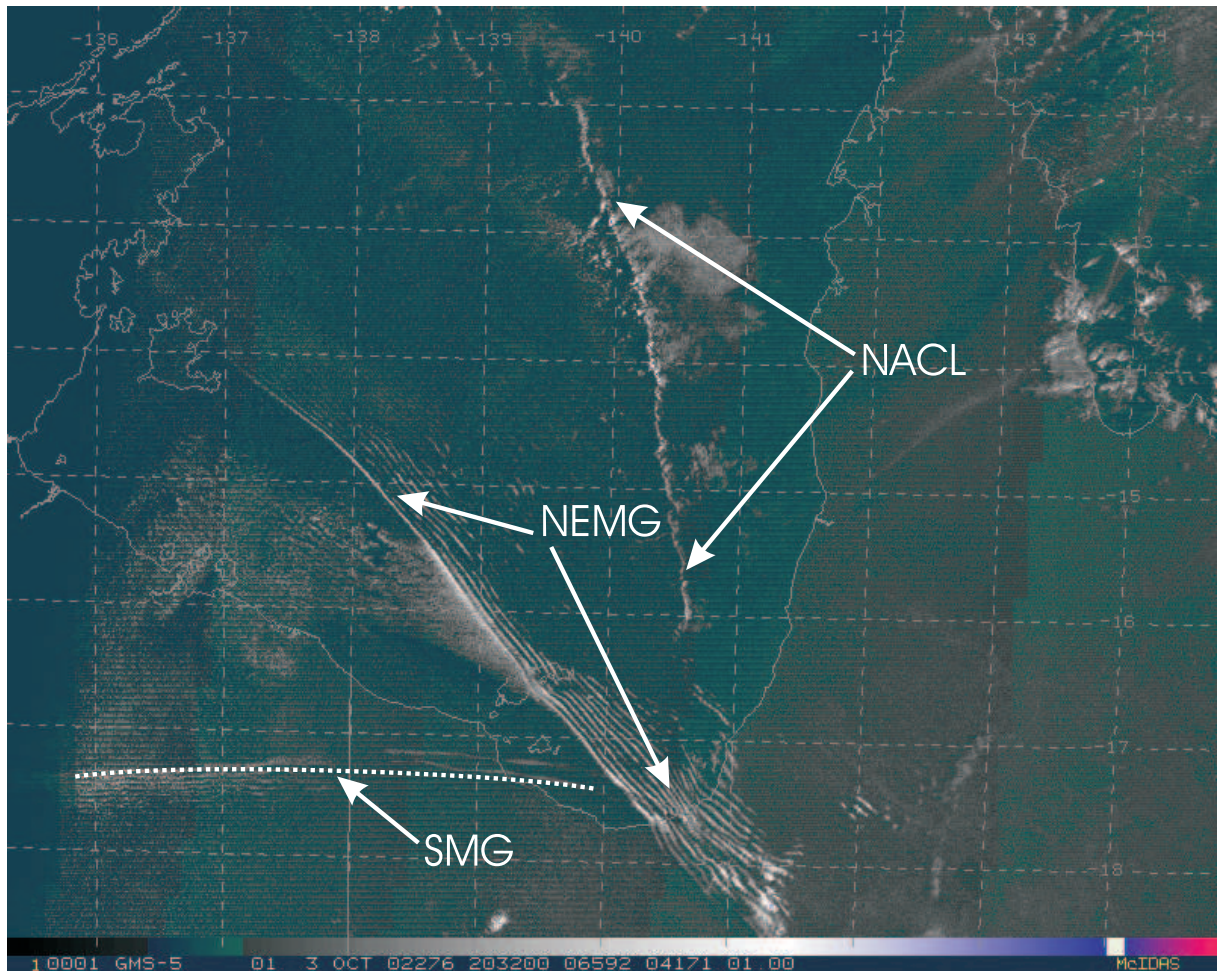


Figure 1.1: GMS visible image of the Gulf of Carpentaria region at 0632 EST on 04 October 2002. The north-easterly morning glory (NEMG), the southerly morning glory (SMG) and the North Australian Cloud Line (NACL) are indicated by arrows, the leading cloud line of the southerly morning glory is highlighted by a dashed line.

observed cloud lines. The formation mechanism for these convergence lines is the collision of two dense layers of air. I will show that in case of the north-easterly morning glory and the NACL, these layers are the east-coast and west-coast sea breeze which collide over the Cape York Peninsula in the early afternoon. I will show also that in case of the southerly morning glory the two dense layers are the sea breeze approaching from the north and cold front approaching from the south.

A first attempt to determine the predictability of the low-level convergence lines over the gulf is described by Jackson *et al.* (2001) using the mesoscale version (mesoLAPS) of the Limited Area Prediction System (LAPS) of the Australian Bureau of Meteorology,



Figure 1.2: Photograph of a north-easterly morning glory at Karumba in the morning of 04 October 2002. Courtesy of Roger K. Smith.

which is described by Puri *et al.* (1998). Events were chosen on occasions when cloud lines of various types were clearly visible in satellite imagery and verification was based on the prediction of a low-level convergence line in the observed location and with the observed orientation of the cloud line. However, no other data were available for verification.

The GLEX experiment was carried out for a period in September-October 2002 in order to remedy the deficiency in the data base and to document the occurrence and evolution of the convergence lines in as much detail as possible. To this end a network of automatic weather stations (AWS) was installed in the region and an instrumented light aircraft was used to make measurements of lines over the sea. Details of the experiment and the results thereof are described in a series of papers by Goler *et al.* (2006), Smith *et al.* (2006) and Weinzierl *et al.* (2006).

The next step in researching these phenomena presented in this study starts with high-

resolution numerical simulations of selected cases during the GLEX experiment (Chapter 2) and is followed by studies of the sensitivity to the different boundary layer parameterisations (Chapter 3), to the soil moisture (Chapter 4) and to the orography (Chapter 5). By doing this, the generation mechanisms and propagation of the lines can be determined. The order of the chapters does not reflect the order of the numerical experiments and has been chosen for a better readability. The measurements taken during the GLEX experiment are used to verify the results of the model. The hydrostatic mesoscale model of the Australian Bureau of Meteorology has certain disadvantages at the required high resolutions in this study, as there are good reasons for choosing a non-hydrostatic model. The first reason is that the undular disturbances which are analysed here are intrinsically non-hydrostatic. The second reason is that the interaction between orography and atmosphere is incompletely represented at small scales by a hydrostatically-balanced model, which is an important point as the role of the orography will be investigated also. The calculations presented in this study are carried out using the nonhydrostatically-balanced numerical mesoscale model of the Pennsylvania State University and the National Center for Atmospheric Research (NCAR), MM5. For some of the case studies, results from meso-LAPS were available also and I present comparisons between the two models were possible.

Studying the morning glory and the NACL is relevant to aviation safety because of the immediate hazards of the morning glory, and a major importance is to understand these lines in a dry environment before doing the next step and studying the lines during the wet season, in which the NACL is known to trigger severe convection. Experiments in order to gather data for cases during the wet season have been carried out as the second part of the GLEX experiment in the end of 2005.

Although similar phenomena occur in different parts of the world (see figures 1.3 to 1.5), for example in the lee of orography (the Rocky Mountains for example), there is no other place on earth besides the Gulf of Carpentaria region in which these convergence lines occur in this degree of regularity (almost daily), and so providing the ideal "laboratory" for experiments. Findings from this research will help forecasters both in Australia and elsewhere both to understand and to forecast the convergence lines. Reports of cloud lines similar to the morning glory over southern Australia have been given, *inter alia*, by Clarke (1986) and a few noteworthy observations in other parts of the world include the 'fog waves' over Berlin (Egger, 1985) and the wave disturbance which occurred over southern England in 1914 (Geophysical Memoirs 1914). Figures 1.3 to 1.5 show further examples.



Figure 1.3: On June 13, 2003, in late afternoon, a morning glory appeared in the otherwise blue sky over the ocean east of Sable Island. At about 1600 local time, the cloud line, oriented roughly north-west to south-east, was located near the east tip of the island ( $44^{\circ} 03' \text{ N}$ ;  $59^{\circ} 38' \text{ W}$ ). Courtesy of the Sable Island Green Horse Society.



Figure 1.4: Morning glory near Nysted, Danmark. Courtesy of the European Meteorological Calendar 2005.

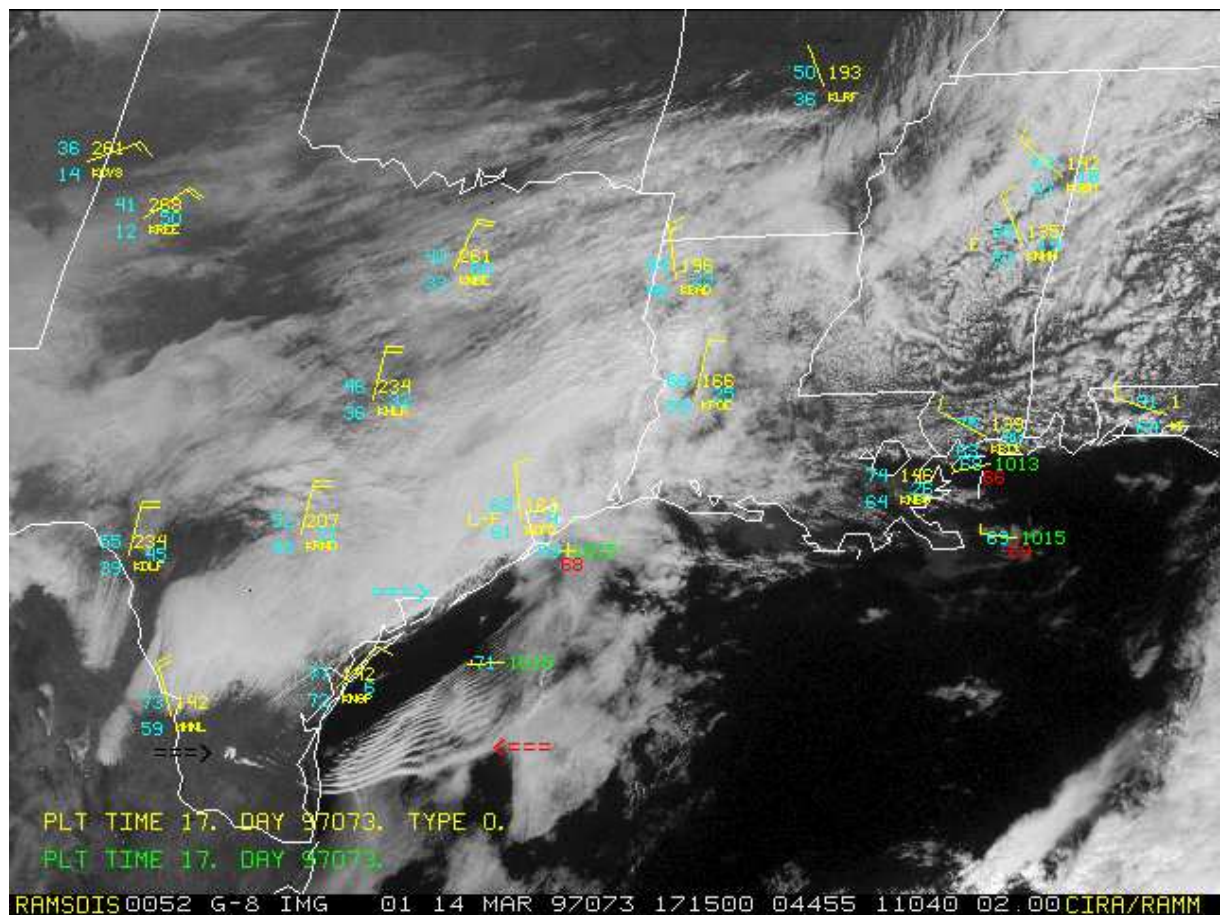


Figure 1.5: The visible satellite image from 14 March 1997 at 1715 UTC shows a morning glory south of the coast of Texas (indicated by a red arrow). On this day a cold front was moving through Texas. The front can be identified as the narrow cloud band which parallels the coast (marked by light blue arrow). Courtesy of the CIRA/RAMM Team Daily Satellite Discussion.

## 1.2 Analytical modelling studies

Considerable efforts have been made during the past years to describe morning glory waves analytically. I just want to describe a few of them briefly here. A comprehensive survey is given by Christie (1989).

A study by Noonan and Smith (1985) showed that linear long wave theory can be made to agree well with the observed wave speed, but only because there is uncertainty in the depth of the stable layer. Egger (1983, 1984) applied the internal bore-wave solutions of the classical shallow-fluid Korteweg-de Vries(KdV)-Burgers equation to analyse the development of the morning glory in a simple two-fluid model. He assumed that horizontal wave lengths are comparable to the height of the troposphere. Though this assumption is not valid for morning glories, the solutions describe the evolution of the waves and their speeds, but not their half-widths, reasonably well. Approaches with the more suitable assumption that the morning-glory disturbance is a wave propagating on a statically-stable shallow layer embedded in a much deeper homogeneous fluid apply the Benjamin-Davis-Ono (BDO) equation in the case where friction is neglected and the BDO-Burgers equation when turbulent dissipation is significant (see Christie, 1989). Assumptions tested with both equations range from long waves of finite amplitude to internal deep-fluid bore waves of infinite spatial extent. Results of these theories describe the evolution of the waves quite well, producing wave speeds which agree reasonably with the observations.

However, both KdV and BDO approaches have the shortcoming of producing wave half-widths which do not closely agree with observations, being too small by a factor of between two and three. By applying the (orographically) forced BDO equation, Porter and Smyth (2002) argued that orographic forcing was an important aspect for the formation of morning-glory waves, a thesis which is not supported by the results of this study (see Chapter 5).

## 1.3 Numerical modelling studies

Prior to the work by Noonan and Smith (1987), all numerical studies of the morning glory or NACL were two-dimensional. These studies can be divided into two groups.

The first group investigated the development and subsequent collision of two sea breezes explicitly. Clarke's model (1983) was based on the formulation of Smagorinsky *et. al.* (1965). This model was hydrostatically-balanced and anelastic. It accounted for solar radiation and for fluxes of heat and moisture at the surface and was formulated in  $\sigma$ -coordinates to allow for orography. The horizontal resolution was 5-10 km. The model used by Noonan and Smith (1986) was a two-dimensional version of one developed by Pielke

and described by McNider and Pielke (1981). It was a dry, hydrostatic, primitive equation model formulated on terrain-following height coordinates with 10 km grid spacing. Since the horizontal resolutions were too coarse and the models were hydrostatically-balanced, numerical experiments with both Clarke's and Noonan and Smith's models have produced broad-scale propagating convergence lines rather than waves corresponding to a morning-glory. Using a nonhydrostatic two-dimensional model first described by Clark (1977) and applying a very high horizontal resolution (200 m), Goler and Reeder (2004) were the first ones who modeled the generation of morning-glory waves explicitly.

The second group of models includes the studies of Crook and Miller (1985), Crook (1986,1988), Haase and Smith (1989) and Skyllingstad (1991). Though these models do not generally refer directly to morning glories, I will shortly discuss their relevance to these lines. In these studies a gravity current runs into a stable layer. This gravity current may be interpreted as a cold front or a sea breeze. It is not yet clear if southerly morning glories always emerge from the collision of a cold front and a sea breeze from the north or whether the stable layer provided by a shallow radiation inversion would suffice. If the gravity current is interpreted as the east-coast sea breeze, the environmental flow which is normally present over Cape York Peninsula has to be considered. In these conditions, there are important differences between an idealised gravity current imposed by a stationary source of cold air, and a sea breeze produced by differential heating over land and sea. When a uniform environmental flow opposes an idealised gravity current of this type, the depth of the gravity current increases (Liu and Moncrieff, 1996), while sea breezes would decrease in depth in this case (Goler 2004).

The first three-dimensional modelling study of the morning glory and NACL phenomena was carried out by Noonan and Smith (1987) in which they applied a modification of a model by Pielke *et. al.* (1974). It is a hydrostatic, primitive-equation model and water vapour is carried and allowed to affect the vertical stability, but not to change state. Parameterisations for the boundary layer and short- and longwave radiation are included. The model produced convergence lines corresponding to a morning glory and an NACL. This study was complemented and extended by a study by Smith and Noonan (1998), using the Lagrangian Atmospheric Dispersion Model (LADM) which was developed at the Commonwealth Scientific Industrial and Research Organisation (CSIRO) Division of the Atmospheric Research in Australia (Physick *et. al.* 1994). This model is fully compressible and formulated in  $\sigma$ -coordinates. It incorporates parameterisations for the surface- and boundary layer and the short- and longwave radiation. Like the model in the 1987 study, water vapour does not change state. The calculations in both studies are initialised with a typical local profile and driven by a uniform geostrophic wind. The latest three-dimensional study of the morning glory and NACL so far was that by Jackson *et. al.* (2002) mentioned earlier in this chapter. This model and results will be described into more detail in Chapter 2.

## 1.4 Description of the MM5 model

The numerical simulations are carried out using the MM5 model, which I describe only briefly here. A detailed description of the model and the derivation of the equations is given by Grell *et al.* (1995). The vertical grid is arranged in  $\sigma$ -coordinates ( $\sigma = (p - p_t)/(p_s - p_t)$ , where  $p$  is pressure,  $p_s$  is the surface pressure and  $p_t$  the pressure at the model top, assumed constant, equal to 100 mb) on a Lorenz-grid (the vertical velocities are calculated halfway inbetween the full  $\sigma$ -layers, where the other model variables are situated, see Fig. 1.6a). The model is nonhydrostatic and formulated on a B-grid (Mesinger and Arakawa, 1976) in the horizontal (see Fig. 1.6b). For the later described equations, it uses second-order finite differences to represent spatial gradients and a second-order leapfrog scheme for time differencing.

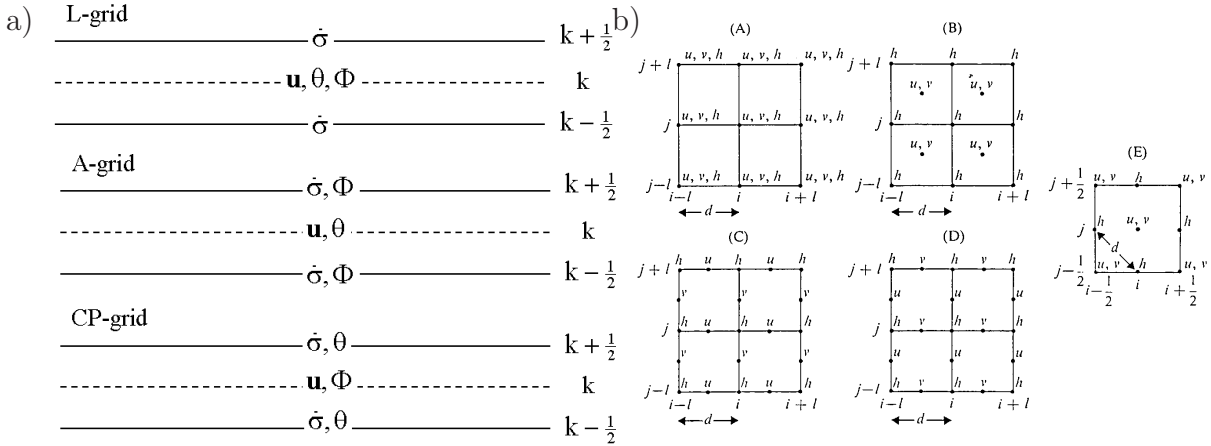


Figure 1.6: Panel (a) vertical grid configurations (from top to bottom: Lorenz-, Arakawa- and Charney-Phillips grid). The B-grid is applied in the horizontal and the Lorenz-grid in the vertical in MM5. Panel (b) possible horizontal grid configurations with the B grid in subpanel (B).

Let  $p$ ,  $T$  and  $\rho$  be the pressure, temperature and density, respectively. We consider a constant reference state (indicated by  $_0$ ) and perturbations from it (indicated by  $'$ ) defined by

$$p(x, y, \sigma, t) = p_0(z) + p'(x, y, \sigma, t), \quad (1.1)$$

$$T(x, y, \sigma, t) = T_0(z) + T'(x, y, \sigma, t), \quad (1.2)$$

and

$$\rho(x, y, \sigma, t) = \rho_0(z) + \rho'(x, y, \sigma, t). \quad (1.3)$$

Then the perturbation pressure equation is given by:

$$\frac{\partial p'}{\partial t} - \rho_0 g w + \gamma p \nabla \cdot \vec{v} = -\vec{v} \cdot \nabla p' + \frac{\gamma p}{T} \left( \frac{\dot{Q}}{c_p} + \frac{T_0}{\theta_0} D_\theta \right). \quad (1.4)$$

The three spatial components of the momentum equation are given by:

$$\frac{\partial u}{\partial t} + \frac{m}{\rho} \left( \frac{\partial p'}{\partial x} - \frac{\sigma}{p^*} \frac{\partial p^*}{\partial x} \frac{\partial p'}{\partial \sigma} \right) = -\vec{v} \cdot \nabla u + v \left( f + u \frac{\partial m}{\partial y} - v \frac{\partial m}{\partial x} \right) - e w \cos \alpha - \frac{u w}{r_{earth}} + D_u \quad (1.5)$$

$$\frac{\partial v}{\partial t} + \frac{m}{\rho} \left( \frac{\partial p'}{\partial y} - \frac{\sigma}{p^*} \frac{\partial p^*}{\partial y} \frac{\partial p'}{\partial \sigma} \right) = -\vec{v} \cdot \nabla v + u \left( f + u \frac{\partial m}{\partial y} - v \frac{\partial m}{\partial x} \right) + e w \sin \alpha - \frac{v w}{r_{earth}} + D_v \quad (1.6)$$

$$\frac{\partial w}{\partial t} - \frac{\rho_0}{\rho} \frac{g}{p^*} \frac{\partial p'}{\partial \sigma} + \frac{g p'}{\gamma p} = -\vec{v} \cdot \nabla w + g \frac{p_0}{p} \frac{T'}{T_0} - \frac{g R_d p'}{c_p p} + e(u \cos \alpha - v \sin \alpha) + \frac{u^2 + v^2}{r_{earth}} + D_w \quad (1.7)$$

Here,  $x$  and  $y$  are the eastward and northward components of a Cartesian coordinate system on the earth surface, respectively and  $p^* = p_s - p_{top}$ . The terms  $u \frac{\partial m}{\partial y}$ ,  $v \frac{\partial m}{\partial x}$  and the terms with the earth radius  $r_{earth}$  represent curvature effects and  $m$  is a map-scale factor. The Coriolis parameter is  $f = 2\Omega \sin \lambda$  and the terms  $eu$ ,  $ev$  and  $ew$  represent the usually neglected components of the Coriolis force, where  $e = 2\Omega \cos \lambda$ ,  $\alpha = \phi - \phi_c$ ,  $\lambda$  is latitude,  $\phi$  is longitude,  $\phi_c$  is the central longitude and  $\Omega$  is the angular velocity of the earth. The full Coriolis force leads to an upward/downward acceleration on westerly/easterly flows and a westward/eastward acceleration on upward/downward flows in addition to the rightward/leftward deflection on the the northern/southern hemisphere.

The first law of thermodynamics is expressed by:

$$\frac{\partial T}{\partial t} = -\vec{v} \cdot \nabla T + \frac{1}{\rho c_p} \left( \frac{\partial p'}{\partial t} + \vec{v} \cdot \nabla p' - \rho_0 g w \right) + \frac{Q}{c_p} + \frac{T_0}{\theta_0} D_\theta, \quad (1.8)$$

where the advection terms can be expanded as

$$\vec{v} \cdot \nabla A \equiv m u \frac{\partial A}{\partial x} + m v \frac{\partial A}{\partial y} + m \dot{\sigma} \frac{\partial A}{\partial \sigma} \quad (1.9)$$

with

$$\dot{\sigma} = \frac{\rho_0 g}{p^*} w - \frac{m \sigma}{p^*} \frac{\partial p^*}{\partial x} u - \frac{m \sigma}{p^*} \frac{\partial p^*}{\partial y} v. \quad (1.10)$$

The divergence term can be expanded as

$$\nabla \cdot \vec{v} = m^2 \frac{\partial}{\partial x} \left( \frac{u}{m} \right) - \frac{m \sigma}{p^*} \frac{\partial p^*}{\partial x} \frac{\partial u}{\partial \sigma} + m^2 \frac{\partial}{\partial y} \left( \frac{v}{m} \right) - \frac{m \sigma}{p^*} \frac{\partial p^*}{\partial y} \frac{\partial v}{\partial \sigma} - \frac{\rho_0 g}{p^*} \frac{\partial w}{\partial \sigma}. \quad (1.11)$$

The terms on the right ( $D_u$ ,  $D_v$ ,  $D_w$ ,  $D_\theta$ ) in equations (1.5) to (1.8) represent the horizontal diffusion, which is used to control nonlinear instability and aliasing, the vertical diffusion and the vertical mixing due to planetary boundary layer turbulence or dry convective adjustment. At the outermost two rows and columns of the large domain, a second-order horizontal diffusion of the form

$$F_{H2\alpha} = p^* K_H \nabla_\sigma^2 \alpha \quad (1.12)$$

is applied. In the inner region of the large domain and everywhere in the nests a more scale-selective fourth-order form is used:

$$F_{H4\alpha} = p^* K'_H \nabla_\sigma^4 \alpha \quad (1.13)$$

with

$$K'_H = \Delta S^2 K_H, \quad (1.14)$$

$S$  being the vertical wind shear and  $\alpha$  being any prognostic variable. The horizontal diffusion coefficient  $K_H$  consists of a background value  $K_{H0}$  and a term proportional to the deformation  $c_{def}$ :

$$K_H = K_{H0} + 0.5k^2 \Delta S^2 c_{def}, \quad (1.15)$$

where  $k$  is the von Karman constant and  $c_{def}$  is given by:

$$c_{def} = \sqrt{\left(\frac{\partial u}{\partial x} - \frac{\partial v}{\partial y}\right)^2 + \left(\frac{\partial v}{\partial x} + \frac{\partial u}{\partial y}\right)^2}, \quad (1.16)$$

A background value of  $K_H$  is determined in terms of the grid size  $\Delta x$  and time step  $\Delta t$  by

$$K_{H0} = 3 \cdot 10^{-3} \frac{\Delta x^2}{\Delta t}. \quad (1.17)$$

The vertical diffusion above the boundary layer is predicted by K-Theory:

$$F_{V\alpha} = p^* \frac{\partial K_z}{\partial z} \frac{\partial \alpha}{\partial z}. \quad (1.18)$$

The eddy diffusivity,  $K_z$ , is a function of the local Richardson number  $Ri$ :

$$K_z = \begin{cases} K_{z0} + l^2 S^{\frac{1}{2}} \frac{Ri_c - Ri}{Ri_c} & \text{for } Ri < Ri_c \\ K_{z0} & \text{for } Ri \geq Ri_c, \end{cases} \quad (1.19)$$

where  $K_{z0} = 1 \text{ m}^2/\text{s}$ ,  $l = 40 \text{ m}$ ,  $Ri_c$  is a critical Richardson number which is a function of layer thickness and the Richardson number  $Ri$  is defined as

$$Ri = \frac{g}{\theta S} \frac{\partial \theta}{\partial z}, \quad (1.20)$$

with

$$S = \left(\frac{\partial u}{\partial z}\right)^2 + \left(\frac{\partial v}{\partial z}\right)^2 + 10^{-9} \text{ s}^{-2} \quad (1.21)$$

The value  $10^{-9} \text{ s}^{-2}$  is arbitrarily added in MM5 (see model code) to avoid division by zero.

## 1.5 General model configuration

There are 24  $\sigma$ -levels with relatively high resolution in the boundary layer. The levels below 3 km are at heights of approximately: 0, 36, 73, 146, 220, 294, 370, 521, 676, 833, 1155, 1489, 1836, 2196, 2572 and 2963 m. A table with all applied  $\sigma$ -layers and a conversion into pressure and height levels is given in Appendix B.

The calculations are carried out on two horizontal domains: an outer domain with relatively coarse resolution and an inner domain with three times this resolution shown in Fig. 1.7. The outer domain has  $221 \times 221$  grid points with a horizontal resolution of 9 km and the inner domain has  $301 \times 301$  points with a horizontal resolution of 3 km. The terrain land use and topography is taken from the MM5 USGS (United States Geological Survey) data set and has a 5' resolution for the outer domain and 2' resolution for the inner domain. The time step is chosen as 27 s for the outer domain and 9 s for the inner domain. The Grell cumulus parameterisation scheme is used in the outer domain, but no such scheme is used in the inner domain. The Dudhia scheme (described by Dudhia, 1989) is chosen as an explicit scheme for moisture. The MRF boundary-layer scheme (Troen and Mahrt, 1986) is chosen for all domains. A sensitivity study of all boundary layer schemes available in MM5 showed that this scheme gives the most realistic results compared with the observations for the phenomena described. Details of this study will be presented in chapter 3. The short- and long-wave cloud and ground radiation scheme takes account of diurnal variations. A bucket soil moisture model is used to allow the soil moisture to vary with time, particularly in response to rainfall and surface evaporation. The moist vertical diffusion scheme allows diffusion in cloudy air to mix towards a moist adiabat by basing its mixing on moist stability instead of the dry stability. It can mix cloudy air upwards into clear air in addition to just internally in cloudy layers. This model configuration uses the European Centre for Medium Range Weather Forecasts (ECMWF) analysis data with a horizontal resolution of  $0.25^\circ$  for the initial and boundary conditions. However, I use soil moisture data from mesoLAPS for the bucket soil moisture model as the ECMWF data were found to be unrealistically moist for the dry season in northern Australia. Details of the sensitivity to soil moisture are given in chapter 4.

The relatively large size of the two model domains and the fine grid resolution required the use of the massive parallel processing (mpp) version of the MM5 code. Unfortunately the code of the mpp version of MM5 was not ready to run with the particular distribution of LINUX (SUSE) and compiler (INTEL FORTRAN) used in the Meteorological Institute. To setup the mpp version of MM5 on our computer system required extensive work on the code. These modifications became part of the official version 3.7 of the MM5 code.

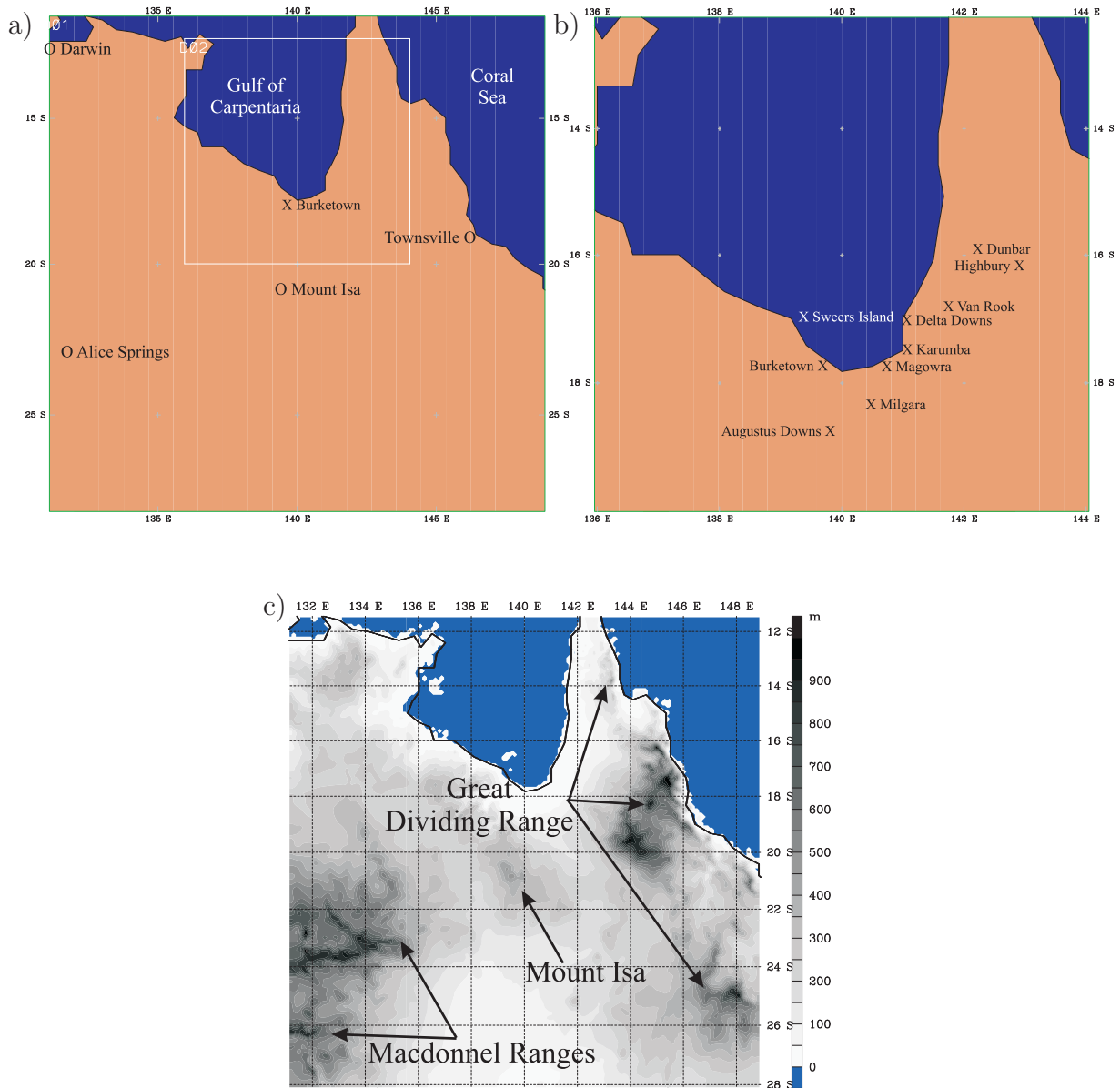


Figure 1.7: Map of north-eastern Australia showing (a) the coarse domain of the model with places mentioned in the text, (b) the inner domain with the locations of AWS stations in the southern gulf region marked by crosses and (c) significant orography within the coarse domain.

# Chapter 2

## Case studies

### 2.1 Five major events

In this chapter I focus on five events during the GLEX experiment. All dates and times are given in Eastern Australian Time (EST), which is 10 h ahead of Universal Time Coordinated, (UTC). In the first case, on 04 October 2002, there were three disturbances: a pronounced north-easterly morning glory, an NACL and a weak southerly morning glory. In the second case, on 28/29 September 2002, a major southerly disturbance moved across the southern half of the gulf. It was composed of two convergence lines, the leading line had an undular-bore-like structure and was followed some hours later by a significant air mass change. This event is described in detail in Smith *et al.* (2005). A weaker north-easterly morning glory and an NACL were present on this day also. In the third case, on 08/09 October there was a southerly and a north-easterly morning glory of comparable strength, one of the rarely observed south-easterly morning glories and an NACL. In the event of 09/10 September there were north-easterly and southerly morning glories and an NACL. On 30 September, neither the AWS recorded nor the satellite imagery showed any disturbance and this case is used to test if the model also fails to reproduce a morning-glory or NACL disturbance correctly.

In each case I begin by examining the ability of the model to reproduce the observations, first with satellite data and then with data from the AWSs at Augustus Downs, Burketown, Delta Downs, Dunbar, Highbury, Karumba, Magowra, Milgara, Sweers Island and Van Rook (the locations of these stations are shown in Fig. 1.7b). Thereafter I use the GLX simulation to explore important aspects of the evolution and other properties of the convergence lines.

## 2.2 Model setup

In addition to the model configuration described in Section 1.5, a set of medium resolution calculations was carried out. These are compared with available results from meso-LAPS simulations.

### 2.2.1 MesoLAPS simulations

Mesoscale predictions using mesoLAPS were carried out operationally for the gulf region for the duration of the GLEX experiment. For this study, digital data for only three of the events were available: 28/29 September, 03/04 October and 08/09 October. MesoLAPS is a hydrostatic model with 29 vertical levels and a horizontal resolution of 12.5 km. The initial and boundary conditions were taken from the Bureau of Meteorology's Global Analysis and Prediction System.

### 2.2.2 Medium resolution simulations, BOM

An additional set of medium resolution experiments was carried out with MM5 for comparison with the corresponding hydrostatic mesoLAPS simulations described above. These simulations are similar to those described in section five of the first chapter, but are carried out with an outer domain of  $53 \times 53$  grid points with a horizontal resolution of 37.5 km and an inner domain of  $76 \times 76$  grid points with a horizontal resolution of 12.5 km, the latter being comparable to the grid spacing of mesoLAPS. In this case, the Grell cumulus parameterisation scheme is implemented in both domains and the terrain land use and topography data sets have 10' and 5' resolution, respectively. The time step is chosen as 112.5 s for the outer domain and 37.5 s for the inner domain. In contrast to the GLX experiments, I use ECMWF forecast data for the boundary conditions as mesoLAPS uses forecast data also, albeit from the Bureau's global prediction system. Experiments of this type are referred to as "BOM".

## 2.3 03-04 October

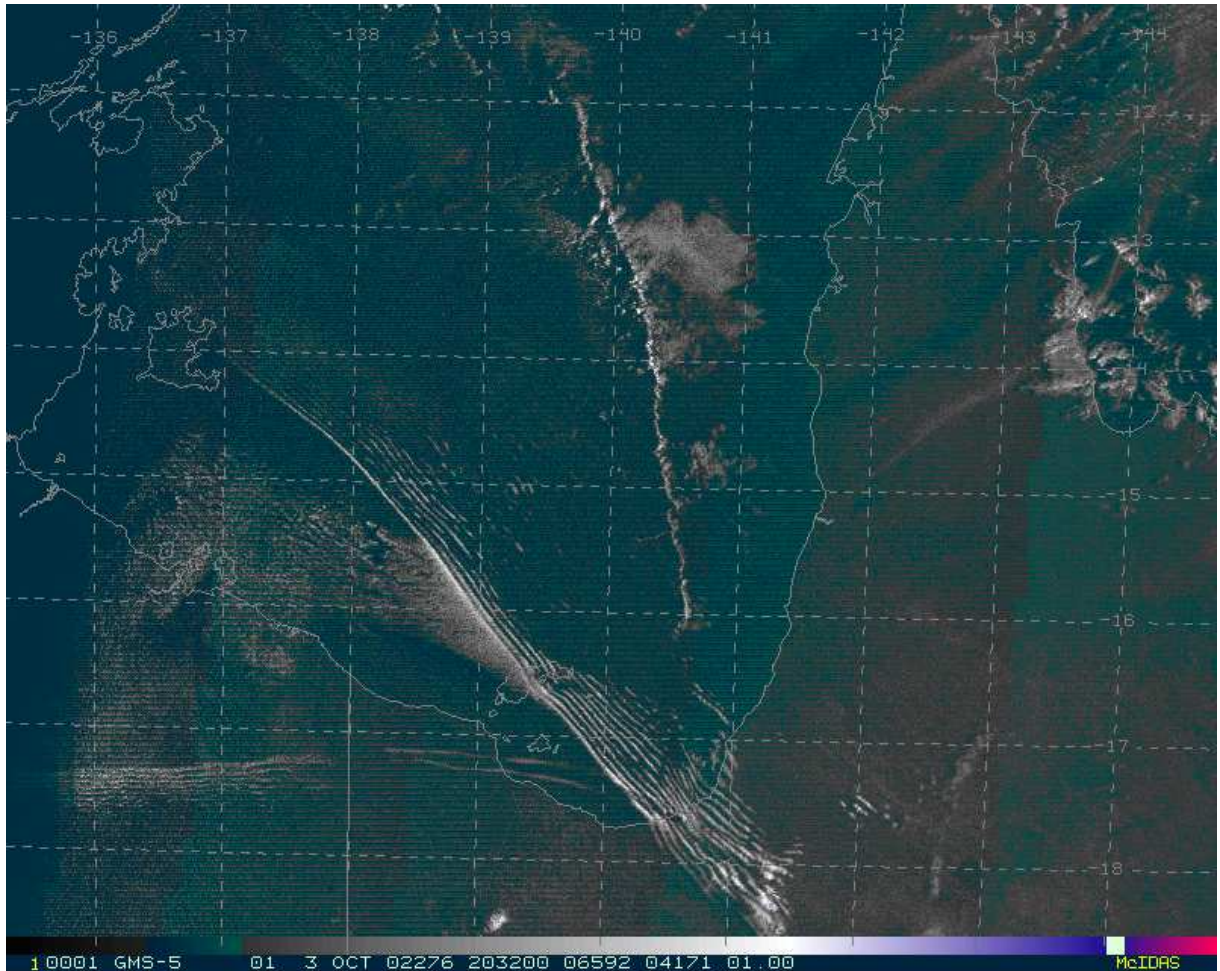


Figure 2.1: GMS visible image of the Gulf of Carpentaria region at 0632 EST on 04 October.

Figure 2.1 shows the Japanese Geostationary Meteorological Satellite (GMS) image for the gulf region at 0632 EST on 04 October. The series of cloud lines stretching north-westwards from the south-eastern corner of the gulf are associated with a north-easterly morning-glory, while a line stretching north-north-westwards from the same corner is an NACL. A pair of cloud lines forming a slightly curved arc and oriented approximately east-west south of the southern gulf coast is associated with a southerly morning glory. The model simulations for this event commenced at 1000 EST on 03 October.

Figure 2.2 compares the predicted low-level divergence at 0730 EST for the GLX and

BOM calculations and at 0700 EST for the mesoLAPS calculation (only three-hourly output is available for mesoLAPS). All three calculations show a convergence line over the southern part of the gulf that corresponds approximately to the observed position of the north-easterly morning glory. The presumption made by Jackson *et al.* (2002) that the cloud lines correspond to lines of enhanced convergence in the low-level divergence patterns was confirmed in the GLEX cases by the surface measurements. The orientation of this convergence line in the GLX and BOM calculations corresponds very well to observations (see Table 2.1), but in the LAPS run the line curves to the south at its southern end, a feature that is not seen in the satellite image. The GLX run captures the orientation and position of the NACL as well, whereas the other runs provide only a hint of it in the northern part of the gulf. Moreover, mesoLAPS places this line some 300 km too far to the north-west. Both MM5 runs produce a southerly convergence line, which is too far to the south, compared with the satellite image. MesoLAPS fails to produce this line.

Table 2.1: Observed orientation (measured anticlockwise from north) of the north-easterly morning-glory (NEMG) and NACL in Fig. 2.1 compared between the model and observations (Note that there is about half an hour difference in times in the case of mesoLAPS).

	NEMG	NACL
Observed	40°	11°
GLX	40°	9°
BOM	40°	9°
LAPS	40°	9°

I examine now the ability of the models to reproduce the surface observations at Karumba and to capture the timing of the north-easterly morning-glory convergence line at AWS stations in the southern part of the gulf. Figures 2.3a and b compare observed and model-predicted time-series of surface pressure at Karumba on 03 October. Figure 2.3a shows the total pressure, while Fig. 2.3b shows a 12 h segment of the corrected pressure, obtained by first removing daily trend and then the diurnal and semidiurnal variation. The trend was assumed to be linear throughout the day and the diurnal and semidiurnal variation were removed by performing a Fourier analysis of the pressure and then subtracting the first two wavenumbers. Both MM5 simulations (GLX and BOM) show a remarkably good agreement with the observed behaviour, but the mean pressure is offset by about 2.5 mb, which I attribute to the difference in mean height of the orography in the grid-box surrounding Karumba and the station height of the model (the actual height was estimated to be 15 m compared with 1.8 m in mesoLAPS, 0.6 m in BOM and 0 m in GLX). In contrast, the surface pressure variation is not well captured by LAPS, probably because the radiation scheme in the operational version of this model is invoked only every three hours (Dr. Bill Bourke, personal communication).

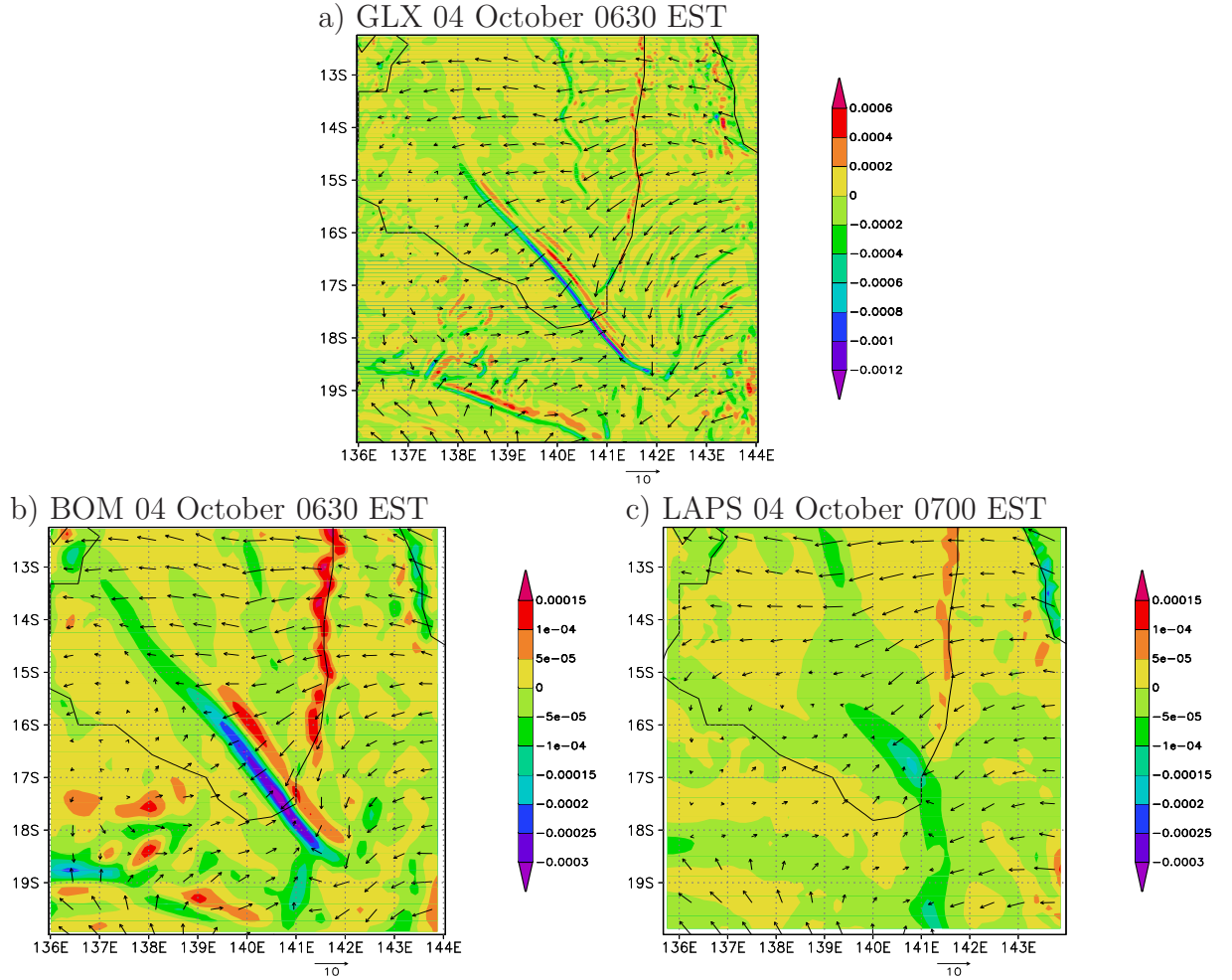


Figure 2.2: Low-level wind vectors (scale  $10 \text{ m s}^{-1}$  below each panel) and divergence (shaded, unit  $\text{s}^{-1}$ ) for the (a) GLX and (b) BOM simulations at  $\sigma = 0.9975$  at 0630 EST on 04 October, and (c) for the mesoLAPS simulation at 1025 mb and 0700 EST on this day. Note that the contour interval for divergence is different in the lower panels.

Figures 2.3c and d show time series of the zonal and meridional wind speed at Karumba. The vertical arrows indicate the passage of the north-easterly morning-glory, which is characterised by a sharp change in wind direction. As expected, the time of passage is captured best in the high-resolution GLX run, being within a few minutes of the observed time, and second best in the BOM run, where the passage is between two and three hours too late. The timing in mesoLAPS is a little worse, but it is difficult to deduce a precise value as the data are available only every three hours.

In an attempt to quantify the overall agreement between the surface pressure observed

Table 2.2: Times of passage, note that GLX times have a temporal resolution of just 30 minutes.

	<b>Observed</b>	<b>GLX</b>
Highbury	2200	0030
Dunbar	2250	0030
Van Rook	0150	0130
Delta Downs	0315	0330
Karumba	0510	0600
Magowra	0540	no signature
Milgara	0620	0700
Sweers Island	0730	0800
Burketown	0845	1000
Augustus Downs	1000	1230

at AWS stations and the corresponding pressures in the model simulations I calculate the correlation coefficient defined by

$$r = \frac{\sum (p_{meas} - \overline{p_{meas}})(p_{mod} - \overline{p_{mod}})}{\sqrt{\sum (p_{meas} - \overline{p_{meas}})^2 \sum (p_{mod} - \overline{p_{mod}})^2}},$$

where the average is taken over the stations listed in Table 2.2. The index 'meas' denotes a measured value and 'mod' refers to a particular model. The overlined variables are averaged over the 36 h integration time. For the GLX and BOM runs, the correlation,  $r = 0.95$ , is high on this day while for LAPS it is lower:  $r = 0.82$ .

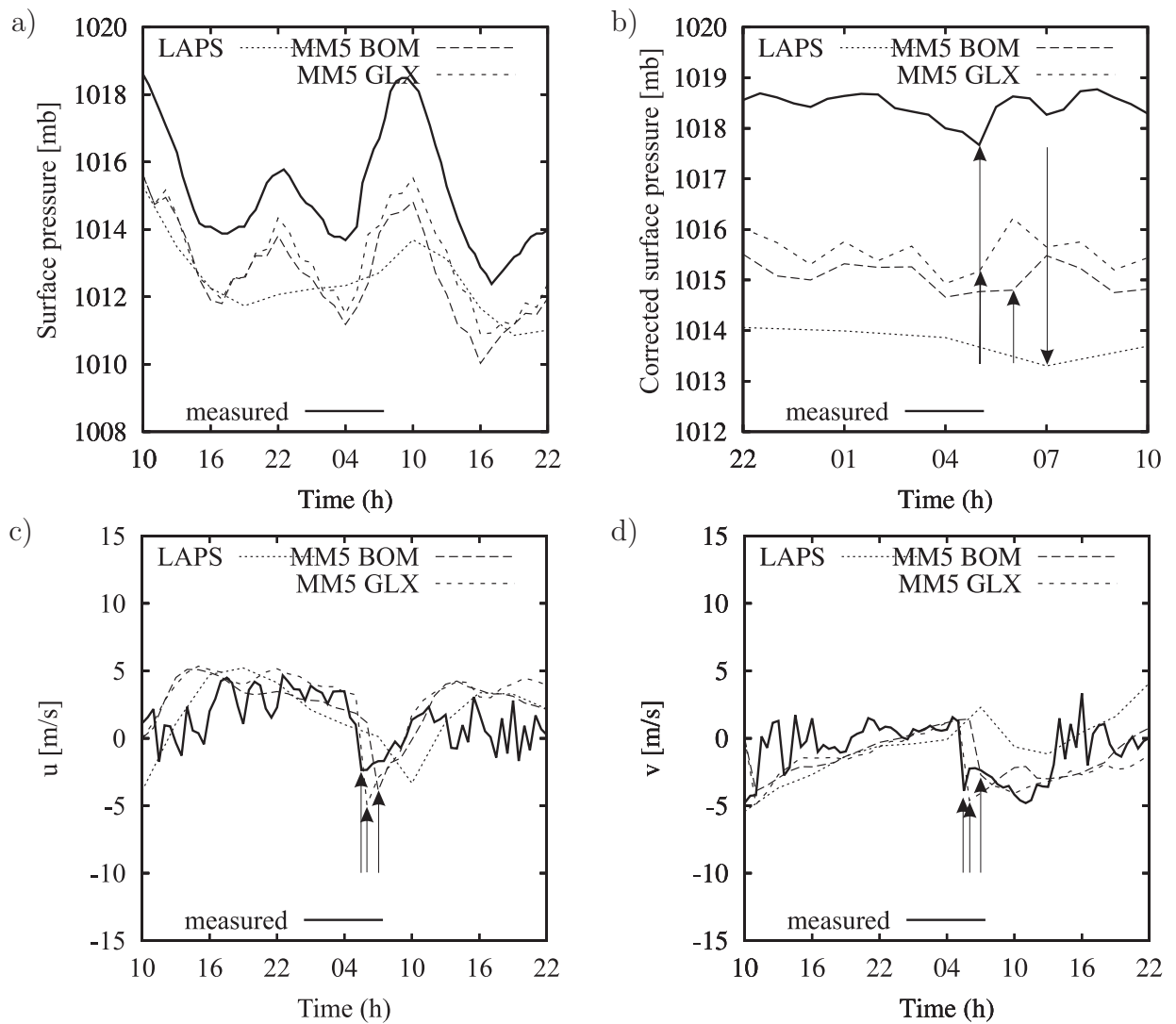


Figure 2.3: (a) Surface pressure, (b) corrected surface pressure, (c) zonal wind speed,  $u$ , at 10 m and (d) meridional wind speed,  $v$ , at 10 m at Karumba on 03-04 October (times in EST). The vertical arrows indicate times of passage of the morning-glory in the observations and in the model.

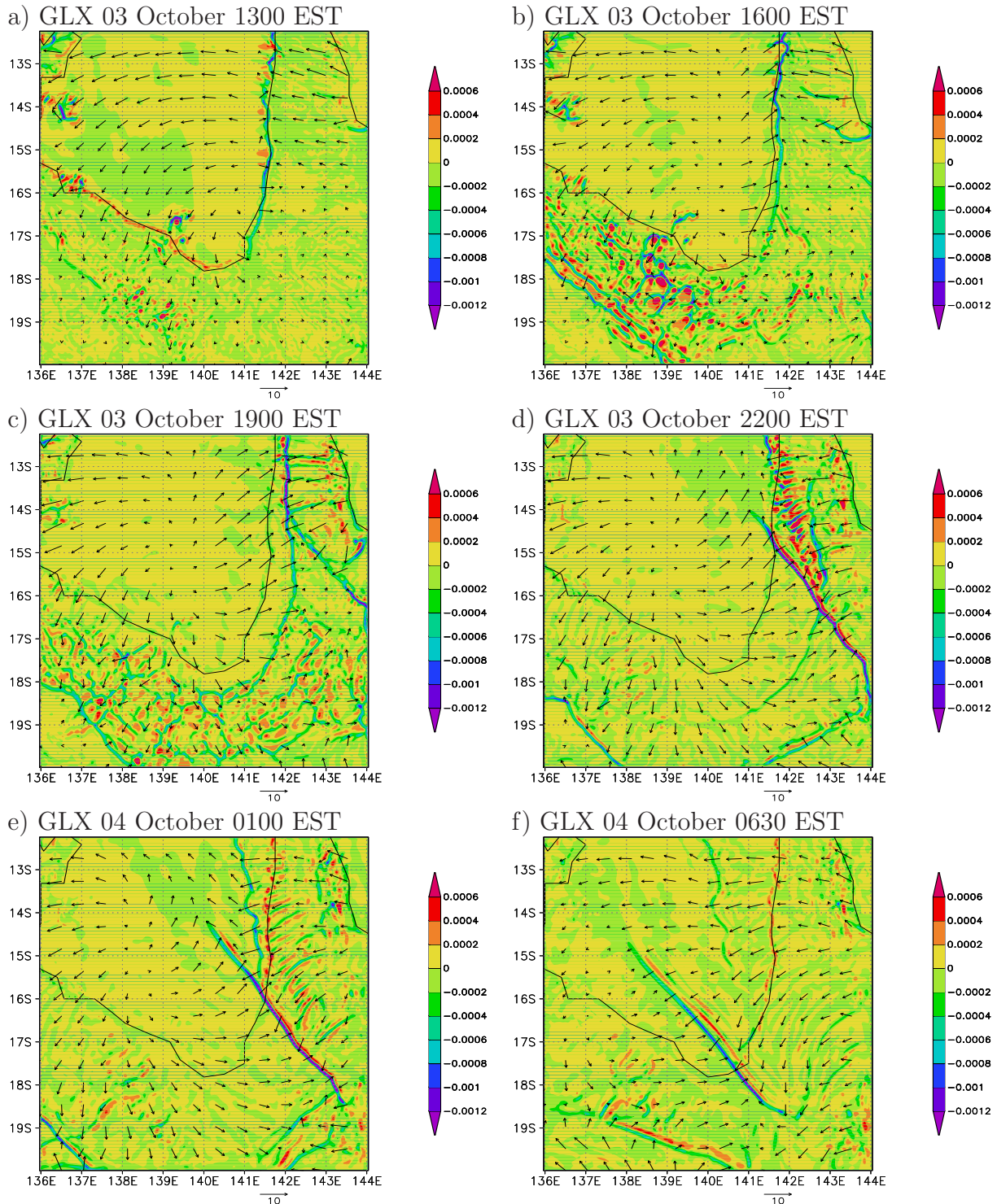


Figure 2.4: Sequence of plots of wind vectors (scale  $10 \text{ m s}^{-1}$  below each panel) and divergence (shaded, unit  $\text{s}^{-1}$ ) at  $\sigma = 0.9975$  for the GLX run at times indicated above each plot. The domain size is  $900 \text{ km} \times 900 \text{ km}$ .

The evolution of the low-level convergence lines in the GLX run is shown in Fig. 2.4. At 1300 EST the sea breeze has just begun to develop along the west coast of the peninsula and is marked there by a well-defined line of convergence along the coast because the broadscale flow is offshore along this coast. Two short lines of convergence have formed on the north-eastern side of the peninsula as well. There is also a line of convergence approximately parallel to the southern gulf coast and 100 km or more inland and a shorter line nearer to the coast, both west of  $140^\circ$  E. The line further inland is ragged at its south-eastern end suggesting a significant influence of orography in this region.

By 1600 EST the convergence line marking the west-coast sea-breeze front has moved a little inland, especially along its southern part and the lines in the north-east have lengthened. These lines are presumably a result of convergence produced by the onshore acceleration of the easterly flow in conjunction with orography. Note that the daytime occurrence of sharp sea-breeze fronts is favoured by an offshore component of the broadscale flow (Clarke, 1983). At this time two long coherent lines of convergence are evident south of the gulf, west of  $140^\circ$  E, together with many small cells of convergence, which may be an attempt by the model to capture the largest boundary layer eddies induced by the irregular terrain in this region.

By 1900 EST, which is close to sunset, the west-coast sea-breeze front has moved further inland and has joined with that which has formed inland of the concave part of the coastline in the south-eastern corner of the gulf. In the north of the peninsula the three segments of convergence evident in the east at 1600 EST have merged to form a line approximately parallel to the east coast and the collision of the north-western end of this line and the west-coast sea-breeze front has started. There are strong easterly winds to the east of this line in the north and strong north-easterlies further south. This line marks the newly formed east-coast sea-breeze front.

At 2200 EST the east-coast sea-breeze front has become split. North of about  $14^\circ$ S it is evident as a band of enhanced convergence parallel to the east coast at these latitudes and lying close to the west coast. This line lies offshore north of about  $13.5^\circ$ S and is rather broken south of  $13^\circ$ S. South of  $14^\circ$ S, the line is coherent and almost straight and its northern end extends out over the gulf. This part of the line is approximately parallel to the east coast of the peninsula south of  $14.5^\circ$ S and has strong north-easterly winds to the north-east and south-westerlies to the south-west. A narrow curved strip of enhanced convergence marks the south-coast and west-coast sea-breeze fronts inland along the entire gulf coastline. This strip intersects the east-coast sea-breeze front about  $16.4^\circ$ S. Animations of the low-level flow fields show that the convergence lines associated with the sea breezes pass through each other. However, a sequence of vertical-zonal cross-sections of wind and virtual potential temperature at  $13^\circ$ S show that after the collision, the eastward-moving convergence line propagates as a wave disturbance in the easterly flow and subsequently decays. In the lower right of Fig. 2.4d, the south-coast sea-breeze front is already 250 km

inland. A second convergence line is also evident a little further inland and separates winds with a northerly or westerly component to the north of it from those with a southerly to easterly component to the south of it. This line is associated with nocturnal ageostrophic convergence into the inland trough.

At 0100 EST on 04 October, the southern section of the east-coast sea-breeze front has moved south-westwards. Behind it over the land are strong north-easterlies, while over the sea the winds behind are south-easterly. At the same time the northern section has regained coherence and forms a separate line of convergence extending south-southeast to north-north-west over the north-eastern part of the gulf. North of its intersection with the east-coast sea-breeze front, the west-coast sea-breeze front has lost its identity. The sea-breeze front from the southern gulf coast has moved further inland, forming an arc near the southern edge of the plotting domain.

Figure 2.4f shows the situation at 0630 EST, the time of the satellite image in Fig. 2.1. At this time the convergence line that was the east-coast sea-breeze front lies very close to the location of the north-easterly morning glory in the satellite image, which is clear evidence that the latter develops out of the former. Further, the NACL lies close to the convergence line in the northern part of the gulf, the origin of which can be traced back to the east-coast sea breeze along the northern part of the peninsula. An animation of the half-hourly fields like those in Fig. 2.4 shows also a convergence line moving from the south, this being the east-west oriented line at 0630 EST in Fig. 2.4f. This line appears to be the attempt of the model to capture the southerly morning glory seen in the satellite image. However, this line is some 150 km too far south of the observed cloud line at its western end and some 200 km at its eastern end. Since the convergence line in the model is still over land when the mixed layer redevelops after sunrise, the line weakens before reaching the southern gulf coast. A likely reason for the incorrect location of this line is its incorrect location in the initial analysis. The coarser resolution operational mesoLAPS forecasts failed also to capture this disturbance.

Figure 2.5 compares the satellite picture at 1430 EST on 04 October with the model fields like those in Fig. 2.4. By this time the north-easterly morning-glory cloud line has long moved over land and disappeared in the satellite imagery, but the NACL is still evident. The position of the NACL is tolerably well captured in the model (it is close to the point  $14^{\circ}\text{S}$ ,  $139^{\circ}\text{E}$  in both the model and the image), but the orientation in the model is a little different from that observed. The sea-breeze front along the southern gulf coast and along the west coast of the peninsula is reasonably well captured also. This front is presumably close to the northern/western edge of the cumulus cloud field in the satellite image. An animation of the half-hourly fields like those in Fig. 2.4 shows that the sea-breeze front along the southern gulf coast forms out of the morning-glory convergence line, which accounts for the series of convergence lines just south of the southern tip of the gulf in the model, although such waves are not seen in the corresponding satellite image. The southern edge of this cloud field, south of the gulf, appears to correspond approximately

to a continuous line of enhanced convergence in the model, separating a north-easterly airstream to the north from a south- to south-easterly airstream to the south. In the model, this line lies close to (not more than 15 km north of) the mean axis of the inland trough at this time.

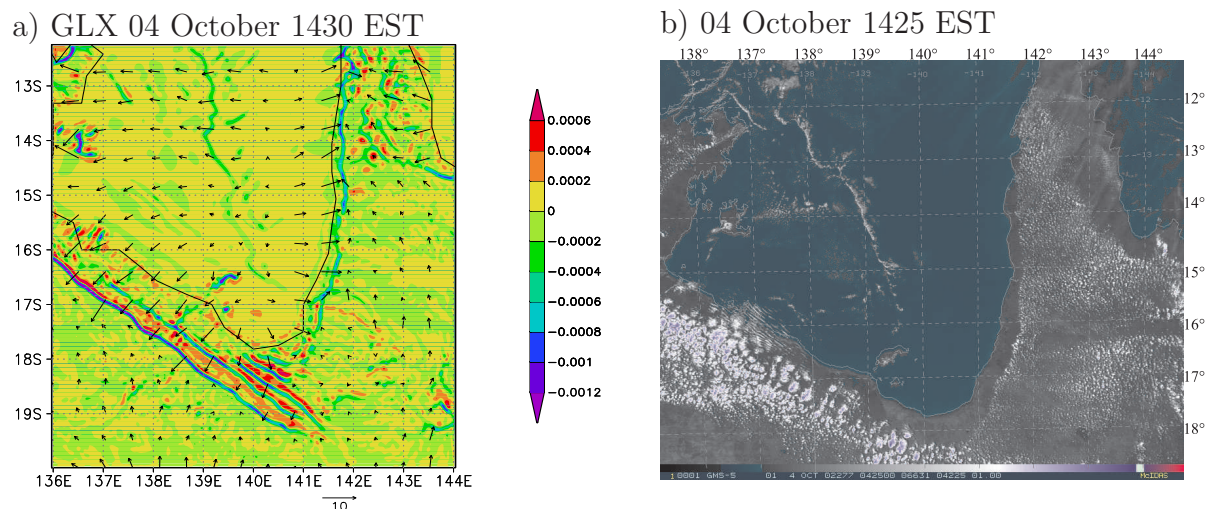


Figure 2.5: (a) Low-level wind vectors (scale  $10 \text{ m s}^{-1}$  below panel) and divergence (shaded, unit  $\text{s}^{-1}$ ) for the GLX simulations at  $\sigma = 0.9975$  at 1430 EST on 04 October. (b) GMS visible satellite image at 1425 EST on the same day.

The evolution described above provides a modified view of the generation of north-easterly morning glories compared with previous studies. The early idealised calculations by Clarke (1984) and Noonan and Smith (1986, 1987) indicated that the morning-glory is generated by the collision of the east- and west-coast sea breezes over the Cape York Peninsula. The collision results in an elevated hump of stably-stratified air that subsequently forms a south-westward propagating bore wave. The observations of bore-formation ahead of a cold front over central Australia (Smith *et al.*, 1995) and more recent calculations of morning-glory convergence lines by Smith and Noonan (1998) provide evidence that the collision of the sea breezes is not a necessary prerequisite for producing a bore-wave (in the Smith and Noonan calculations, the convergence line is also well-formed south of the gulf coast where no collision occurs). The foregoing model simulations as well as the more recent mesoLAPS calculations by Jackson *et al.* (2002) all indicate that the morning glory and NACL are associated with the same convergence line although the observations during GLEX suggested that this is not the case. Indeed, a feature of the foregoing GLX calculation, in contrast to all previous calculations, is the clear distinction it shows between the convergence line that corresponds to the morning glory and that which corresponds to the NACL.

In a very recent study by Goler and Reeder (2004) using an extremely-high resolution (200 m in the horizontal) two-dimensional model, the air behind the east-coast sea-breeze front is warmer than the air behind the west-coast sea-breeze front and runs over the west-coast sea breeze to form the morning-glory convergence line. In their calculation the sea surface temperature is the same on both sides of the peninsula, while in my calculations, the sea surface temperature is lower in the Coral Sea than in the Gulf of Carpentaria. A vertical cross-section of virtual potential temperature,  $\theta_v$ , water vapour mixing ratio and horizontal wind vectors from (15.5°S, 141.5°E) to (13.5°S, 143°E) at 1900 EST and 2000 on 03 October, shortly before and shortly after the collision of the two sea breezes, is shown in Fig. 2.6. Inspection of the 1900 EST cross-section shows that in the present simulation, the depth of the cold air behind the west-coast sea-breeze front is shallower and the air just behind the front is a little moister than that behind the east-coast sea-breeze front. Furthermore the horizontal gradient of  $\theta_v$  near the surface is largest across the west-coast sea-breeze front, suggesting that the east-coast sea breeze will rise above the west-coast sea breeze at collision, as in the Goler and Reeder calculations. However, one would not expect the present model with 3 km horizontal resolution to capture the details of the collision process, especially because the boundary-layer scheme that is implemented in the model at all grid points is unlikely to be valid near the collision point. Calculations not shown indicate that the pseudo-equivalent potential temperature of air behind the west-coast sea-breeze front is a little larger than that behind the east-coast sea-breeze front.

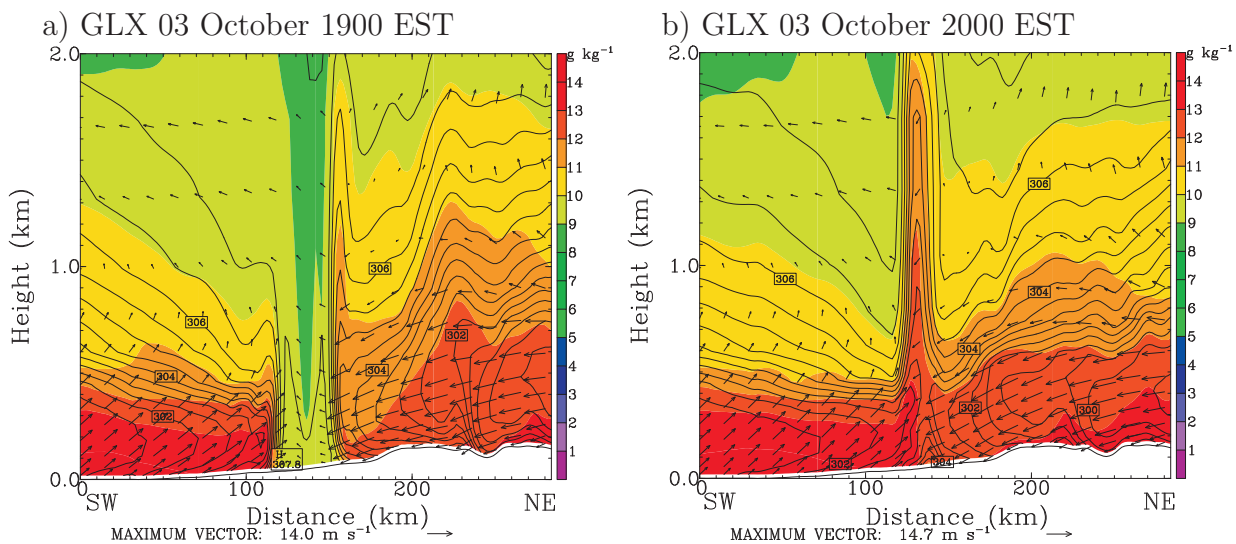


Figure 2.6: Vertical cross-section of virtual potential temperature (contour lines, interval 0.5 K), water vapour mixing ratio (shaded, in  $\text{g kg}^{-1}$ ) and horizontal wind vectors from the surface to 2 km at (a) 1900 EST, and (b) 2000 EST on 03 October. The cross-section extends from (15.5°S, 141.5°E) to (13.5°S, 143°E). In (a) the two sea breezes are about to collide and (b) is just after the collision.

Figure 2.7 and 2.8 show the relative flow,  $u - c$ , directly behind the NACL and behind the morning-glory convergence lines at a height of  $\sigma = 0.965$  and at selected times, where  $u$  is the wind speed perpendicular to and towards the line in question and  $c$  is the propagation speed of that line. In these calculations the orientation of the NACL is  $\sim 10^\circ \pm 1^\circ$  at 0000 and 0300 EST on 04 October, and  $\sim 8^\circ \pm 1^\circ$  at 0500 EST, measured anticlockwise from north. The mean propagation speed of this line between 2200 EST on 03 October and 0700 EST on 04 October is  $\sim 4.8 \text{ m s}^{-1}$ . The morning-glory line has an orientation of  $\sim 36.7^\circ \pm 1^\circ$  at 0000 EST,  $\sim 39.5^\circ \pm 1^\circ$  at 0300 EST, and  $\sim 40.0^\circ$  at 0500 EST on 04 October. The translation speeds of this line at these times are  $10.1 \text{ m s}^{-1}$ ,  $10.1 \text{ m s}^{-1}$  and  $10.7 \text{ m s}^{-1}$ , respectively. The errors in calculating these propagation speeds are estimated to be less than  $1 \text{ m s}^{-1}$ . It is seen that the relative flow behind, i.e. to the east of both lines is positive (i.e. towards the line) after the collision of east- and west-coast sea breezes. A positive value of  $u - c$  is indicative of mass transport like in a gravity current, while a negative value is characteristic of a bore-like disturbance (Simpson 1997). Figure 2.7 shows that for this event, at least, the NACL has the clear structure of a gravity current, both before and after the collision of the sea breezes. The same is true of the morning-glory disturbance at first, but  $u - c$  progressively declines behind the disturbance and eventually becomes negative. After about 0500 EST, the relative flow behind the morning-glory is everywhere negative and its transition to a bore wave is complete.

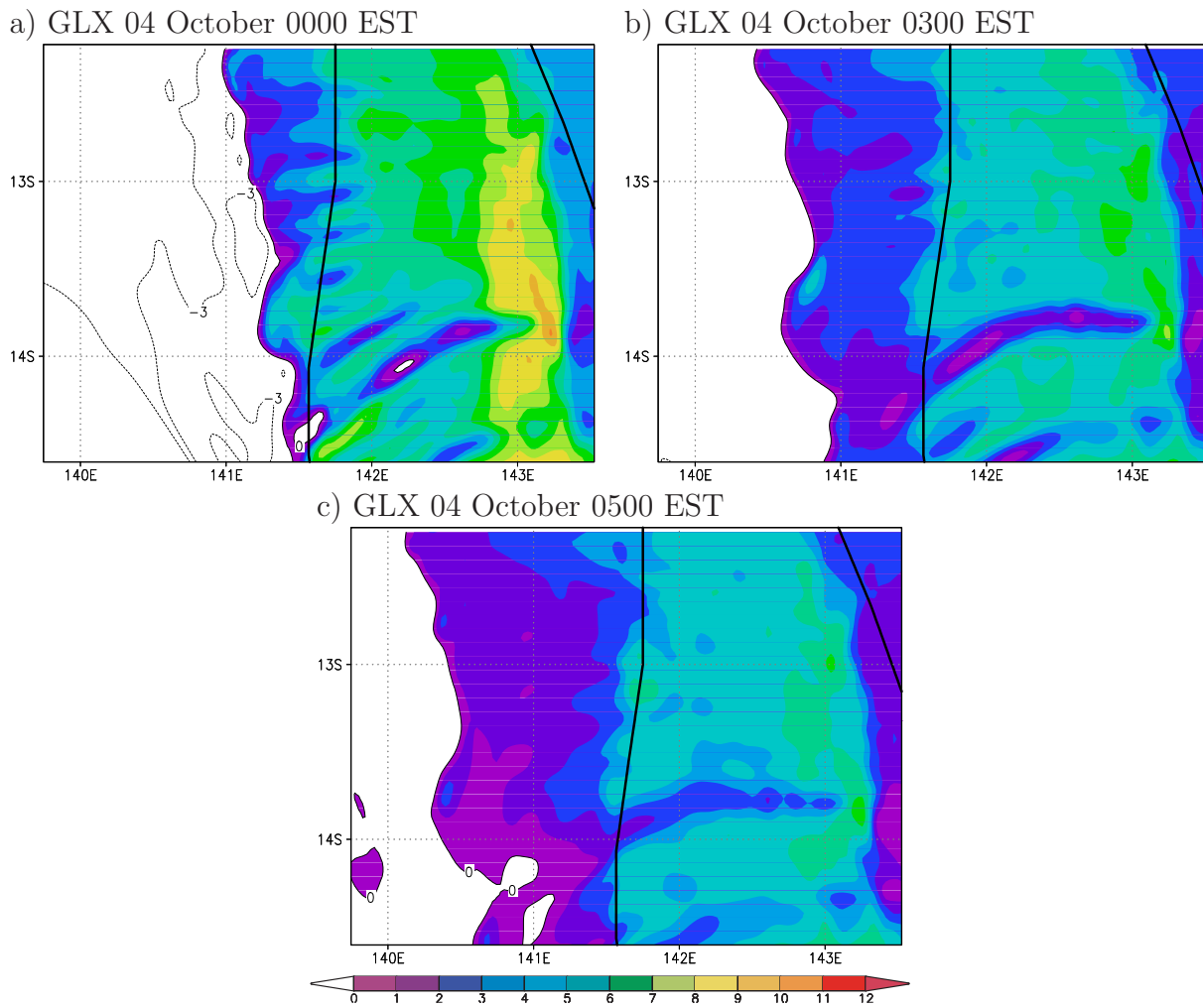


Figure 2.7: Calculations of the relative flow,  $u - c$  (in  $\text{m s}^{-1}$ ), normal to and behind the NACL at  $\sigma=0.965$  in the GLX run on 04 October at times indicated. Positive values of  $u - c$  are shaded.

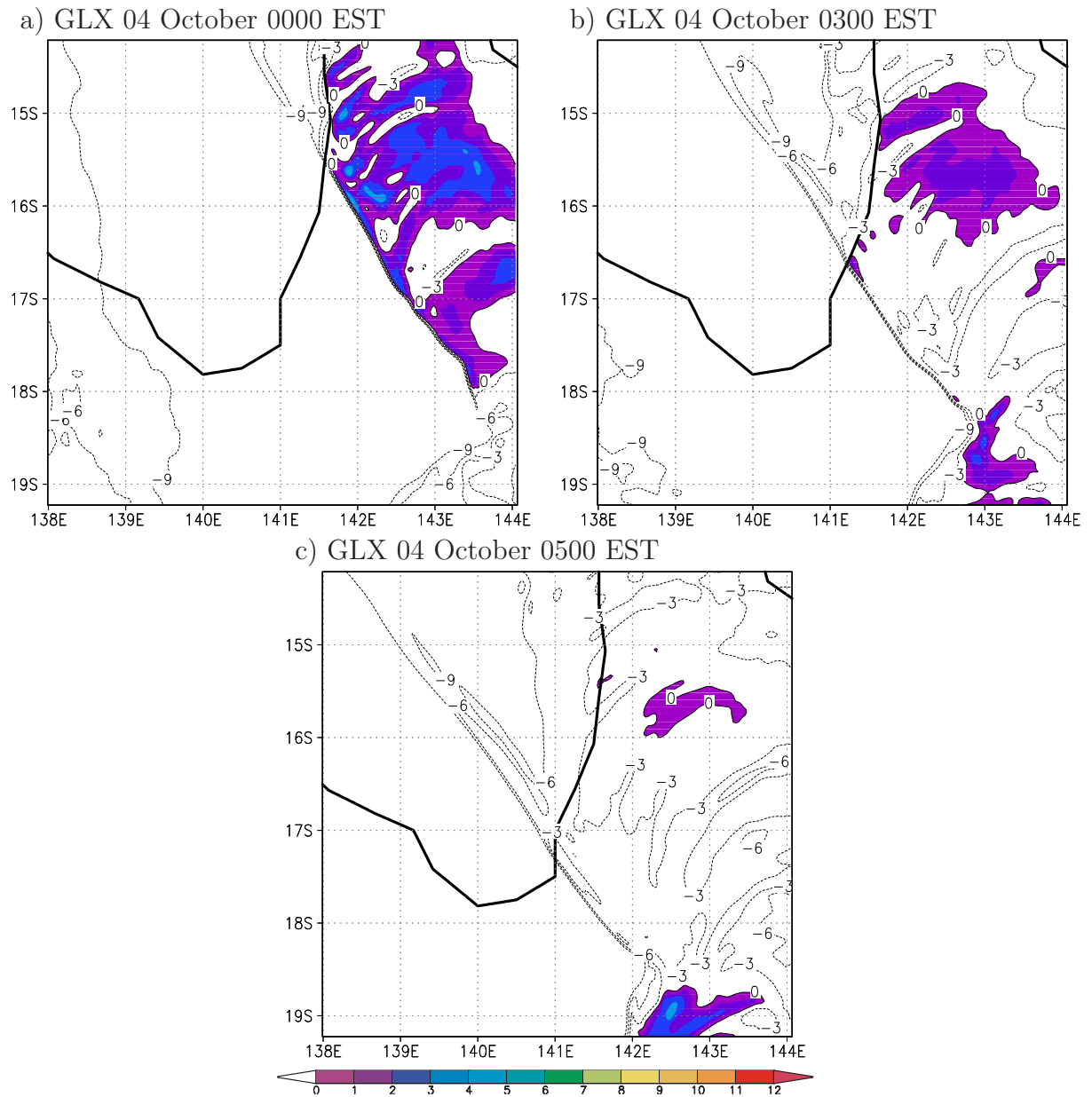


Figure 2.8: Calculations of the relative flow,  $u - c$  (in  $\text{m s}^{-1}$ ), normal to and behind the morning-glory convergence line at  $\sigma=0.965$  in the GLX run on 04 October at times indicated. Positive values of  $u - c$  are shaded.

The MSLP analysis shown in Fig. 2.9 gives a synoptic overview at 0400 EST in the morning of 04 October. A trough line following Australia's coast line except for the southern coast surrounds a high-pressure system centred at the Great Australian Bight. The position of this trough line in the Gulf of Carpentaria region is about 50 km south of the southern coast of the gulf. The satellite image in Fig 2.1 shows the southerly morning glory

has reached the gulf coast about 2 h later. This close temporal distance suggests that there is a link between the trough line and possibly the collision of an associated airmass with the south-coast sea breeze and the occurrence of a morning glory.

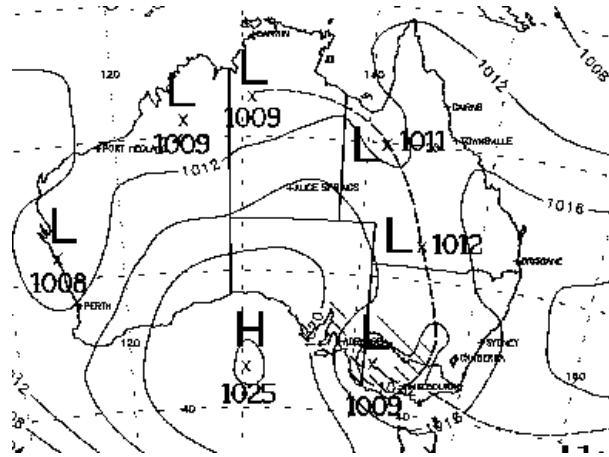


Figure 2.9: Trough line in the Gulf of Carpentaria region at 0400 EST on 04 October (adapted from Bureau of Meteorology mean sea level analysis).

Figure 2.10 shows the distribution of mean sea level pressure together with regions of strong convergence and large water vapour mixing ratio gradients. An arc of strong moisture gradient south of the south coast in panel (a) marks the south-coast sea-breeze front (marked by the bold dashed line I). The convergence line corresponding to the sea-breeze front is too weak to appear in this plot, but coincides with the arc of strong moisture gradient. A broken arc of strong convergence coinciding with strong moisture gradient marks the sea-breeze front of the previous day (02 October) to the south (indicated by the bold dashed line marked II). The air between both sea-breeze fronts is drier than behind the sea-breeze front of 03 October and moister than the air to the south. The trough line is marked by an arc of low mean sea level pressure (the bold dashed line marked III), stretching approximately from to  $18.5^\circ$  S on the left edge of the figure ( $134^\circ$  E) to  $142^\circ$  E on the lower edge of the figure ( $24^\circ$  S). An arc of strong convergence has formed at the northern edge of the southerly ageostrophic flow towards the trough. A study with an idealised numerical model of the dynamics of heat lows in simple background flows by Spengler *et al.* (2005) shows that strong low-level convergence into the trough during night generates intense, but shallow cold fronts. The figures described in the next paragraph show that a cold front (indicated by the bold dashed line marked IV) has indeed formed to the south of the trough line. The collision of the cold front and the sea-breeze front of 02 October has just begun in the central parts of the fronts at 0000 EST on 04 October. Panel (b) shows the situation 6 h later. The field of high moisture associated with the sea breezes has been pushed northwards by the cold front and the convergence line, which was located south of the region of moisture gradient before the collision, is now located on the northern side of the moisture gradient. The moderately moist air associated with the sea

breeze of 02 October is elevated by the sea breeze of 03 October and the cold front. Unlike in the other southerly events of this study, the convergence line which corresponds to the southerly morning glory does not run far north of the strip of strong moisture gradient and is located about 150 km further to the south than the position of the southerly morning glory in the satellite image in Fig. 2.1. The north-easterly morning-glory disturbance and the convergence line corresponding to the NACL are visible in both panels also.

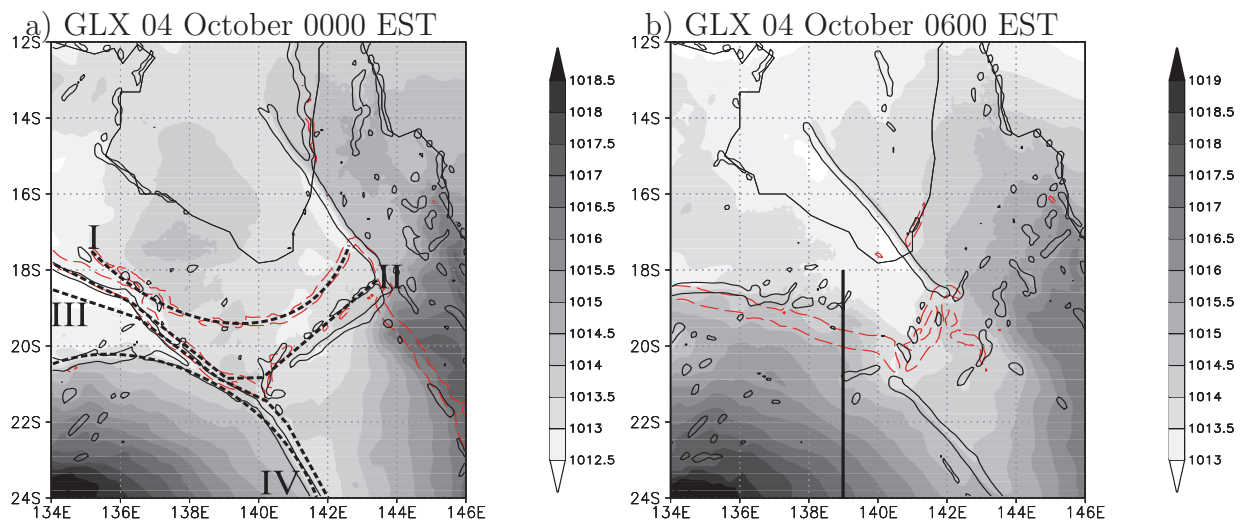


Figure 2.10: Mean sea level pressure (shaded) at 0000 EST (a) and 0600 (b) on 04 October. Solid black lines show the region where the low-level wind divergence is less than  $-8 \times 10^{-5} \text{ s}^{-1}$  indicating strong convergence. Dashed red lines show where the water vapour mixing ratio gradient exceeds  $8 \times 10^{-4} \text{ km}^{-1}$ . The bold dashed lines marked by Roman numerals in panel (a) refer to the text, the straight bold line in panel (b) indicates the position of the cross sections in Fig. 2.11.

Figure 2.11 shows a vertical cross-section of virtual potential temperature, water vapour mixing ratio and the (horizontal) wind vectors from 24°S to 18°S along 139°E (indicated in Fig. 2.10 b) at 2300 EST on 03 October and 0100 EST on 04 October, shortly before and after the collision of the two air masses associated with the sea breeze of 02 October and behind the trough line shown in Fig. 2.10. The Roman numerals shown in the figure correspond to the numbers in the previous paragraph. At 2300 EST the region south of the cold front (IV) coincides with the region of coolest air. The air is relatively dry and there is a decline in mixed-layer temperature towards the south (this decline continues much further south than shown in this figure). The driest air lies between the cold front and the sea breeze. Indeed the vertical structure of the atmosphere in this region is reminiscent of that behind a cold front. The low-level flow to the north is moist and is associated with the sea breezes from the southern gulf coast. A comparison of both panels shows that, following the collision, the warm dry air between cold front and the sea breeze of

02 October is raised. A bore wave marked by an elevation of the isentropes is seen ahead of the cold front at 0100 EST on 04 October. The collision of the cold front and the sea breeze of 03 October occurs around 0300 EST on 04 October, but this collision does not appear to generate an additional bore wave. The collision rather seems to strengthen the existent disturbance.

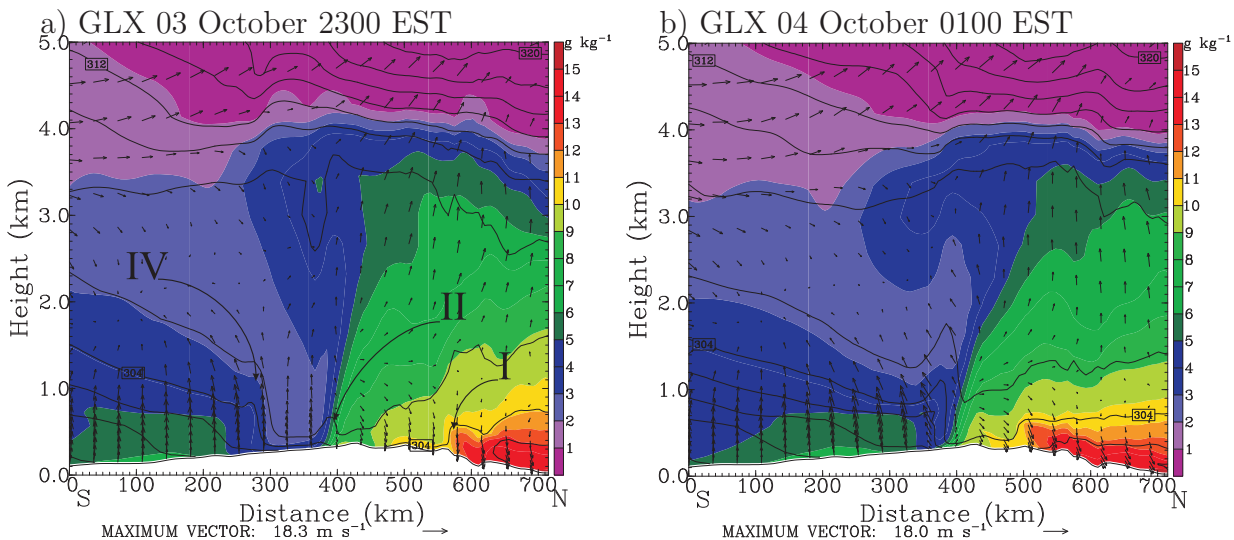


Figure 2.11: Vertical cross-section of virtual potential temperature (contour lines, interval 0.5 K), water vapour mixing ratio (shaded, in  $\text{g kg}^{-1}$ ) and horizontal wind vectors from the surface to 5 km at (a) 2300 EST on 03 October, and (b) 0100 EST on 04 October. The cross-sections extend from  $24^{\circ}\text{S}$  to  $18^{\circ}\text{S}$  along  $139^{\circ}\text{E}$ , a distance of about 750 km. Panel (a) shows the cold front and sea breeze south of the gulf before their collision near Mount Isa, and panel (b) after the collision. The Roman numerals refer to Fig. 2.10.

Figure 2.12 shows the relative flow in the model,  $u - c$ , directly behind the cold front (left panel) and the bore wave ahead of it (middle and right panel) at a height of  $\sigma = 0.965$  at selected times. Again  $u$  is the wind speed perpendicular to and towards the line in question and  $c$  is the propagation speed of that line (note that  $c$ 's are different for each line). In these calculations the orientation of the lines is  $\sim 70^{\circ} \pm 1^{\circ}$  at 0200 EST,  $\sim 62^{\circ} \pm 1^{\circ}$  at 0400 and  $\sim 66^{\circ} \pm 1^{\circ}$  at 0600 EST on 04 October, measured anticlockwise from north. The mean propagation speed of the cold front at 0200 EST is  $\sim 8 \text{ m s}^{-1}$ . The translation speeds of the morning-glory convergence line at 0400 EST and 0600 EST on 29 September are  $10 \text{ m s}^{-1}$  and  $12 \text{ m s}^{-1}$ , respectively. The errors in calculating these propagation speeds are estimated to be less than  $1 \text{ m s}^{-1}$ . It is seen that the relative flow on the southern side of the cold front is positive (i.e. towards the line) shortly after the collision of the cold front and the south-coast sea breeze. As noted earlier, a positive value of  $u - c$  is indicative of a gravity current, while a negative value is characteristic of a bore-like disturbance. Figure 2.12 shows that  $u - c$  becomes negative behind the northward-moving line that emerges

from the collision of the northward-moving front and the sea breeze. After about 0400 EST on 04 October, the relative flow behind the morning-glory convergence line is everywhere negative and its transition to a bore wave is complete.

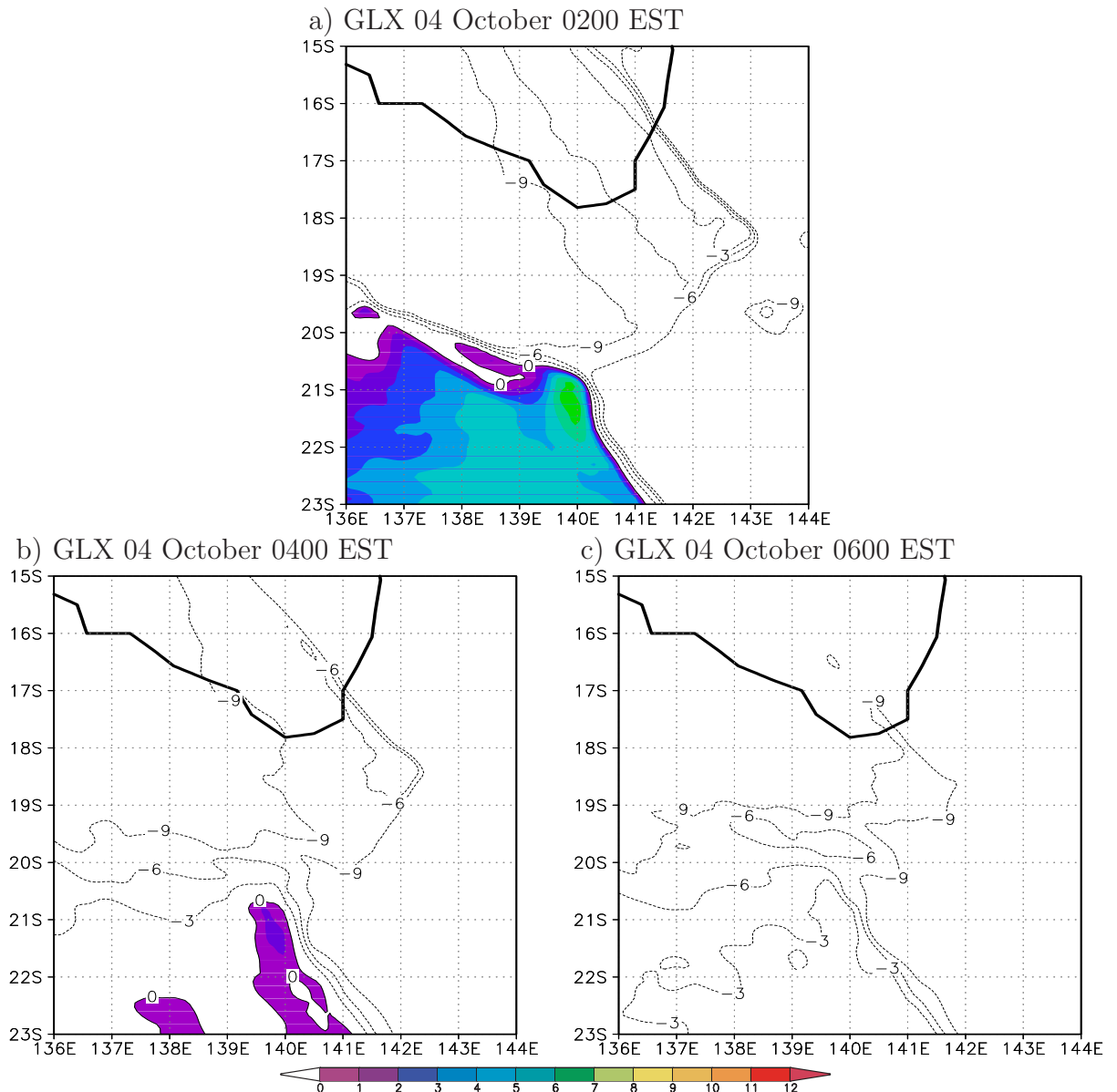


Figure 2.12: Legend as for Fig. 2.7, but for the relative flow normal to and behind cold front and the southerly morning glory disturbance on 04 October. Positive values of  $u - c$  are shaded.

## 2.4 28-29 September

The synoptic situation for this event is exemplified by the MSLP analysis for 2200 EST 28 September shown in Fig. 2.13a. An anticyclone centred in the Great Australian Bight extends a ridge almost to the southern gulf coast, while the inland trough (marked by the dashed line in this figure) over northern Australia lies just south of this coast. The precursors to this event are seen in the National Oceanic and Atmospheric Administration's Advanced Very High Resolution Radiometer (AVHRR) infrared satellite image at 1950 EST on 28 September shown in Fig. 2.13b. The image shows the sea-breeze front along the coastal region of the southern and eastern gulf, which is marked partly by line segments of cloud and elsewhere by a sharp gradient in texture, presumably associated with the cooler sea breeze air (this boundary is highlighted by a dotted line and marked SBF in Fig. 2.13b). A second boundary evident in Fig. 2.13b is marked also by a sharp gradient in texture and partly by line segments of cloud. This line is highlighted by a dashed line in Fig. 2.13b and appears to be associated with a convergence line approaching from the south (see below).

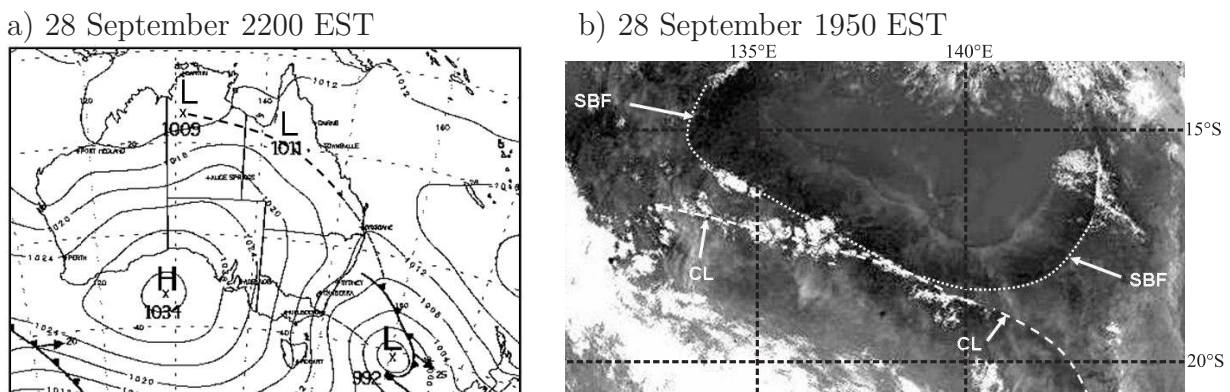


Figure 2.13: (a) Trough line in the Gulf of Carpentaria region at 2200 EST on 28 September (adapted from Bureau of Meteorology mean sea level analysis). (b) NOAA AVHRR infrared satellite image for the Gulf of Carpentaria area at 1950 EST on 28 September. SBF stands for sea-breeze front and CL stands for convergence line.

Figure 2.14 shows the low-level wind and divergence at two times on this day. Panel (a) shows fields for the GLX run at 2000 EST, which should be compared with the satellite image for 1950 EST in Fig. 2.13. It is seen that the position of the sea-breeze front and the convergence line south of it agree well with the positions of these lines in the satellite image, where they are denoted by SBF and CL, respectively. At 2200 EST, all three models show the southerly convergence line, which the calculations indicate marks the trough line. Only the high-resolution run separates this line into the southerly morning glory to the

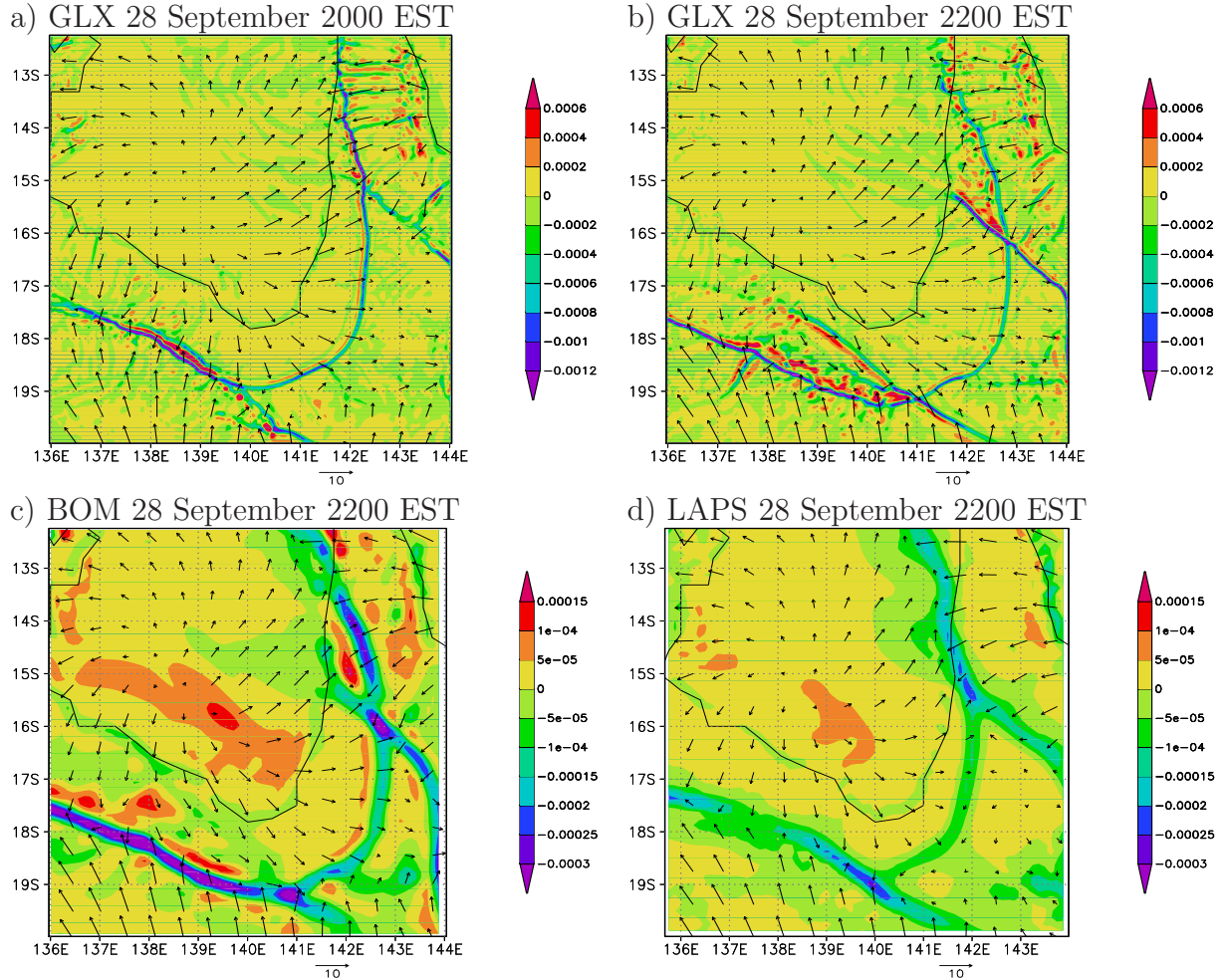


Figure 2.14: Low-level wind vectors (scale  $10 \text{ m s}^{-1}$  below each panel) and divergence (shaded, unit  $\text{s}^{-1}$ ) in the GLX calculation at (a) 2000 EST and (b) 2200 EST on 28 September. Panels (c) and (d) show the corresponding fields for the BOM and mesoLAPS calculations, respectively, at 2200 EST. The plots for the GLX and BOM fields are at  $\sigma = 0.9975$ , and that for mesoLAPS at 1025 mb. Panel (a) should be compared with the infrared satellite image in Fig. 2.13, which is valid 10 min. before. Note that the contour interval for divergence is different in the lower panels.

north and the sea breeze to the south. The models show also a north-easterly line oriented south-east to north-west near the west coast of the peninsula, the existence of which was evident in the AWS data at Dunbar and Highbury (see Fig. 1.7b). Moreover, all models capture the sea-breeze front, parallel to and inland of the gulf coast, the passage of which was also observed at AWS stations. The convergence lines are much sharper in the GLX run because of its higher resolution, but the positions of these lines are similar in all the models.

Panel (a) of Fig. 2.15 shows isochrones of the northward-moving convergence lines in the high-resolution GLX simulation. Panel (b) shows the trough line, which is marked by a band of low mean sea level pressure at 2000 EST on 28 September. To the south of this band at the front of the southerly ageostrophic flow towards the trough a line of strong convergence has formed. The sea-breeze front is marked by an arc of enhanced convergence coinciding with an arc of large moisture gradient inland of the gulf. As in the 03/04 October case, the convergence towards the trough has generated a cold front. The collision of the cold front and the south-coast sea breeze has already commenced by this time. The band of strong moisture gradient to the south-east of the sea-breeze front marks the cold front where it has not yet collided with the sea breeze. The position of the front is consistent with the convergence line indicated in the satellite image in Fig. 2.13 b.

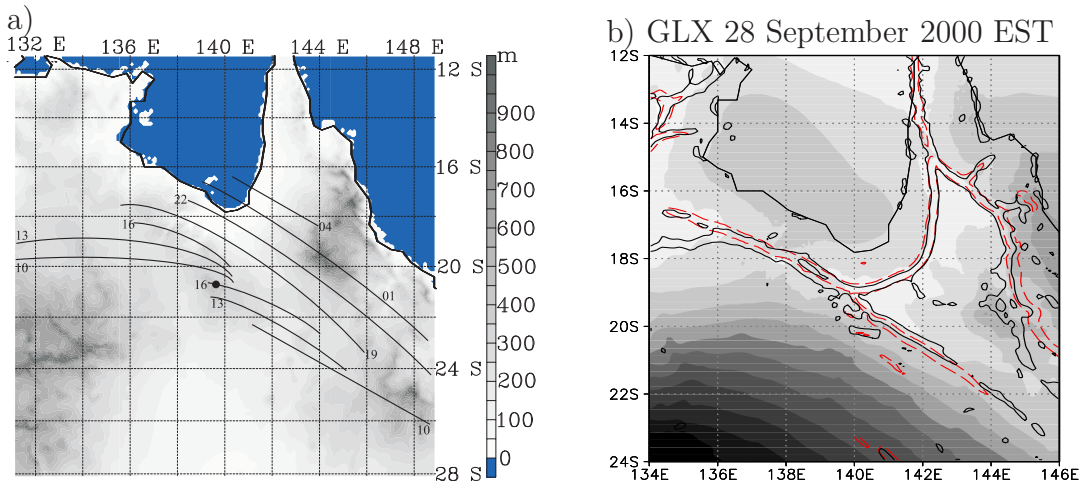


Figure 2.15: (a) Positions of the trough line (from 1000 EST to 1900 EST on 28 September) and southerly morning-glory disturbance (from 2200 EST to 0200 EST on 29 September) indicated by thick solid lines. Surface orography is shaded. (b) Mean sea level pressure (shaded) at 2000 EST on 28 September. Solid black lines show the region where the low-level wind divergence is less than  $-8 \times 10^{-5} \text{ s}^{-1}$  indicating strong convergence. Dashed red lines show where the water vapour mixing ratio gradient exceeds  $8 \times 10^{-4} \text{ km}^{-1}$ .

Figure 2.16 shows a vertical cross-section of virtual potential temperature, water vapour mixing ratio and the (horizontal) wind vectors at 1800 EST and 2200 EST on 28 September from 20°S on 138°E to 15°S on 142°E. At 1800 EST the inland trough coincides with the region of warmest air and with the deepest well-mixed layer. The low-level flow to the north-east of the trough is moist and corresponds to the sea breeze from the southern gulf coast. To the south-west of the trough the air is relatively dry and there is a decline in mixed-layer temperature towards the south (this decline continues much further south than shown in this figure). Indeed the vertical structure of the atmosphere in this region

is reminiscent of that behind a cold front. On the right of panel (b), the disturbance corresponding to the north-easterly morning glory is evident by the sharp jump in the isentropes.

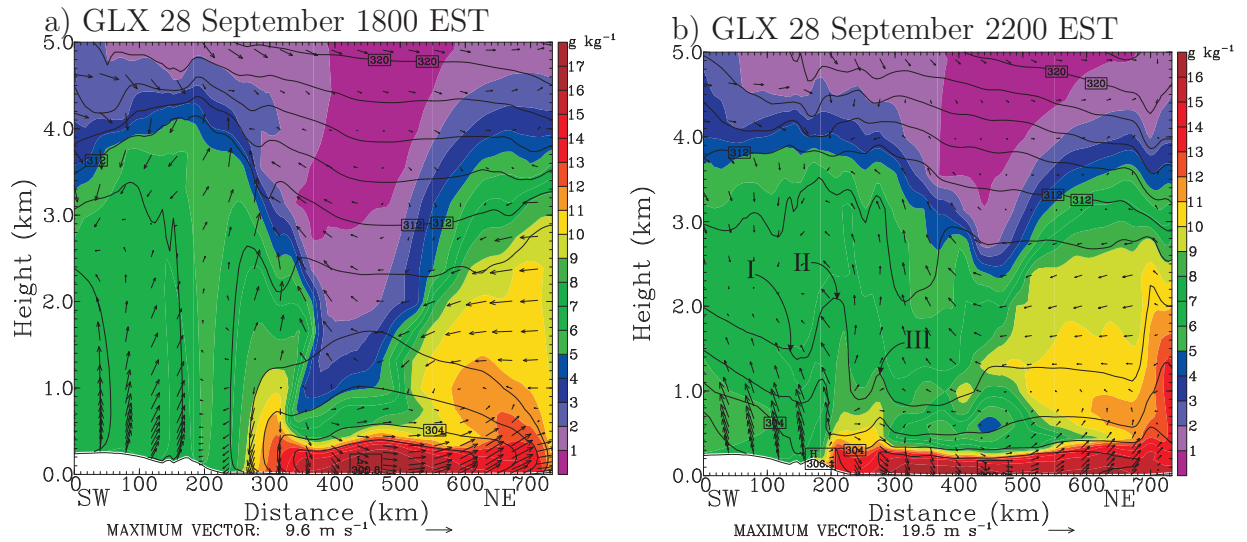


Figure 2.16: Vertical cross-section of virtual potential temperature (contour lines, interval 0.5 K), water vapour mixing ratio (shaded, in  $\text{g kg}^{-1}$ ) and horizontal wind vectors from the surface to 5 km at (a) 1800 EST, and (b) 2200 EST on 28 September. The cross-sections extend from  $20^{\circ}\text{S}$  on  $138^{\circ}\text{E}$  to  $15^{\circ}\text{S}$  on  $142^{\circ}\text{E}$ , a distance of about 750 km (the position of the cross section is indicated by the solid line in Fig. 2.17a) Panel (a) shows the nocturnal front and sea breeze south of the gulf before their collision near Mount Isa, and panel (b) after the collision. The right panel shows also the disturbance corresponding to the north-easterly morning glory. The Roman numerals in panel (b) refer to positions in Fig. 2.17a.

In an hourly animation of low-level wind divergence, the coherence of the convergence towards the trough is disrupted by the orography in the vicinity of Mount Isa, but becomes reestablished as the disturbance moves northwards over the flatter terrain to the north. It is here where the cold front collides with the sea breeze before continuing its generally northward movement. A comparison of the two panels in Fig. 2.16 shows that following the collision, the warm dry air between cold front and sea breeze is raised above the surface. A bore wave, marked by an elevation of the isentropes, is seen ahead of the front at 2200 EST. The latter is the precursor to the model analogue of the southerly morning glory. It has strong southerly winds behind it at low levels.

The disturbance observed on 28/29 September consisted of two convergence lines: a leading line with an undular-bore-like structure followed later by a significant airmass change. The separation in time between the arrival of each line increased from one and a

quarter hours to five hours as the disturbance progressed northwards. The GLX configuration shows also the formation of two northward-propagating lines. These are seen in Fig. 2.17, which shows the same fields as in Fig. 2.15, but at 2200 EST on 28 September and 0200 EST on 29 September. The convergence line and dry line that were coincident at 2000 EST in Fig. 2.15b have separated by 2200 EST (Fig. 2.17a) and the separation continues to 0200 EST (Fig. 2.17b). The leading disturbance (marked by the fork-shaped pattern of strong convergence near the south-eastern corner of the gulf in Fig. 2.17b) propagates to the north-east, moving ahead of the region of strong moisture gradient. The latter, which marks the dry line, slows down after collision with the sea breeze and the dry airmass arrives at the gulf coast at about 0200 EST on 29 September, comparable with the observed passage at about 0200 EST at Burketown and about 0230 EST at Karumba. While the accuracy of the detailed structures of the convergence lines in the calculation are hard to assess, the broad-scale features of evolution are certainly consistent with the observations.

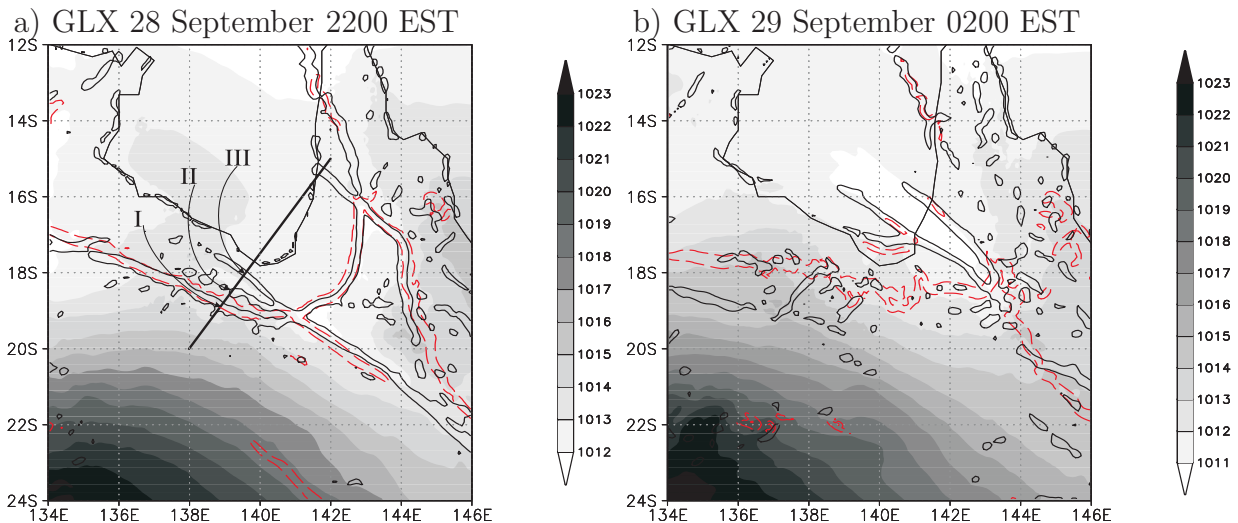


Figure 2.17: Legend as for Fig. 2.15b, but for (a) 2200 EST on 28 September, and (b) 0200 EST on 29 September. The black solid line in panel (a) indicates the position of the cross-section in Fig. 2.16b and the Roman numerals refer to the positions indicated in that figure.

Figure 2.18 shows the relative flow in the model,  $u - c$ , directly behind the two convergence lines (the moving cold front, and the bore wave ahead of it) at a height of  $\sigma = 0.965$  at selected times. Again  $u$  is the wind speed perpendicular to and towards the line in question and  $c$  is the propagation speed of that line (note that  $c$ 's are different for each line). In these calculations the orientation of the lines is  $\sim 60^\circ \pm 1^\circ$  at 1800 EST and  $\sim 57^\circ \pm 1^\circ$  at 2200 EST on 28 September and 0000 EST on 29 September, measured anticlockwise from north. The mean propagation speed of the cold front at 1800 EST on 28 September

is  $\sim 6.1 \text{ m s}^{-1}$ . The translation speeds of the morning glory at 2200 EST on 28 September and 0000 EST on 29 September are  $10.2 \text{ m s}^{-1}$  and  $12.2 \text{ m s}^{-1}$ , respectively. The errors in calculating these propagation speeds are estimated to be less than  $1 \text{ m s}^{-1}$ . It is seen that the relative flow on the southern side of the cold front is positive (i.e. towards the line) before the collision of the front and the south-coast sea breeze. As noted earlier, a positive value of  $u - c$  is indicative of a gravity current, while a negative value is characteristic of a bore-like disturbance. Figure 2.18 shows that  $u - c$  becomes negative behind the northward-moving line that emerges from the collision of the cold front and the sea-breeze front. After about 0000 EST on 29 September, the relative flow behind the morning glory is everywhere negative and its transition to a bore wave is complete.

The satellite imagery for this event did not show a distinct NACL since the region where the NACL usually occurs was covered by large cloud fields. The circumstances in the MM5 results, however, are more clear and it produced a convergence line along which the strength varies corresponding to an NACL (see fig. 2.23b and c, between  $140^\circ \text{ E}$  and  $141^\circ \text{ E}$ ). Figure 2.19 shows the relative flow in the model,  $u - c$ , directly behind the NACL convergence lines at a height of  $\sigma = 0.965$  at selected times. Again  $u$  is the wind speed perpendicular to and towards the line in question and  $c$  is the propagation speed of that line. In these calculations the orientation of the line is  $\sim 0^\circ \pm 1^\circ$  at 0000 EST, 0200 EST and 0400 EST on 29 September, measured anticlockwise from north. The mean propagation speed of the line is  $\sim 4.6 \text{ m s}^{-1}$ . The errors in calculating these propagation speeds are estimated to be less than  $1 \text{ m s}^{-1}$ . It is seen that the relative flow almost everywhere on the eastern side of the line is positive at all times (i.e. towards the line). Only behind the breaks in the convergence line, the plots show negative values. As noted earlier, a positive value of  $u - c$  is indicative of a gravity current, while a negative value is characteristic of a bore-like disturbance.

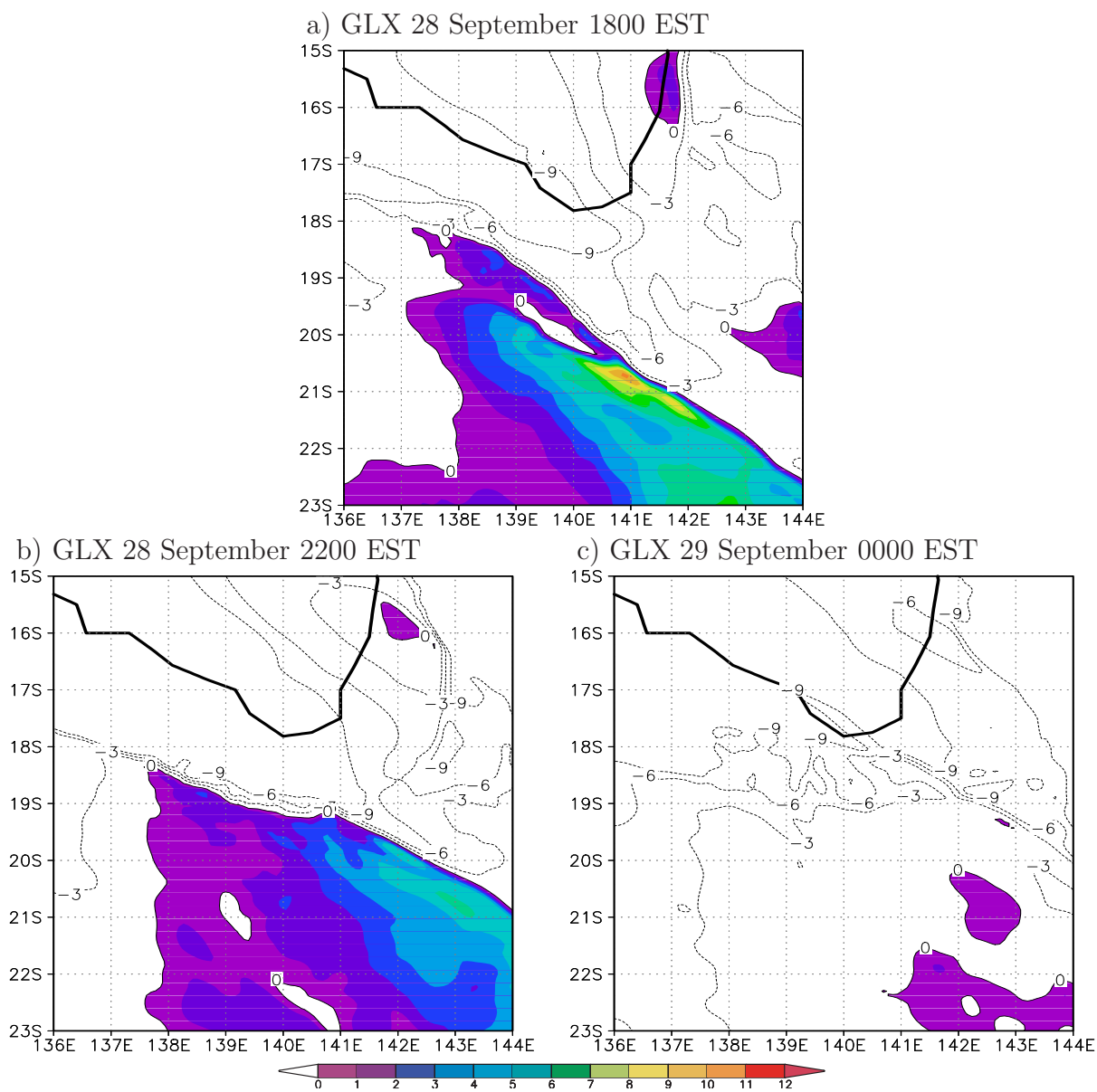
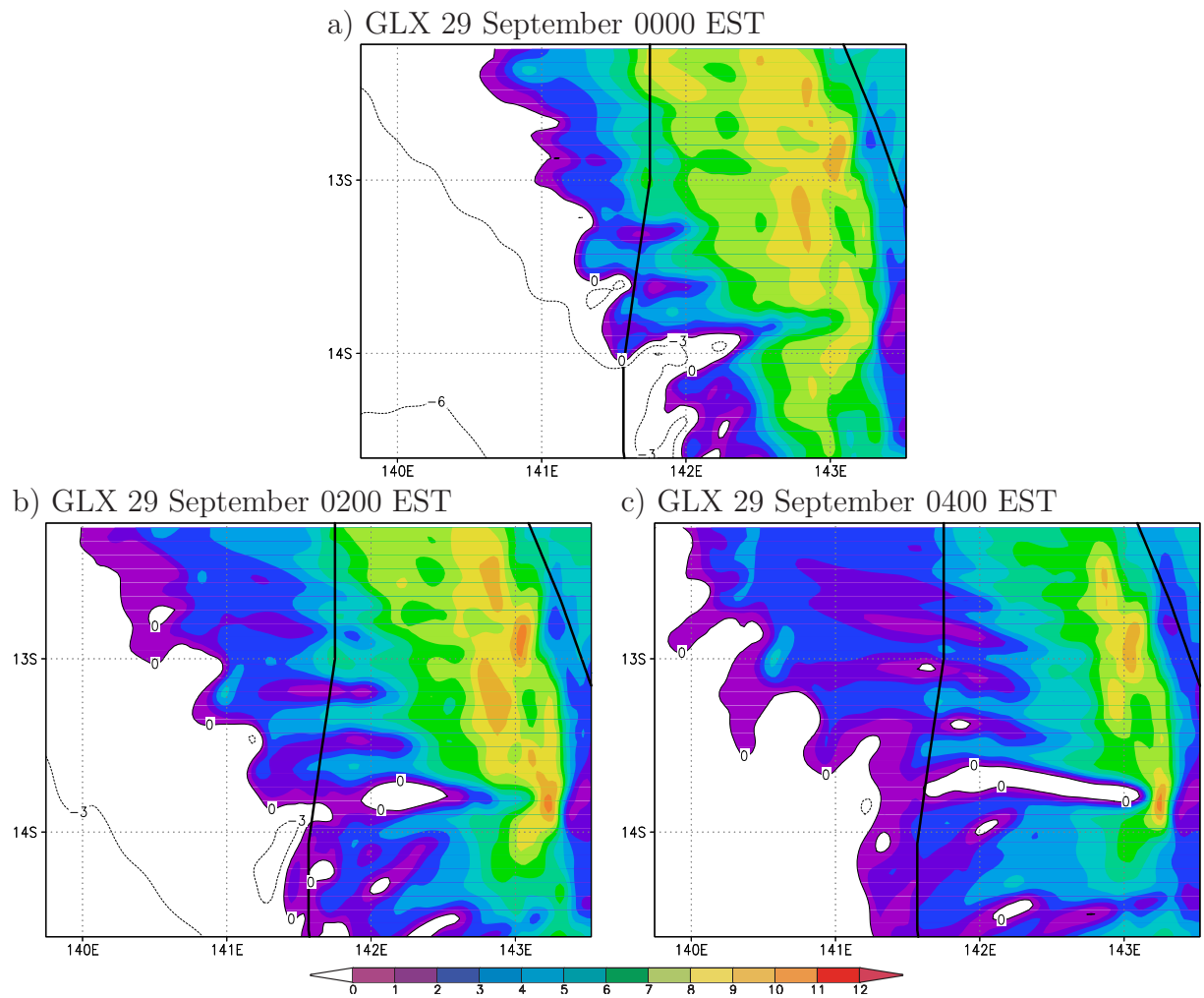


Figure 2.18: Legend as for Fig. 2.7, but for the relative flow normal to and behind cold front and the morning glory disturbance on 28 September. Positive values of  $u - c$  are shaded.



A vertical cross-section of virtual potential temperature,  $\theta_v$ , water vapour mixing ratio and horizontal wind vectors from (15.5°S, 141.5°E) to (13.5°S, 143°E) at 1800 EST and 2000 EST on 28 September, shortly before and shortly after the collision of the two sea breezes, is shown in Fig. 2.20. Inspection of the 1800 EST cross-section shows that, like in the previous simulation, the depth of the cold air behind the west-coast sea-breeze front is shallower and the air just behind the front is a little moister than that behind the east-coast sea-breeze front. Furthermore the horizontal gradient of  $\theta_v$  near the surface is largest across the west-coast sea-breeze front, suggesting that the east-coast sea breeze will rise above the west-coast sea breeze at collision, again like in the 03/04 October case.

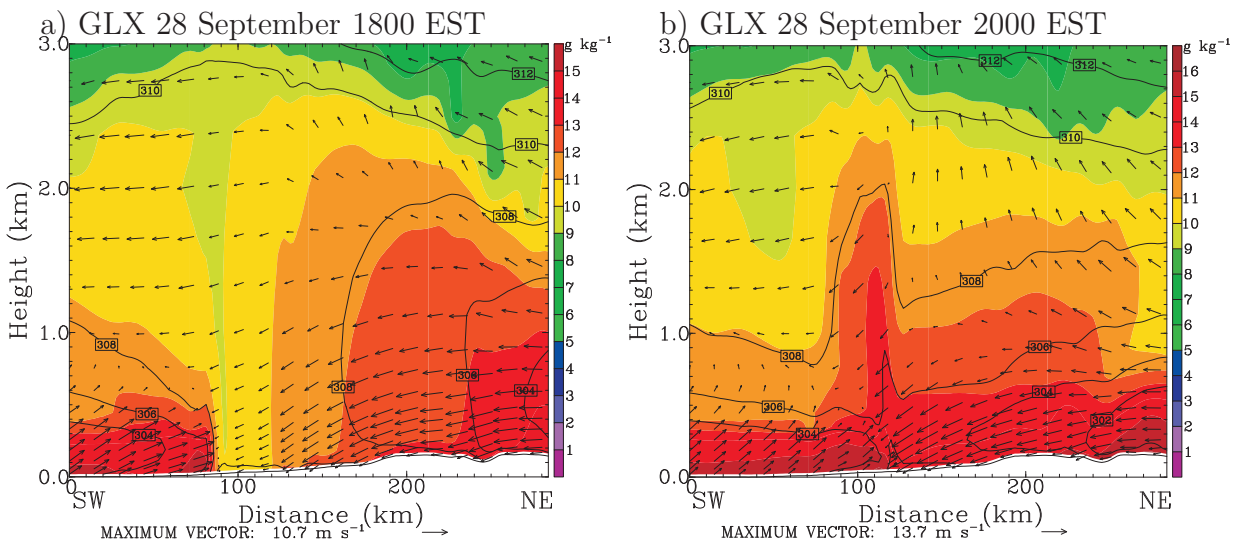


Figure 2.20: Vertical cross-section of virtual potential temperature (contour lines, interval 2 K), water vapour mixing ratio (shaded, in  $\text{g kg}^{-1}$ ) and horizontal wind vectors from the surface to 3 km at (a) 1800 EST and (b) at 2000 EST on 28 September. The cross-sections extend from 15.5°S on 141.5°E to 13.5°S on 143°E, a distance of about 300 km. Panel (a) shows the two sea breezes before their collision, and panel (b) after the collision.

Figure 2.21 shows the relative flow,  $u - c$ , directly behind the north-easterly morning glory at a height of  $\sigma = 0.965$  and at selected times, where  $u$  is the wind speed perpendicular to and towards the line in question and  $c$  is the propagation speed of that line. In these calculations the morning-glory line has an orientation of  $\sim 51^\circ \pm 1^\circ$  at 2200 EST on 28 September and  $\sim 48^\circ \pm 1^\circ$  at 0000 and 0200 EST on 29 September. The translation speeds of this line at these times are  $6.4 \text{ m s}^{-1}$ ,  $7.2 \text{ m s}^{-1}$  and  $7.2 \text{ m s}^{-1}$ , respectively. The errors in calculating these propagation speeds are estimated to be less than  $1 \text{ m s}^{-1}$ . It is seen that the relative flow behind, i.e. to the north-east of the line is positive (i.e. towards the line) after the collision of east- and west-coast sea breezes. As noted earlier, a positive value of  $u - c$  is indicative of a gravity current, while a negative value is characteristic of a

bore-like disturbance.  $u - c$  progressively declines behind the disturbance and eventually becomes negative. After about 0000 EST, the relative flow behind the morning glory is negative behind the line and its transition to a bore wave is complete.

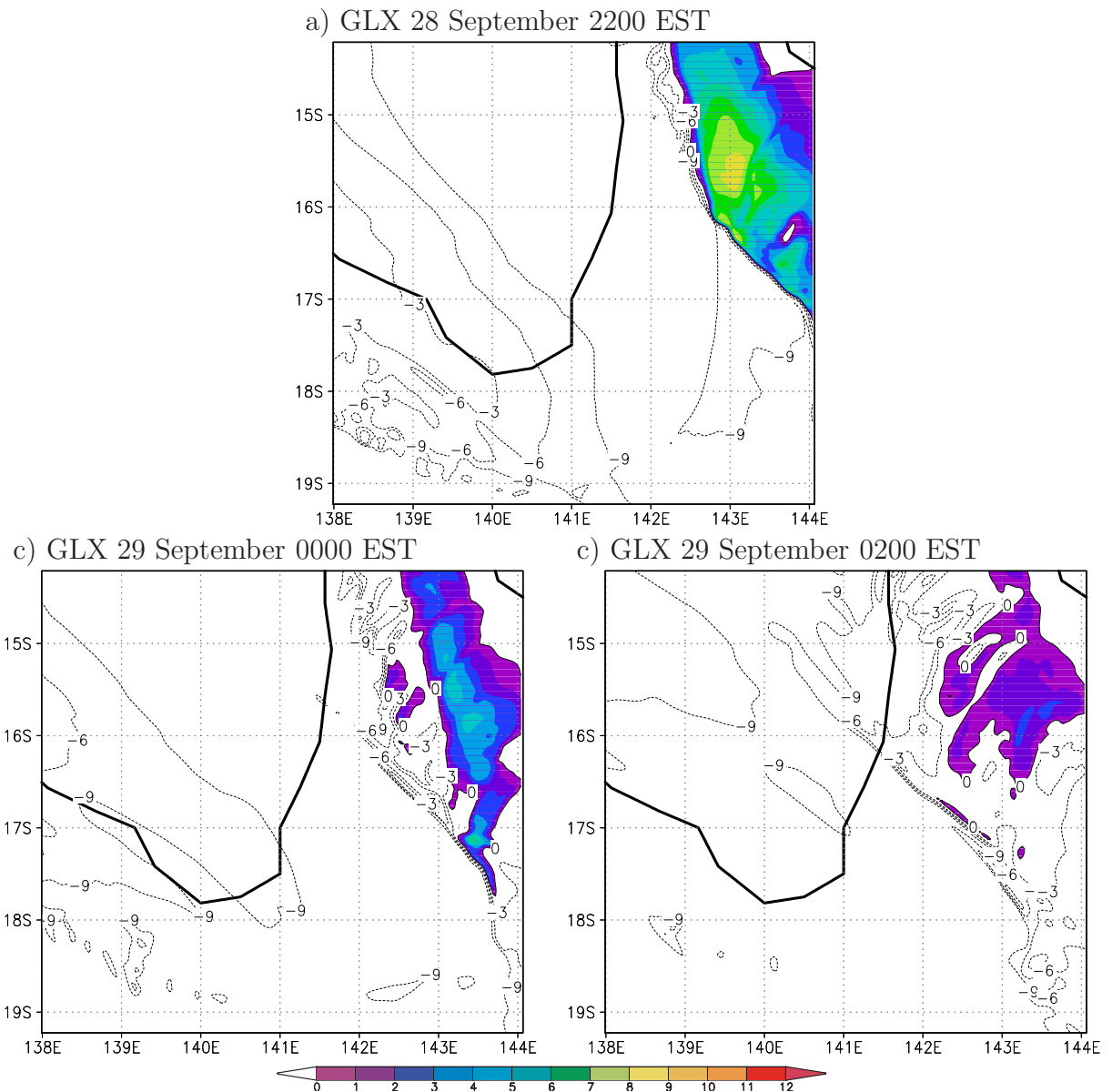


Figure 2.21: Legend as for Fig. 2.7, but for the relative flow normal to and behind the north-easterly morning glory disturbance on 28 and 29 September. Positive values of  $u - c$  are shaded.

Surface-pressure and wind plots at certain stations like those in Fig 2.3 are often difficult to interpret correctly because of the rather sparse temporal resolution of data outputs.

Though these plots were reasonably meaningful for the case of 03 October, this is the reverse for this and other cases. To avoid confusions from misinterpretable plots these are not shown for this and further cases. The surface pressure correlation coefficient, however, gives a reasonable assessment of the models' ability of capturing the situation. The correlation coefficients averaged over all available stations are  $r = 0.97$  for GLX,  $r = 0.95$  for BOM, and  $r = 0.84$  for LAPS.

## 2.5 08-09 October

Figure 2.22 shows the Japanese Geostationary Meteorological Satellite (GMS) image for the gulf region at 0632 EST on 09 October. On this date a southerly, south-easterly and north-easterly morning glory and their interaction over the gulf were documented in great detail by airborne measurements (Smith et al. 2005). The cloud line stretching from south to north and with a bend in the middle located west of the northern Cape York Peninsula is associated with an NACL. A series of cloud lines forming an arc with south-west-west to north-east-east direction in the south-eastern corner of the gulf is associated with a south-easterly morning glory. A pair of cloud lines located south of the gulf line stretching approximately parallel to the coast line is associated with a north-easterly morning glory. The southerly morning glory is visible only by a weak west-east oriented cloud line between the southerly and south-easterly morning glory on this day. The south-easterly morning glory was more extensive than the southerly one, which was confined approximately to the west of Mornington Island. It arrived at Karumba at 0505 EST, shortly before the north-easterly morning glory at 0530 EST.

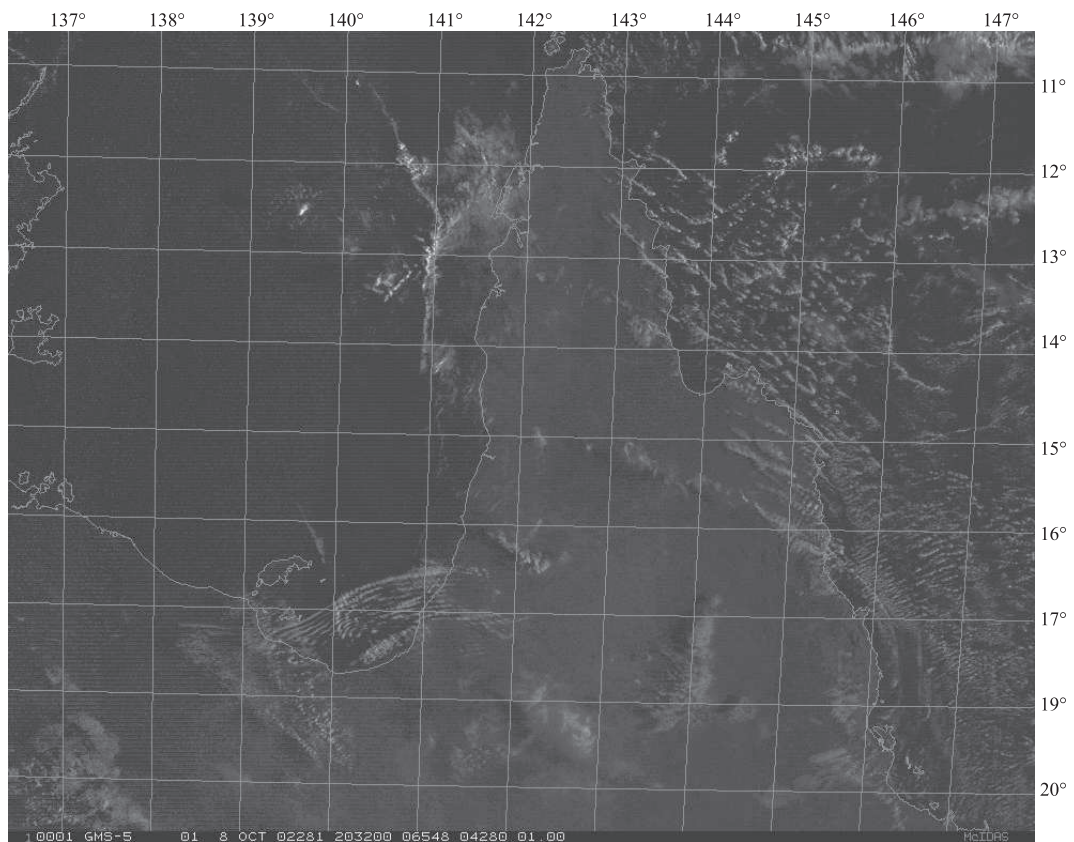


Figure 2.22: Satellite infrared picture of the cloud lines on 09 October at 0632 EST

The model calculation was initialised at 1000 EST on 08 October. Figure 2.23a shows the predicted low-level convergence at 0100 EST on 09 October in the GLX run. The convergence line with a north-westerly orientation over the southern part of the peninsula corresponds to the north-easterly morning glory. The convergence line about 200 km inland of the southern coastline corresponds to the southerly morning-glory. Its position is directly north of the sea-breeze front which is marked by a large arc of convergence inland of the Gulf of Carpentaria. Figure 2.23b-d compares the different predictions of low-level convergence at 0700 EST on 09 October, half hour later than the GMS satellite image in Fig. 2.22 was taken. The two MM5 runs produced convergence lines corresponding to the NACL, the southerly and north-easterly morning glories. As in the case of 03 October, the NACL was parallel to the east coast north of  $14.5^\circ$  and the north-easterly morning glory was parallel to the east coast south of  $14.5^\circ$ . The model did not develop separate disturbances corresponding to the southerly and south-easterly morning glories, but it did produce an extensive convergence line at the longitudes where the cloud lines were observed. The disturbance in the calculation corresponding to the north-easterly morning glory passed over Karumba at about 0500 EST (about half an hour earlier than observed), while the southerly disturbance arrived there at about 0600 EST (about half an hour later than observed). MesoLAPS produced a region of enhanced convergence in the south-eastern part of the gulf, but failed to create separate lines corresponding to the different morning glories and the NACL on this day. Plots of low-level wind divergence at other mesoLAPS output times show that the model created only a convergence line corresponding to the north-easterly morning glory.

As in the case of 03 October, model disturbances corresponding to the north-easterly morning glory and the NACL were generated following the collision of two sea breezes over Cape York Peninsula. Figure 2.24 shows vertical cross-sections of virtual potential temperature,  $\theta_v$ , water vapour mixing ratio and horizontal wind vectors from ( $15.5^\circ\text{S}$ ,  $141.5^\circ\text{E}$ ) to ( $13.5^\circ\text{S}$ ,  $143^\circ\text{E}$ ) at 1900 EST and 2000 EST, shortly before and after the collision of the two sea breezes. Inspection of the two cross-sections shows that the air behind the west-coast sea-breeze front is moister and warmer than behind the east-coast sea breeze, which is consistent with the fact that the sea-surface temperature in the east is cooler by about 2 K than in the gulf. As in the 03 October case, the gradient of  $\theta_v$  near the surface is largest across the west-coast sea-breeze front.

Figure 2.25 shows the relative flow in the model,  $u - c$ , directly behind the convergence line associated with the north-easterly morning glory at a height of  $\sigma = 0.965$  at selected times. Again  $u$  is the wind speed perpendicular to and towards the line and  $c$  is the propagation speed of the line. In these calculations the orientation of the line is  $\sim 38^\circ \pm 1^\circ$  at 2200 EST on 08 October,  $\sim 35^\circ \pm 1^\circ$  at 0000 EST and  $\sim 36^\circ \pm 1^\circ$  at 0200 EST on 09 October, measured anticlockwise from north. The translation speeds of the morning glory at 2200 EST on 08 October and at 0000 EST and 0200 EST on 09 October are  $9.0 \text{ m s}^{-1}$ ,  $9.0 \text{ m s}^{-1}$  and  $10.0 \text{ m s}^{-1}$ , respectively. The errors in calculating these propagation speeds

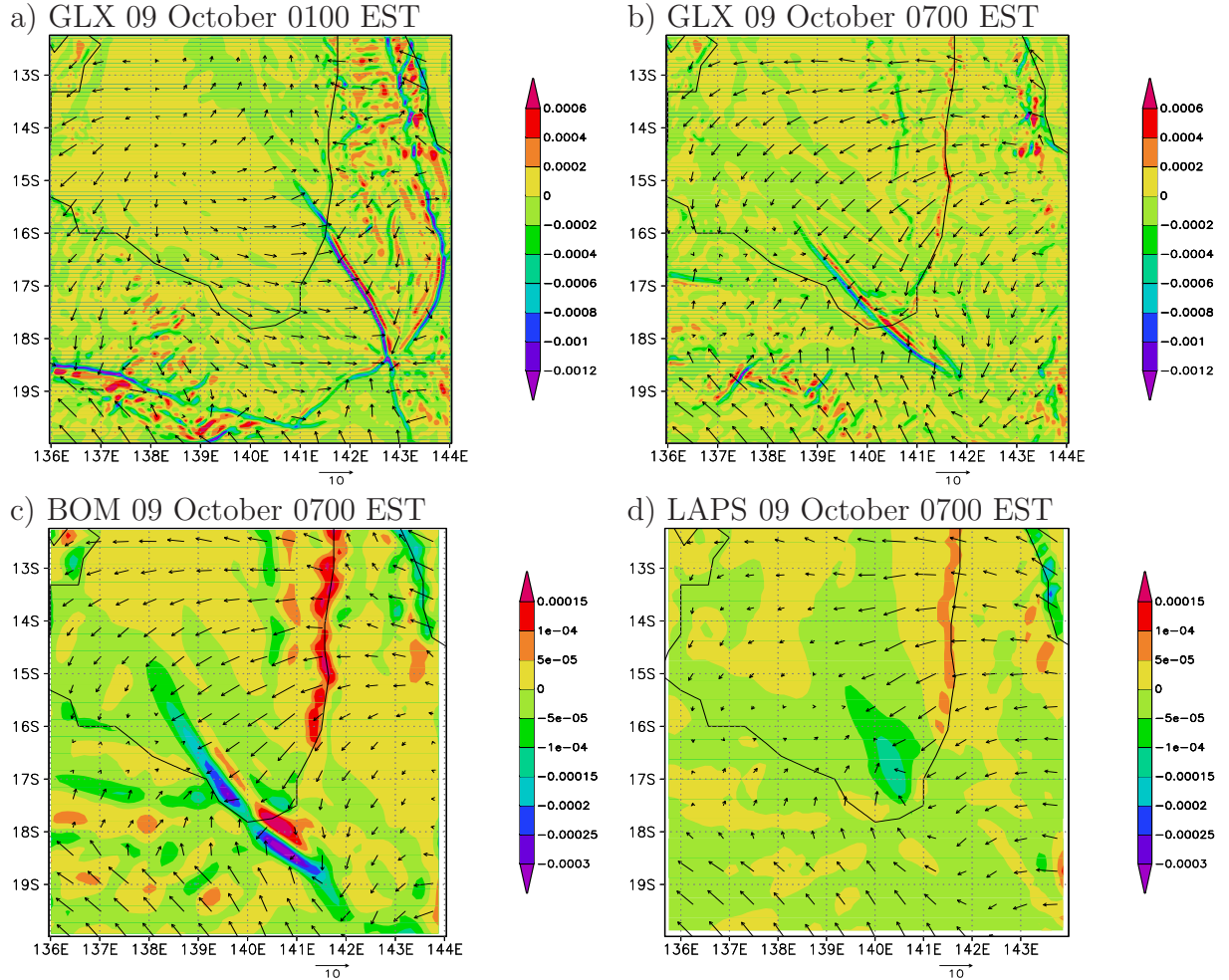


Figure 2.23: Low-level wind vectors (scale  $10 \text{ m s}^{-1}$  below each panel) and divergence (shaded, unit  $\text{s}^{-1}$ ) in the GLX calculation at (a) 0100 EST and (b) 0700 EST on 09 October. Panels (c) and (d) show the corresponding fields for the BOM and mesoLAPS calculations, respectively, at 0700 EST. The plots for the GLX and BOM fields are at  $\sigma = 0.9975$ , and that for mesoLAPS at 1025 mb. Panel (b) to (d) should be compared with the infrared satellite image in Fig. 2.22, which is valid 28 min. before. Note that the contour interval for divergence is different in the lower panels.

are estimated to be less than  $1 \text{ m s}^{-1}$ . It is seen that the relative flow north-eastwards of the morning-glory disturbance is positive shortly after the collision. As noted earlier, a positive value of  $u - c$  is indicative of a gravity current, while a negative value is characteristic of a bore-like disturbance. Figure 2.25b shows that the relative flow has decayed two hours later and becomes negative at 0000 EST on 09 October, as shown in Fig. 2.25c. This transition to a bore is very similar to the case of 03 October.

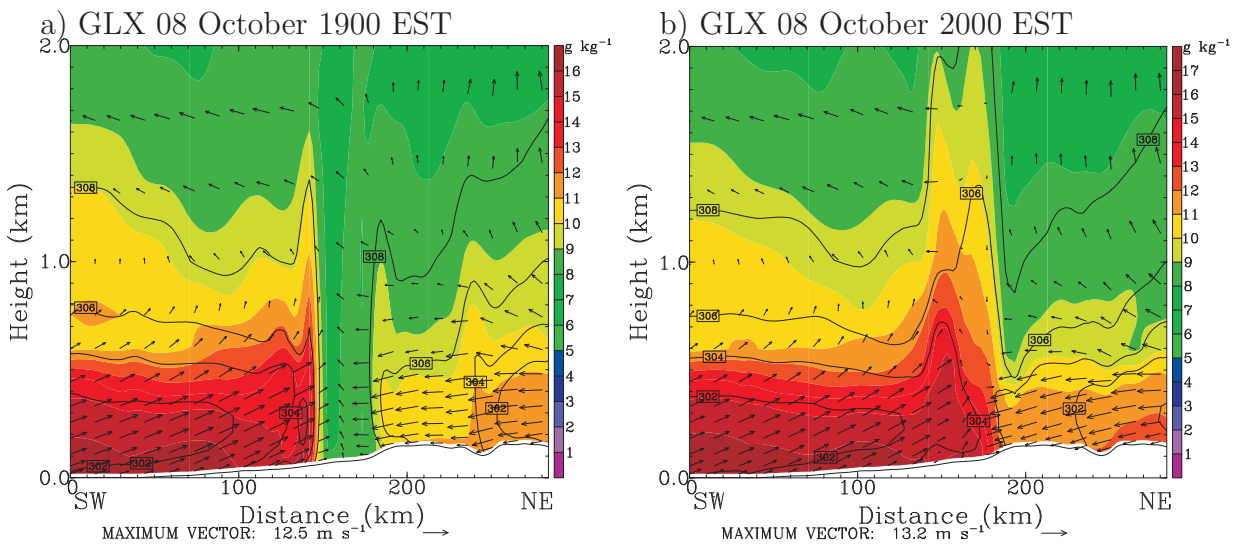


Figure 2.24: Vertical cross-section of virtual potential temperature (contour lines, interval 0.5 K), water vapour mixing ratio (shaded, in  $\text{g kg}^{-1}$ ) and horizontal wind vectors from the surface to 2 km at (a) 1900 EST, and (b) 2000 EST on 08 October. The cross-sections extend from  $15.5^\circ\text{S}$  on  $141.5^\circ\text{E}$  to  $13.5^\circ\text{S}$  on  $143^\circ\text{E}$ . In (a) the two sea breezes are about to collide and (b) is just after the collision.

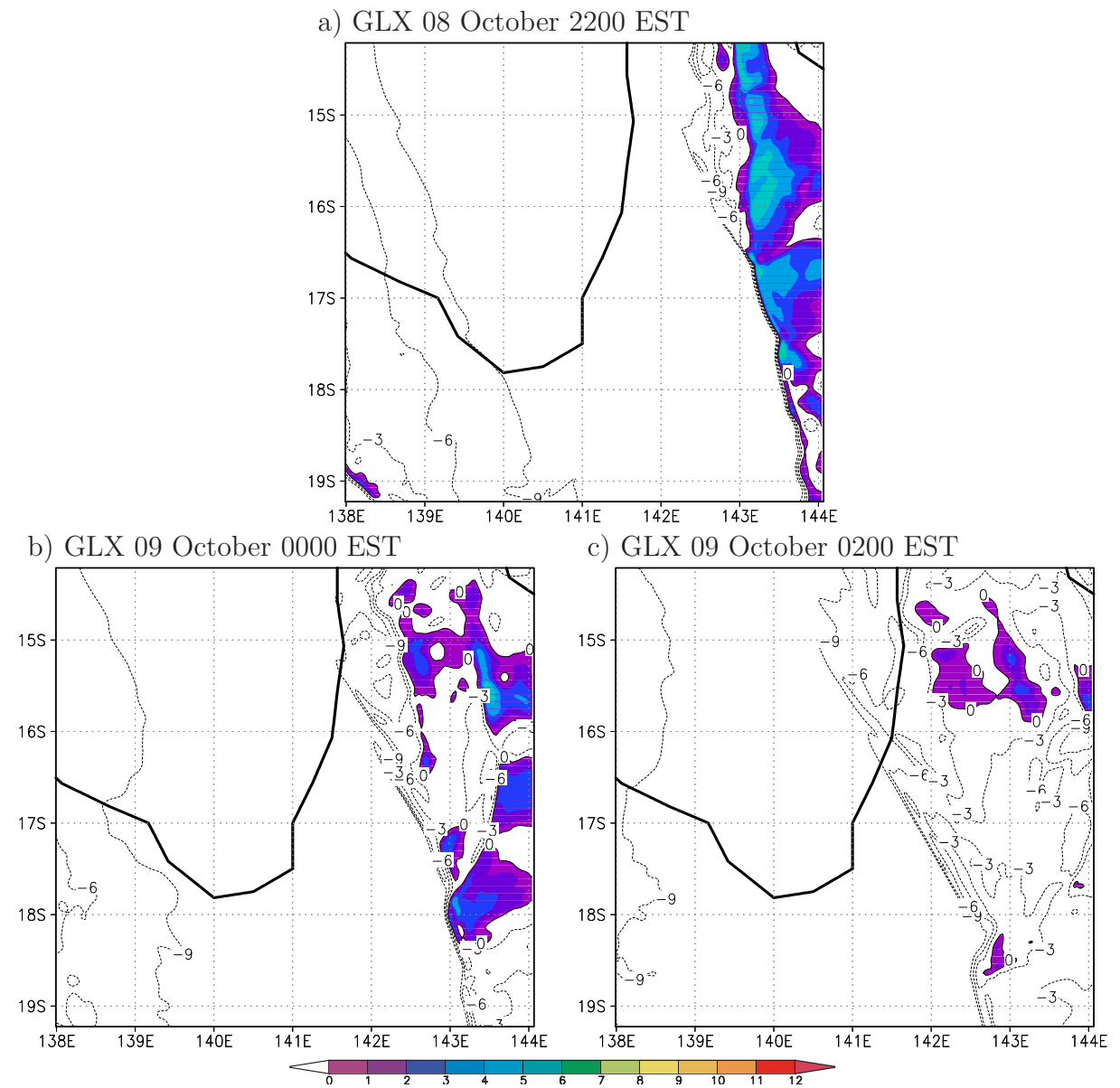


Figure 2.25: Legend as for Fig. 2.7, but for the relative flow normal to and behind the north-easterly morning-glory disturbance on 08 and 09 October. Positive values of  $u - c$  are shaded.

As in the 28/29 September event, a southerly disturbance in the model was generated following the collision of a nocturnal cold front and the sea-breeze front from the southern gulf coast. This cold front was moving from the south following a trough of low pressure. The synoptic situation for this event is exemplified by the MSLP analysis for 2200 EST 08 October shown in Fig. 2.26. An anticyclone centred in the Great Australian Bight extends a ridge almost to the southern gulf coast, while the inland trough (marked by the dashed line in this figure) over northern Australia lies just south of the coast. The prominent north-eastward pointing bump in the trough axis located south of Cape York Peninsula gives a possible explanation for the occurrence of a south-easterly morning glory. Predicting the correct shape of the trough line correctly is beyond the expectations from the ECMWF data sets. Especially for the southerly and south-easterly events, the MM5 results cannot be better than the initial conditions allow, since they rely on the correct position of the inland trough. South-easterly morning glories are not yet fully understood, but assumed generation mechanisms have been linked to the Great Dividing Range (see Fig. 1.7c) which is located along the east coast of the continent (Reeder *et al.* 1995).

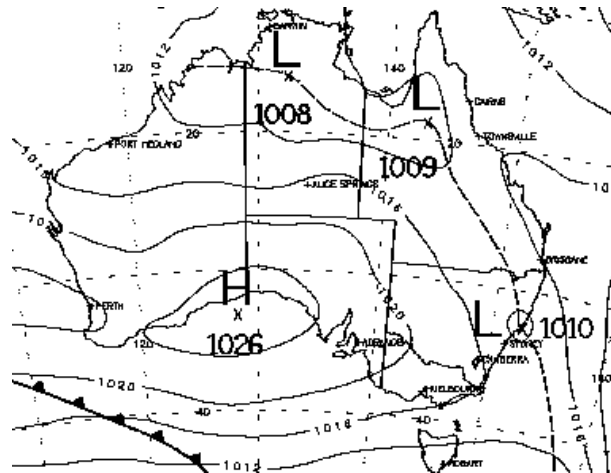


Figure 2.26: Trough line in the Gulf of Carpentaria region at 2200 EST on 08 October, marked by a dashed line (adapted from Bureau of Meteorology mean sea level analysis).

Figure 2.27 shows vertical cross-sections of virtual potential temperature,  $\theta_v$ , water vapour mixing ratio and horizontal wind vectors from 20°S on 138°E to 15°S on 142°E, a distance of about 750 km, at 2200 EST on 08 October (panel a) and at 0000 EST on 09 October (panel b). The course of events during the generation of the southerly morning glory is the same as in the case described in the previous section. At 2200 EST the inland trough coincides with the region of warmest and driest air. The low-level flow to the north-east of the trough is moist and corresponds to the sea breeze from the southern gulf coast. On the right of panel (b), the disturbance corresponding to the north-easterly morning

glory is evident by the sharp jump in the isentropes.

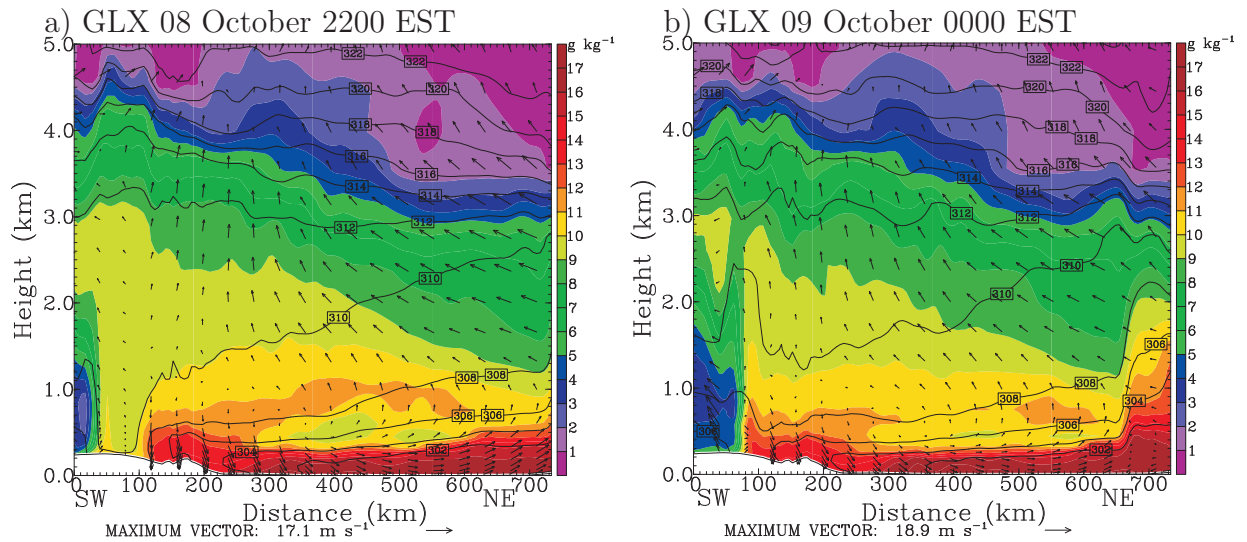


Figure 2.27: Vertical cross-section of virtual potential temperature (contour lines, interval 2 K), water vapour mixing ratio (shaded, in  $\text{g kg}^{-1}$ ) and horizontal wind vectors from the surface to 5 km at (a) 2200 EST on 08 October, and (b) 0000 EST on 09 October. The cross-sections extend from  $20^{\circ}\text{S}$  on  $138^{\circ}\text{E}$  to  $15^{\circ}\text{S}$  on  $142^{\circ}\text{E}$ , a distance of about 750 km. Panel (a) shows the nocturnal front and the sea breeze south of the gulf before their collision near Mount Isa, and panel (b) after the collision. The right panel shows also the disturbance corresponding to the north-easterly morning glory.

Moreover, the southerly disturbance shows a clear separation of the convergence line and the dry line behind the nocturnal cold front as in the case of 28 September. Figure 2.28 shows the mean sea level pressure and regions of strong convergence and strong gradients of water vapour mixing ratio at 2300 EST on 08 October and 0400 EST on 09 October. In the left panel the south-coast sea breeze is marked by an arc of strong convergence and moisture gradient inland of the coast. The position of the trough line is indicated by a band of low mean sea level pressure. There is strong convergence on the southern side of the sea-breeze front. As in the cases described earlier, this convergence on the northern periphery of the region of the southerly ageostrophic flow towards the trough has led to frontogenesis and the band of strong moisture gradient at the southern edge of the trough line, coinciding with a strong temperature gradient (see Fig. 2.27), marks a cold front. The collision of the cold front and the sea breeze has just commenced. The right panel shows the situation 5 h later when the convergence line corresponding to the southerly morning-glory line has moved to the north of the dry line. The translation speed of the dry line has slowed down after the collision. The passage of the dryline at Augustus Downs occurred at about 0700 EST, very close to the observed time there, but the trough line in the model did not move north of  $18^{\circ}$ , consistent with the observations.

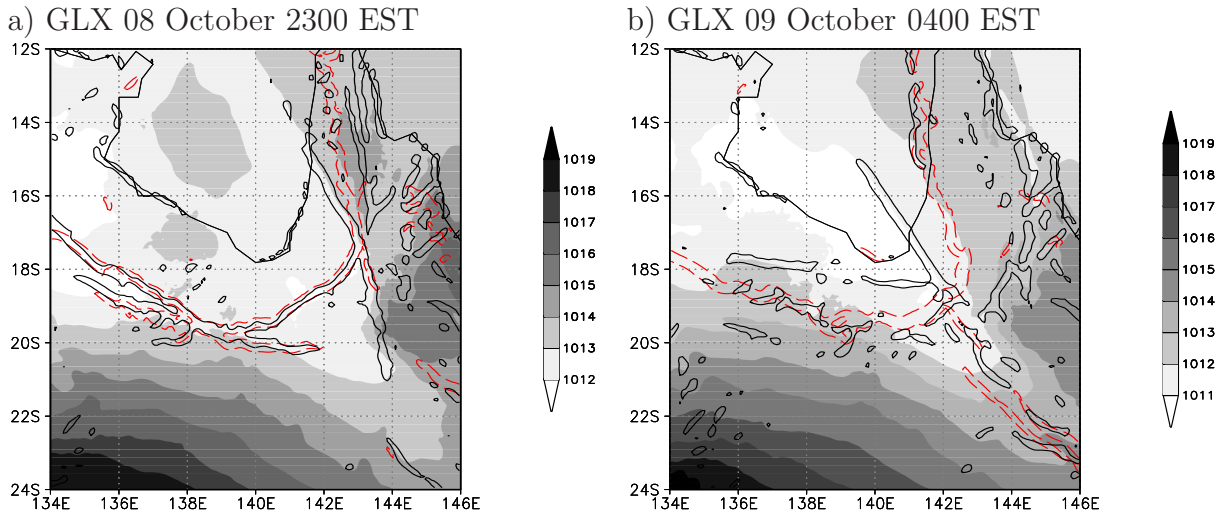


Figure 2.28: Legend as for Fig. 2.15b, but for (a) 2300 EST on 08 October, and (b) 0400 EST on 09 October.

Figure 2.29 shows the relative flow in the model,  $u - c$ , directly behind the convergence lines associated with the cold front and the southerly morning glory at a height of  $\sigma = 0.965$  at selected times. Again  $u$  is the wind speed perpendicular to and towards the line in question and  $c$  is the propagation speed of that line. In these calculations the orientation of the line is  $\sim 75^\circ \pm 1^\circ$  at 2200 EST on 08 October,  $\sim 72^\circ \pm 1^\circ$  at 0000 EST on 09 October and  $\sim 75^\circ \pm 1^\circ$  at 0200 EST on 09 October, measured anticlockwise from north. The translation speeds of the morning glory at these times are  $6.1 \text{ m s}^{-1}$ ,  $6.1 \text{ m s}^{-1}$  and  $10.2 \text{ m s}^{-1}$ , respectively. The errors in calculating these propagation speeds are estimated to be less than  $1 \text{ m s}^{-1}$ . It is seen that the relative flow southwards of the morning-glory disturbance is negative after the collision. Note that at 0000 EST and 0200 EST on 09 October, the morning-glory convergence line has moved north of the shaded region, which indicates the sea-breeze front at those times. As noted earlier, a positive value of  $u - c$  is indicative of a gravity current, while a negative value is characteristic of a bore-like disturbance.

Figure 2.30 shows the low-level divergence in the high-resolution run at 1400 EST (a) and the satellite picture at 1426 EST on 09 October (b). The model captured a convergence line corresponding to the NACL, the position of which at 1330 EST (over 27 h after the initial time), was close (within about 25 km) to the position in the satellite image at that time.

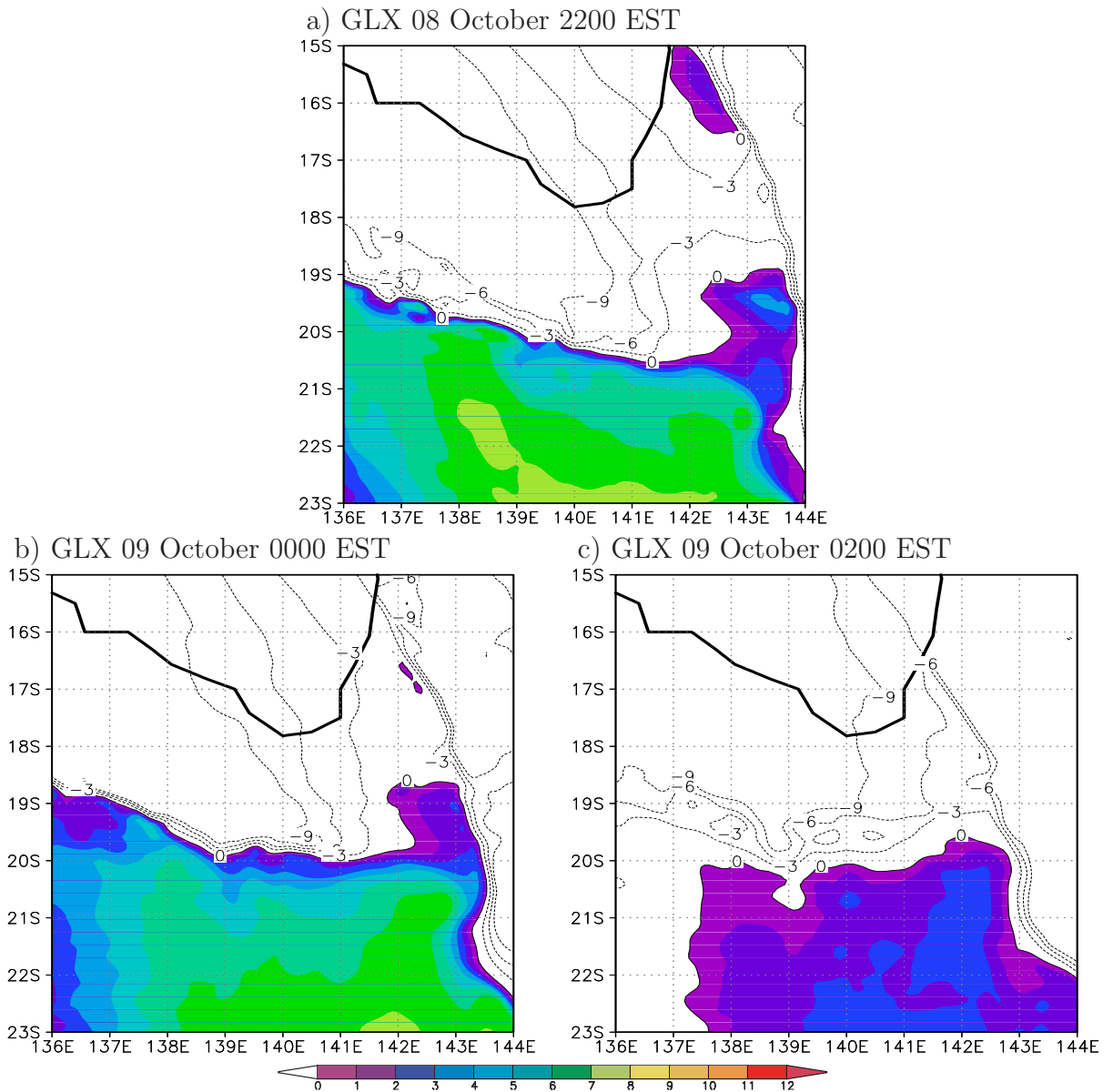


Figure 2.29: Legend as for Fig. 2.7, but for the relative flow normal to and behind the cold front and the southerly morning glory disturbance on 08 and 09 October. Positive values of  $u - c$  are shaded.

As in the event of 28/29 September, the strength of convergence varied along the line corresponding to the NACL on this day. Figure 2.31 shows the relative flow in the model,  $u - c$ , directly behind the NACL convergence lines at a height of  $\sigma = 0.965$  at selected times. Again  $u$  is the wind speed perpendicular to and towards the line in question and  $c$  is the propagation speed of that line. In these calculations the orientation of the line is

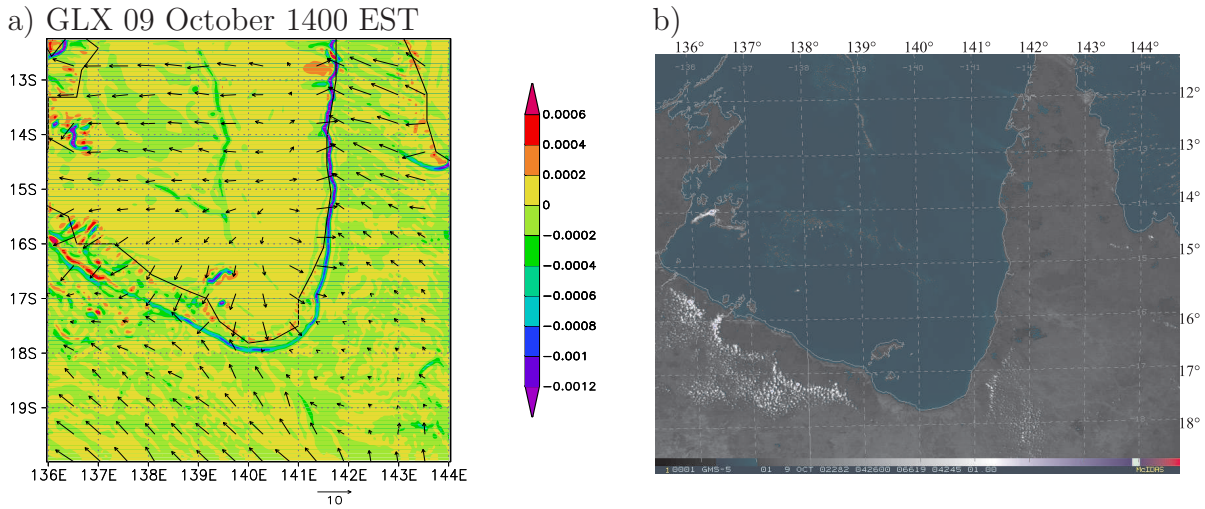


Figure 2.30: (a) Low-level wind vectors (scale  $10 \text{ m s}^{-1}$  below panel) and divergence (shaded, unit  $\text{s}^{-1}$ ) for the GLX simulations at  $\sigma = 0.9975$  at 1400 EST on 09 October. (b) GMS visible satellite image at 1426 EST on the same day.

$\sim 0^\circ \pm 1^\circ$  at 0400 EST, 0600 EST and 0800 EST on 09 October, measured anticlockwise from north. The mean propagation speed of the line is  $\sim 6.3 \pm 0.5 \text{ m s}^{-1}$  at 0400 EST and  $\sim 5.4 \pm 0.5 \text{ m s}^{-1}$  at 0600 EST and 0800 EST. It is seen that the relative flow almost everywhere on the eastern side of the line is positive at all times (i.e. towards the line). Only behind the breaks in the convergence line, the plots show negative values. As noted earlier, a positive value of  $u - c$  is indicative of a gravity current, while a negative value is characteristic of a bore-like disturbance.

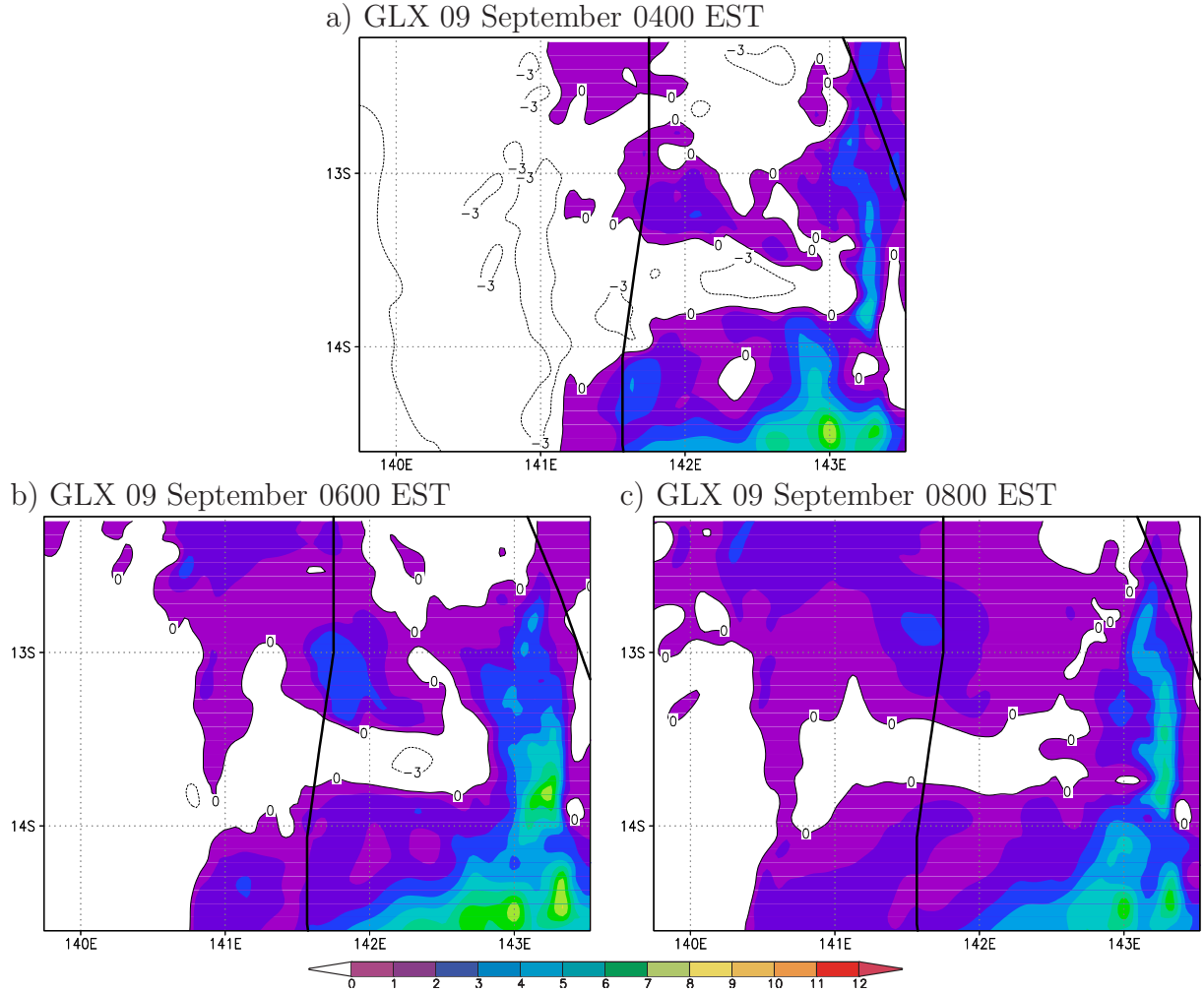


Figure 2.31: Legend as for Fig. 2.7, but for the relative flow normal to and behind NACL convergence line on 09 October. Positive values of  $u - c$  are shaded.

Figure 2.32 shows the evolution of the two morning-glory convergence lines in the model. Where the lines overlap, the strength of the convergence is enhanced, but their propagation speed does not change after passing through each other (note that both lines have bore-like properties at this time). This supports the results of a case study by Reeder *et al.* (1995), which suggests that morning glories are sufficiently stable to survive strong nonlinear interactions.

The surface pressure correlation coefficient for this event averaged over all available stations is  $r = 0.94$  for BOM,  $r = 0.93$  for GLX and  $r = 0.68$  for LAPS. The fact that the correlation coefficient is a little lower for the high-resolution MM5 run than for the lower resolution run shows once more that increasing the resolution does not necessarily increase

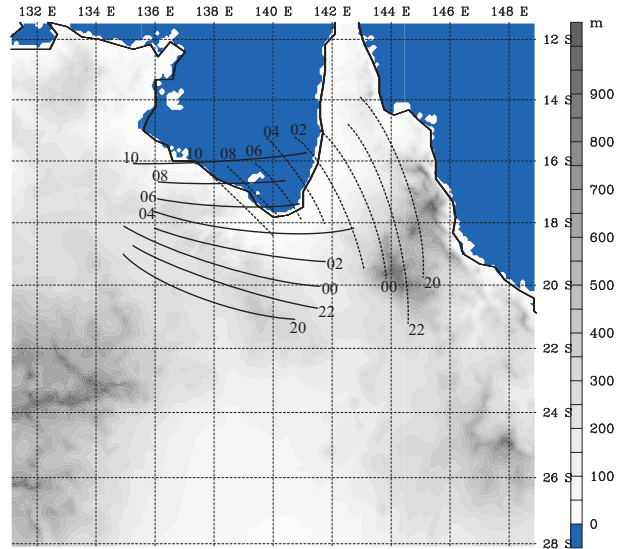


Figure 2.32: Surface orography (shaded). The dashed thick lines show the position of the easterly sea breeze and later north-easterly morning-glory disturbance and the solid thick lines show the position of the southerly morning-glory disturbance at the labelled times in hours, beginning at 2000 EST on 08 October and ending at 1000 EST on 09 October.

the skill of the model based on this criterion.

## 2.6 09-10 September



Figure 2.33: Southerly morning glory, picture taken by Roger K. Smith at Karumba in the morning of 10 September.

On 10 September, a major southerly morning glory, an NACL and a north-easterly morning glory were observed in the satellite imagery. A spectacular southerly morning-glory cloud formation was seen from the ground at Karumba (see Fig. 2.33), preceded by the pressure signature of the passage of a weaker north-easterly morning glory. Figure 2.34 shows the GMS satellite image for the gulf region at 0825 EST on 10 September. The arc of broken cloud over the northern part gulf is an NACL and the series of cloud lines over the south-eastern coastal region is the southerly morning glory. There is a lightly ragged band of cumulus clouds to the east of the leading southerly morning-glory cloud line, stretching from the eastern end of the morning glory to the east coast of the continent. An animation of low-level moisture fields from the MM5 run suggests that this band has its origin not in the southerly morning-glory disturbance. Rather it is produced by moist

sea-breeze air, being lifted over the northern foothills of the Great Dividing Range (see Fig. 1.7c). Animations of low-level wind divergence and vertically integrated cloud water suggest that the north-easterly morning-glory line might have triggered this cloud band, which would explain its observed orientation. The north-easterly morning glory is marked by the single north west-west to south east-east orientated cloud line south of the eastern half of the leading southerly morning-glory cloud line.

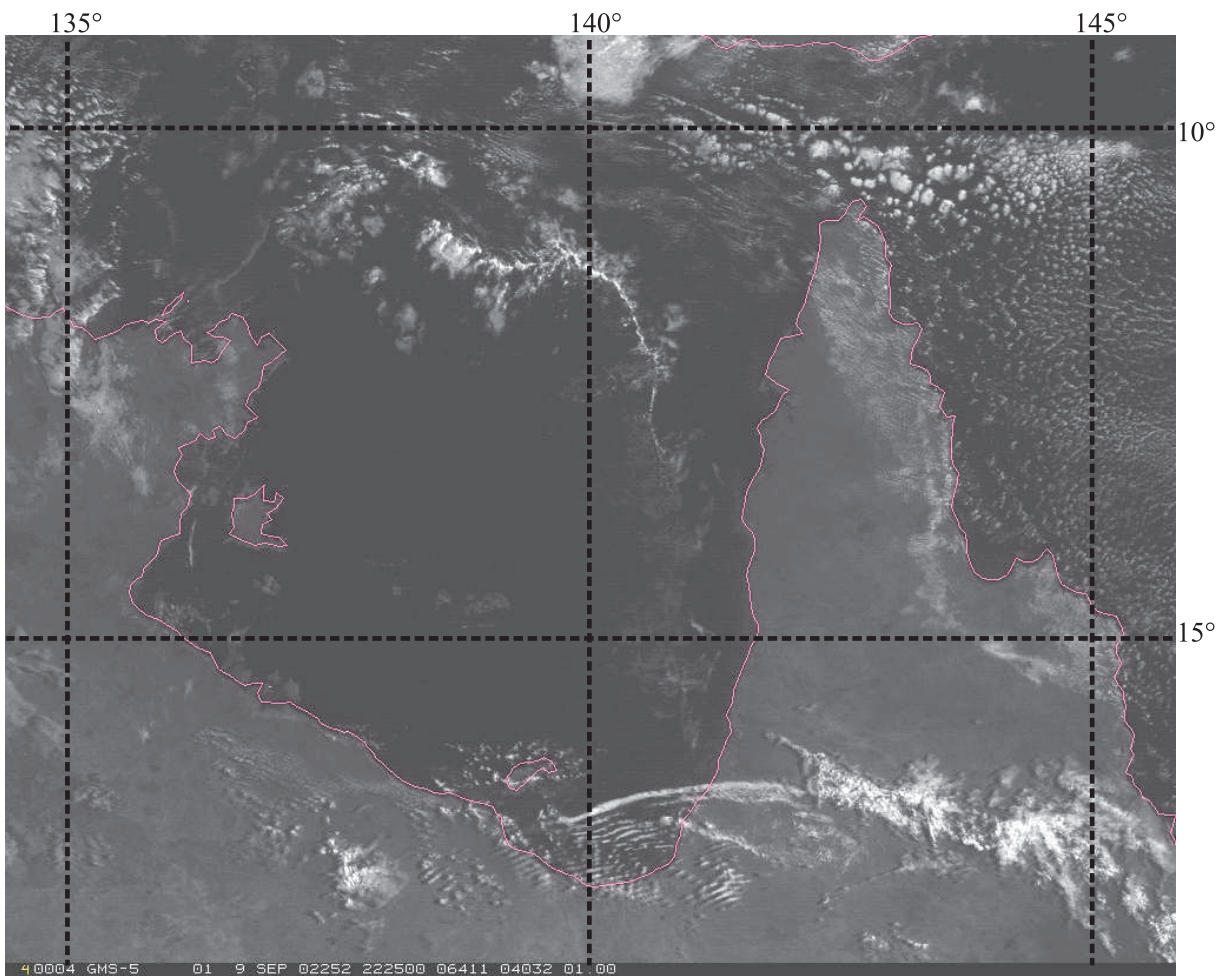


Figure 2.34: GMS visible image of the Gulf of Carpentaria region at 0825 EST on 10 September.

This event was at the beginning of the GLEX experiment when only two AWS stations (Karumba and Mornington Island) were operating. Therefore it was not possible to calculate a correlation coefficient as was done for the other events. Nevertheless, there was evidence in the AWS data of the passage of a weak north-easterly disturbance at Karumba at 0350 EST, while the southerly morning glory arrived there at 0645 EST. Only the

southerly disturbance was observed at Mornington Island (at 0920 EST). In the model the northeasterly disturbance arrived around 0500 EST at Karumba and the southerly disturbance arrived around 0800 EST at Karumba and around 1000 EST at Mornington Island. The timing differences between model and observations show that the model captures the timing of the north-easterly disturbance more correctly than the timing of the southerly disturbance in this case.

For this event, no mesoLAPS forecasts were available and hence no BOM simulation was carried out. The evolution of the convergence lines in the GLX run is shown in Fig. 2.35. The calculation, initialised at 1000 EST on 09 September, produced weaker convergence lines associated with southerly morning glory and NACL than for the other cases and the scaling for the plots of low-level wind divergence had to be adjusted accordingly. Unfortunately, the westward bend of the northern half of the NACL is outside the domain of the MM5 simulation. At 2200 EST on 09 September the gulf sea breeze has already travelled far inland, about 100 km over Cape York Peninsula and about 200 km over the southern gulf region. The northern part of the east-coast sea breeze has already collided with the west-coast sea breeze and a convergence line, having roughly the orientation of the east coast south of  $14^{\circ}$  S has moved to the south-west. The convergence patterns south of the south-coast sea breezes are not associated with the approaching trough line, which is still located south of the domain boundaries at this time.

By 0200 EST on 10 September, the collision of the nocturnal cold front, which has been generated by convergence towards the trough line and the south-coast sea breeze has already occurred and the convergence lines north of the sea-breeze front associated with the southerly morning glory have moved northwards. The collision of the east- and west-coast sea breezes over the peninsula has occurred and the convergence line related to the north-easterly morning glory has propagated further to the south-west. A broken convergence line associated with the NACL has formed along the west coast.

By 0400 EST both southerly and north-easterly morning-glory convergence lines have continued their propagation towards the south-eastern tip of the gulf and the convergence line related to the NACL has moved a little further across the gulf. The north-eastern morning-glory line is situated approximately 50 km north-east of Karumba, where the line was observed at 0350 EST. Thus the arrival time at Karumba is on the order of an hour late. The divergence plot shows the north-western end of the north-easterly disturbance a little to the east of  $139.5^{\circ}$  E, which is consistent with the observation that there was no north-easterly morning glory over Mornington Island on this day.

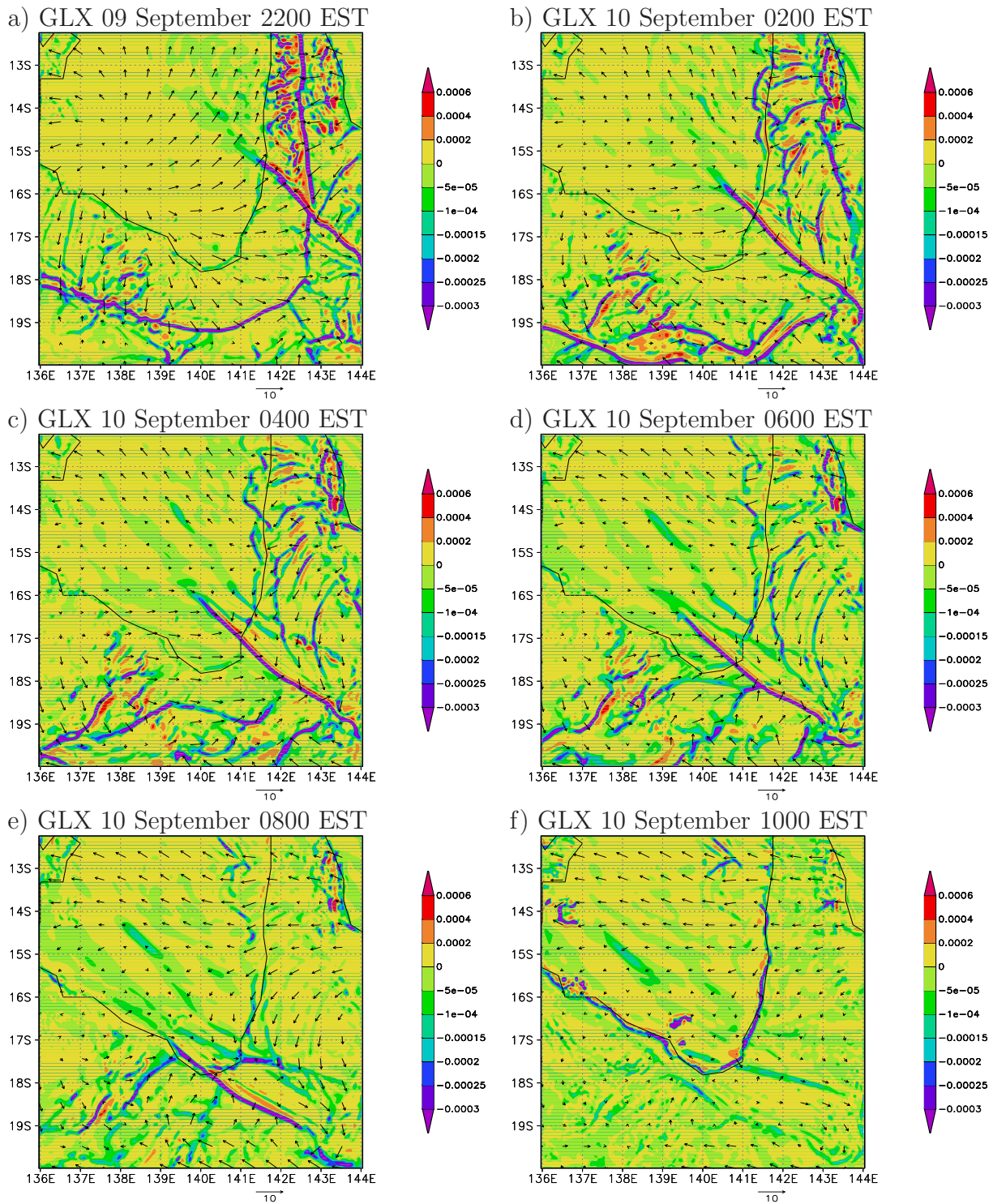


Figure 2.35: Sequence of plots of wind vectors (scale  $10 \text{ m s}^{-1}$  below each panel) and divergence (shaded, unit  $\text{s}^{-1}$ ) at  $\sigma = 0.9975$  for the GLX run at times indicated above each plot. The domain size is  $900 \text{ km} \times 900 \text{ km}$ .

At 0600 EST the southerly morning-glory convergence line is located about 20 km south of the southernmost tip of the gulf. This is in good agreement with the satellite image from 0526 EST in Fig 2.35 b, which shows a line of cloud very close to this position. The NACL convergence line has moved further to the west, having slightly reduced in intensity. The collision of both morning-glory lines at the western end of the southerly convergence line has just commenced.

By 0800 EST the convergence lines corresponding to both morning glories have passed through each other, with little or no disruption. At Karumba the southerly disturbance was observed at 0645 EST and in the model it arrived about 75 min. late, around 0800 EST. The situation at this time can be compared with the satellite image in Fig. 2.34. The NACL has further weakened on its way to the west. By 1000 EST, the NACL and the morning-glory lines have almost disappeared. The southerly morning glory was observed at Mornington Island at 0920 EST, but the model failed to move this convergence line that far north.

Figure 2.36 shows an MSLP analysis of the Australian region at 2200 EST on 09 September. The position of the trough line south of the Gulf of Carpentaria suggests a generation mechanism for the southerly morning glory similar to those described in the previous sections.

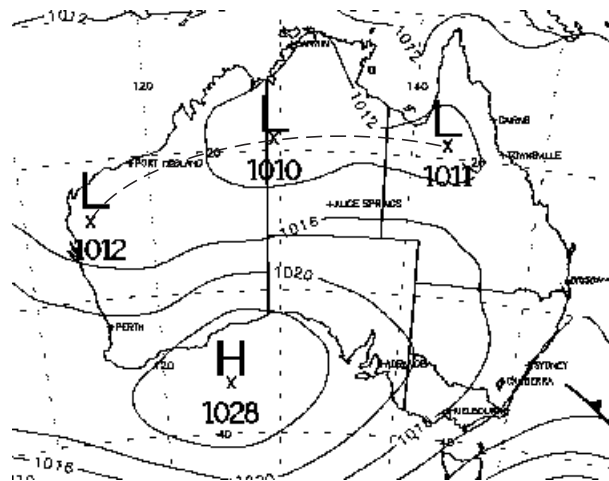


Figure 2.36: MSLP analysis at 2200 EST on 09 September adapted from the Bureau of Meteorology. The trough line in the Gulf of Carpentaria region is indicated by a dashed line.

Figure 2.37 shows regions of horizontal wind convergence with magnitude exceeding  $6 \times 10^{-5} \text{ s}^{-1}$  and regions where the horizontal gradient of water vapour mixing ratio exceeds  $8 \times$

$10^{-4} \text{ km}^{-1}$ . Panel (a) shows that the collision of the developing cold front and the sea-breeze front, indicated by strong convergence and large moisture gradient, has just commenced at 0000 EST on 10 September. The southerly convergence line is not accompanied by a region of strong moisture gradient unlike that seen in the other cases. Panel (b) shows that four hours later, at 0400 EST on 10 September, a convergence line associated with the southerly morning glory has emerged from the collision in panel (a) and propagates northwards. Both panels show also the convergence line associated with the north-easterly morning glory propagating towards the south-west.

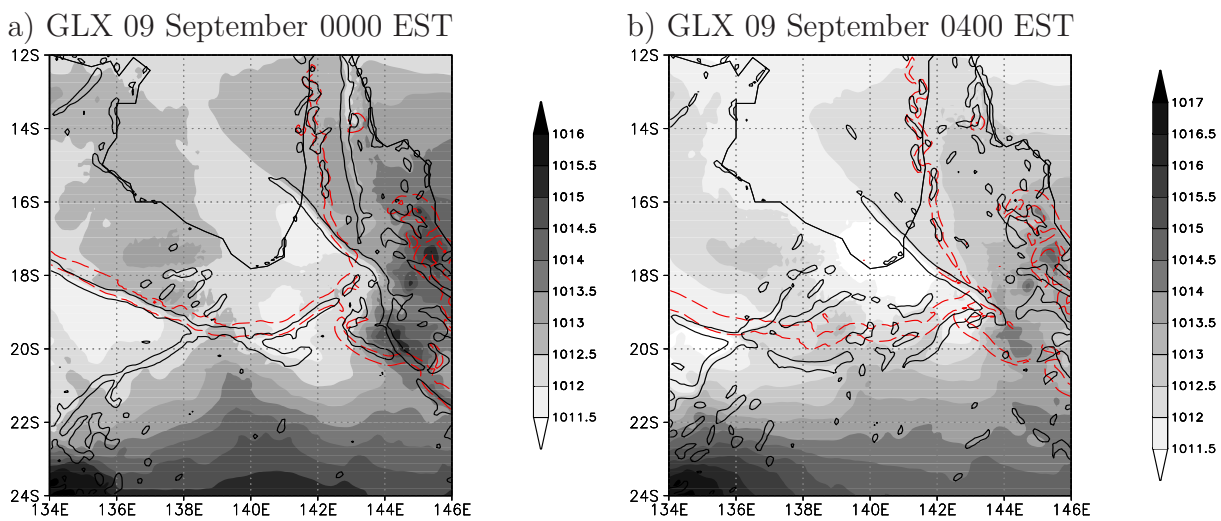


Figure 2.37: Mean sea level pressure is shaded and solid black lines show the region where the low-level wind divergence is less than  $-6 \times 10^{-5} \text{ s}^{-1}$  indicating strong convergence. Dashed red lines show where the water vapour mixing ratio gradient exceeds  $8 \times 10^{-4} \text{ km}^{-1}$ . Panel (a) shows the situation at 0000 EST on 09 September, and (b) at 0400 EST on 10 September.

Figure 2.38 shows vertical cross-sections of virtual potential temperature,  $\theta_v$ , water vapour mixing ratio and horizontal wind vectors from  $26^\circ\text{S}$  to  $17^\circ\text{S}$  on  $140^\circ\text{E}$  at 2300 EST on 09 September and 0000 EST on 10 September in the model, shortly before and after the collision of the cold front and the sea breeze. The position of the collision is about at the 240 km mark of the plot. It is difficult to identify the time and position of the collision alone from these cross-sections because there is not a strong moisture gradient along the convergence line associated with the cold front. The temperature gradient, however, gives a rough idea of the position of the cold front.

Figure 2.39 shows the relative flow,  $u - c$ , directly behind the two convergence lines (the moving cold front and the bore wave ahead of it) at a height of  $\sigma = 0.965$  at selected times. Once again  $u$  is the wind speed perpendicular to and towards the line in question

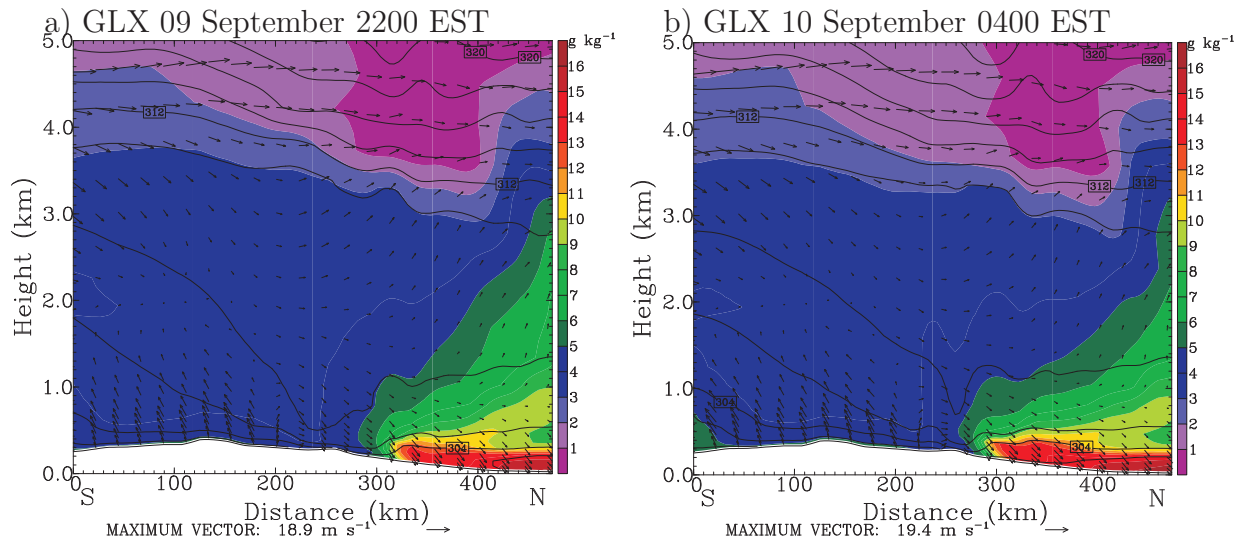


Figure 2.38: Vertical cross-section of virtual potential temperature (contour lines, interval 2 K), water vapour mixing ratio (shaded, in  $\text{g kg}^{-1}$ ) and horizontal wind vectors from the surface to 5 km at (a) 2200 EST on 09 September, and (b) 0400 EST on 10 September. The cross-sections extend from  $22^\circ\text{S}$  on to  $18^\circ\text{S}$  on  $140^\circ\text{E}$ , a distance of about 500 km. Panel (a) shows the cold front and the sea breeze south of the gulf before their collision near Mount Isa, and panel (b) after the collision.

and  $c$  is the propagation speed of that line (note that  $c$ 's are different for each line). In these calculations the orientation of the lines is  $\sim 86^\circ \pm 1^\circ$  at 2200 EST on 09 September and  $\sim 77^\circ \pm 1^\circ$  at 0200 EST on 10 September, measured anticlockwise from north. The mean propagation speed of the cold front at 2200 EST on 09 September is  $\sim 6 \pm 0.5 \text{ m s}^{-1}$ . The translation speeds of the southerly morning-glory disturbance at 0200 EST on 10 September and 0000 EST on 29 September is  $8 \pm 0.5 \text{ m s}^{-1}$ . It is seen that the relative flow on the southern side of the cold front is positive (i.e. towards the line) before the collision with the south-coast sea breeze. As noted earlier, a positive value of  $u - c$  is indicative of a gravity current, while a negative value is characteristic of a bore-like disturbance. Figure 2.39 shows that  $u - c$  becomes negative behind the northward-moving line that emerges from the collision of the northward-moving cold front and the sea breeze. At 0200 EST on 10 September, the relative flow behind the southerly morning-glory disturbance is negative and its transition to a bore wave is complete.

On this day, no dry line was observed following the convergence line, at least as far north as Karumba. An animation of water vapour mixing ratio for this event shows that the dry line did not move north of  $18^\circ\text{S}$ , which is consistent with the observations.

A vertical cross-section of virtual potential temperature,  $\theta_v$ , water vapour mixing ratio and horizontal wind vectors from ( $15.5^\circ\text{S}$ ,  $141.5^\circ\text{E}$ ) to ( $13.5^\circ\text{S}$ ,  $143^\circ\text{E}$ ) at 1800 EST and

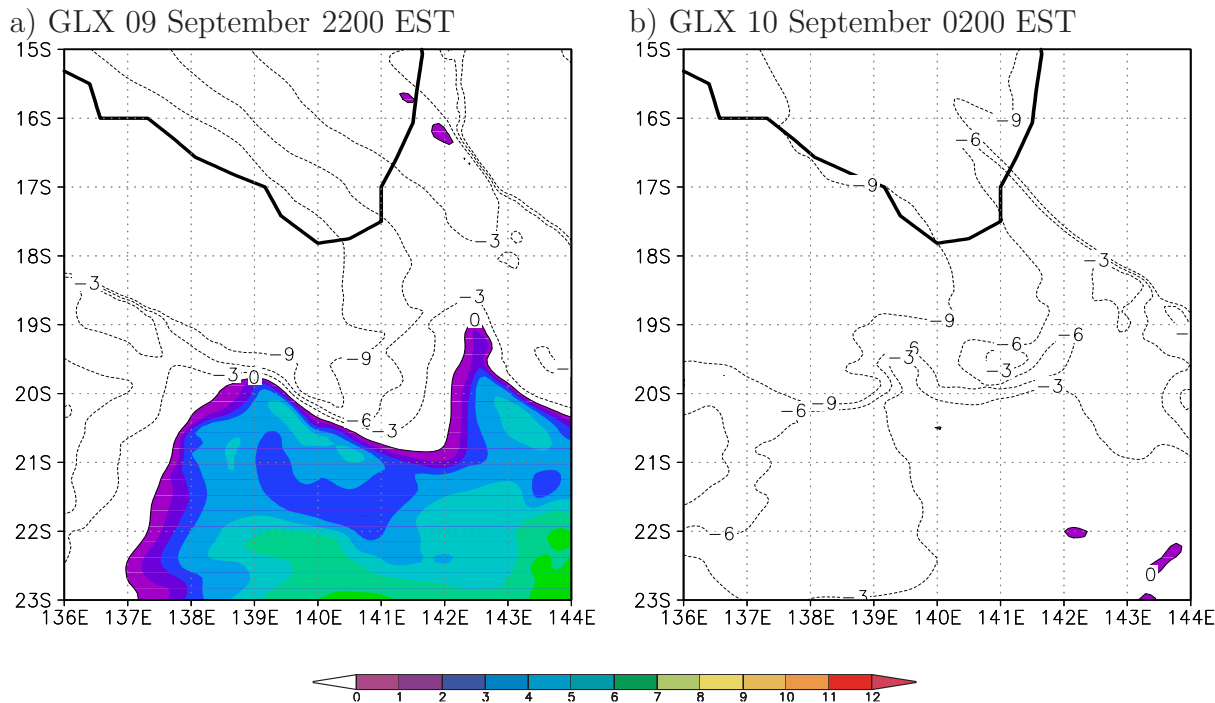


Figure 2.39: Legend as for Fig. 2.7, but for the relative flow normal to and behind the cold front at 2200 EST on 09 September (a) and behind the southerly morning glory disturbance (b) at 0200 EST on 10 September. Positive values of  $u - c$  are shaded.

2000 EST on 03 October, shortly before and shortly after the collision of the east- and west-coast sea breezes, is shown in Fig. 2.40. Inspection of the 1800 EST cross-section shows that in the present simulation, the depth of the cold air behind the west-coast sea-breeze front is shallower and the air just behind the front is a little moister than that behind the east-coast sea-breeze front. Furthermore the horizontal gradient of  $\theta_v$  near the surface is largest across the west-coast sea-breeze front, as in the other north-easterly morning-glory events discussed here.

Figure 2.41 shows the relative flow in the model,  $u - c$ , directly behind the convergence line associated with the north-easterly morning glory at a height of  $\sigma = 0.965$  at selected times. Again  $u$  is the wind speed perpendicular to and towards the line in question and  $c$  is the propagation speed of that line. In these calculations the orientation of the line is  $\sim 48^\circ \pm 1^\circ$  at 2200 EST on 09 September and  $\sim 54^\circ \pm 1^\circ$  at 0200 EST and 0600 EST on 10 September, measured anticlockwise from north. The translation speed of the morning glory at 2200 EST on 09 September and at 0200 EST and 0600 EST on 10 September is  $8 \pm 0.5 \text{ m s}^{-1}$ . It is seen that the relative flow north-eastwards of the morning-glory disturbance is positive (gravity-current like) shortly after the collision. Figure 2.41b shows that the relative flow has declined two hours later and becomes negative (bore-like) at 0600 EST on 10 September, as shown in Fig. 2.41c. This transition to a bore is very similar to

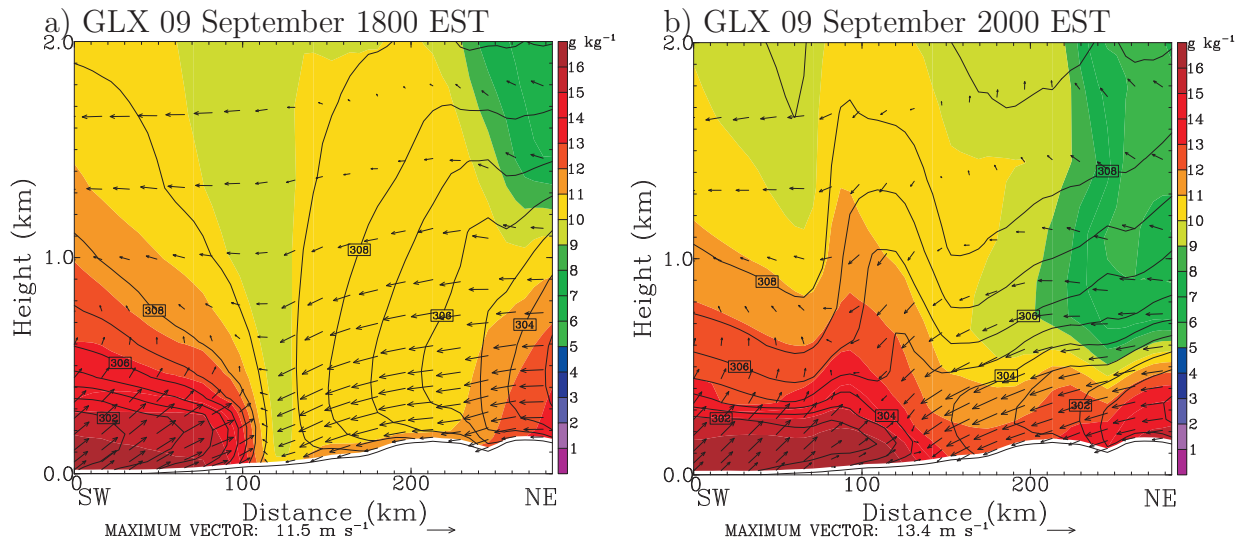


Figure 2.40: Vertical cross-section of virtual potential temperature (contour lines, interval 1 K), water vapour mixing ratio (shaded, in  $\text{g kg}^{-1}$ ) and horizontal wind vectors from the surface to 2 km at (a) 1800 EST and (b) 2000 EST on 09 September. The cross-sections extend from  $15.5^\circ\text{S}$  on  $141.5^\circ\text{E}$  to  $13.5^\circ\text{S}$  on  $143^\circ\text{E}$ , a distance of about 300 km. In (a) the two sea breezes are about to collide and (b) is just after the collision.

the cases discussed earlier in this chapter.

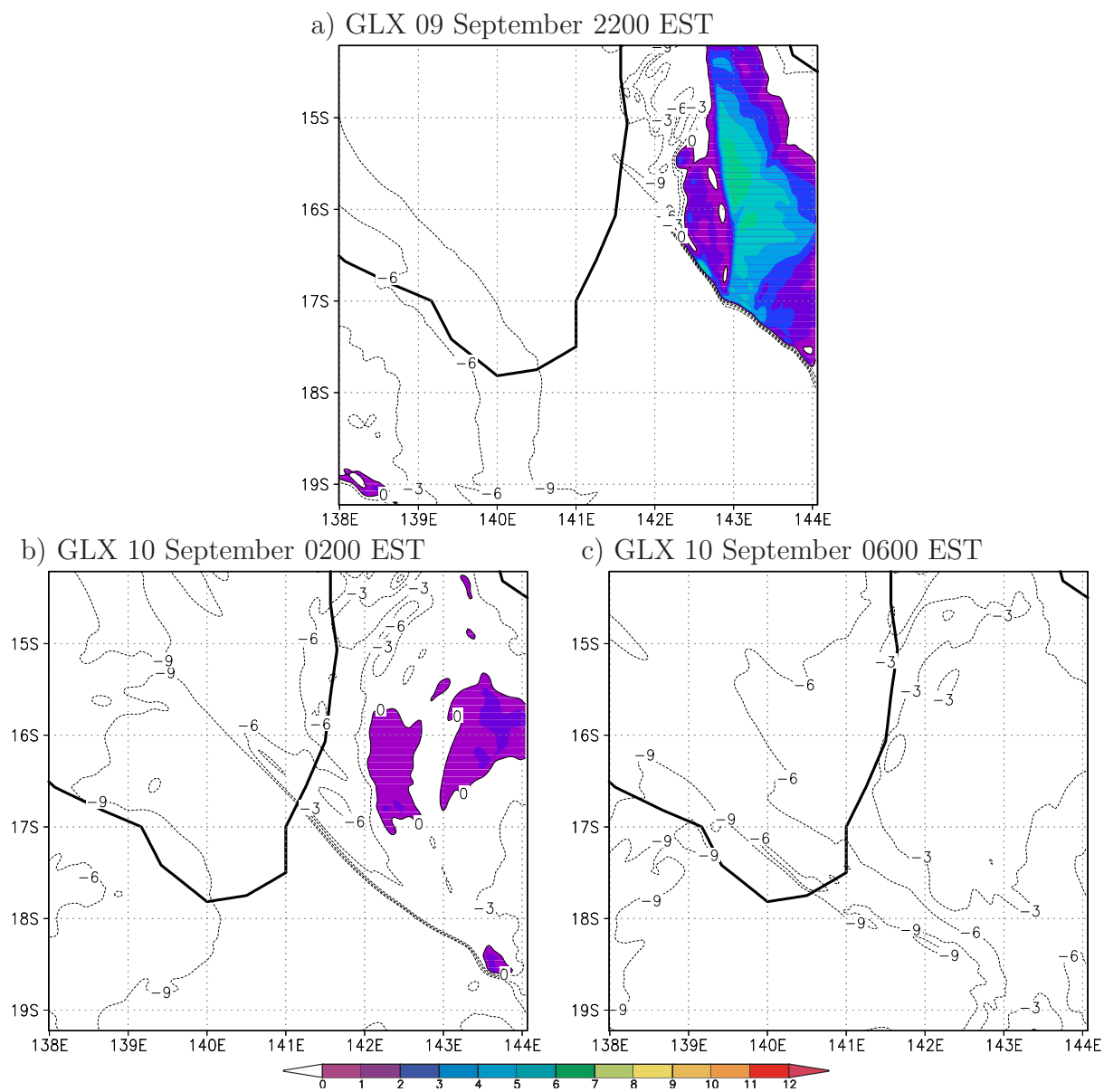


Figure 2.41: Legend as for Fig. 2.7, but for the relative flow normal to and behind the north-easterly morning glory disturbance on 09 and 10 September. Positive values of  $u - c$  ( $\text{m s}^{-1}$ ) are shaded.

## 2.7 29-30 September

The synoptic situation in the southern gulf region at 1000 EST on 29 September was dominated by a trough line and a cold front. This cold front was generated by convergence into the trough and collided with the sea breeze in the evening of 28 September (see the section of that event). The position of the trough line is indicated in the MSLP analysis shown in Fig. 2.42a. On 30 September neither morning glories or an NACL were observed over the gulf. Figure 2.42b shows a visible satellite image of the gulf region at 0532 EST on 30 September. The cloud band stretching from east of the northern Cape York Peninsula over the northern Gulf of Carpentaria was present at the position shown in the image also on the previous days and has its origin most probably in convective processes east and north-east of the peninsula, over the Coral Sea. The spotted area of convective cloud north of a line approximately from  $141.5^{\circ}$  E  $15.5^{\circ}$  S to  $145^{\circ}$  E  $16.5^{\circ}$  S over the peninsula marks the border of dry continental air associated with the dry-line to the south and moist maritime air.

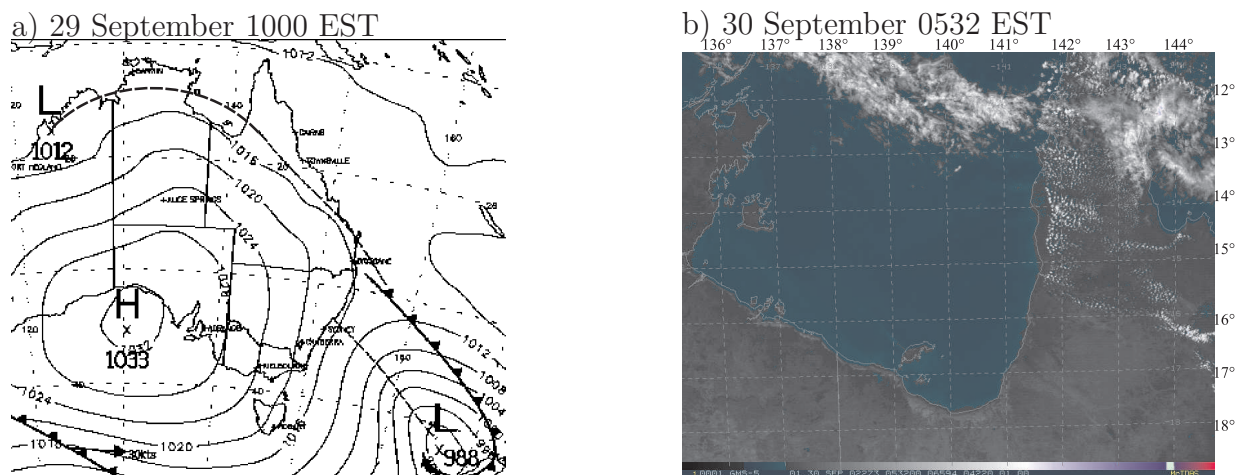


Figure 2.42: (a) MSLP analysis at 1000 EST on 29 September adapted from the Bureau of Meteorology. The trough line in the Gulf of Carpentaria region is indicated by a dashed line. (b) GMS visible satellite image for the Gulf of Carpentaria area at 0532 EST on 30 September.

This simulation was initialized at 1000 EST on 29 September. Figure 2.43 shows a series of predicted low-level divergence fields. By 1900 EST on 29 September the collision of the east-coast and the west-coast sea breezes has commenced north of  $15^{\circ}$  S. The position and time of this collision is usual for the north-easterly events discussed in this chapter. South of  $16.5^{\circ}$  S, strong southerlies have inhibited the formation of a sea breeze.

By 2200 EST a north-easterly disturbance has developed after the collision of the two sea breezes. The position of the disturbance is consistent with the AWS station measurements from Highbury (at 2130 EST) and Dunbar (at 2230 EST) on Cape York Peninsula. Such a disturbance is the usual precursor to a north-easterly morning-glory convergence line.

By 0100 EST on 30 September, the strong southerlies have turned to south-easterlies. The strong winds parallel to the disturbance have inhibited its passage beyond a line from  $140^{\circ}$  E,  $14^{\circ}$  S to  $144^{\circ}$  E,  $18^{\circ}$  S, again in accordance with the observations.

Figure 2.43d shows the situation at 0500 EST, about half an hour earlier than the time of the satellite image in Fig. 2.42a. There is a line of moderate convergence which separates the moist air to the north and the dry air to the south of it. There is also convergence under some parts of the cloud band in the northern gulf, but it is not possible to determine its origin. The divergence plots at earlier times suggest that there was no NACL on this day.

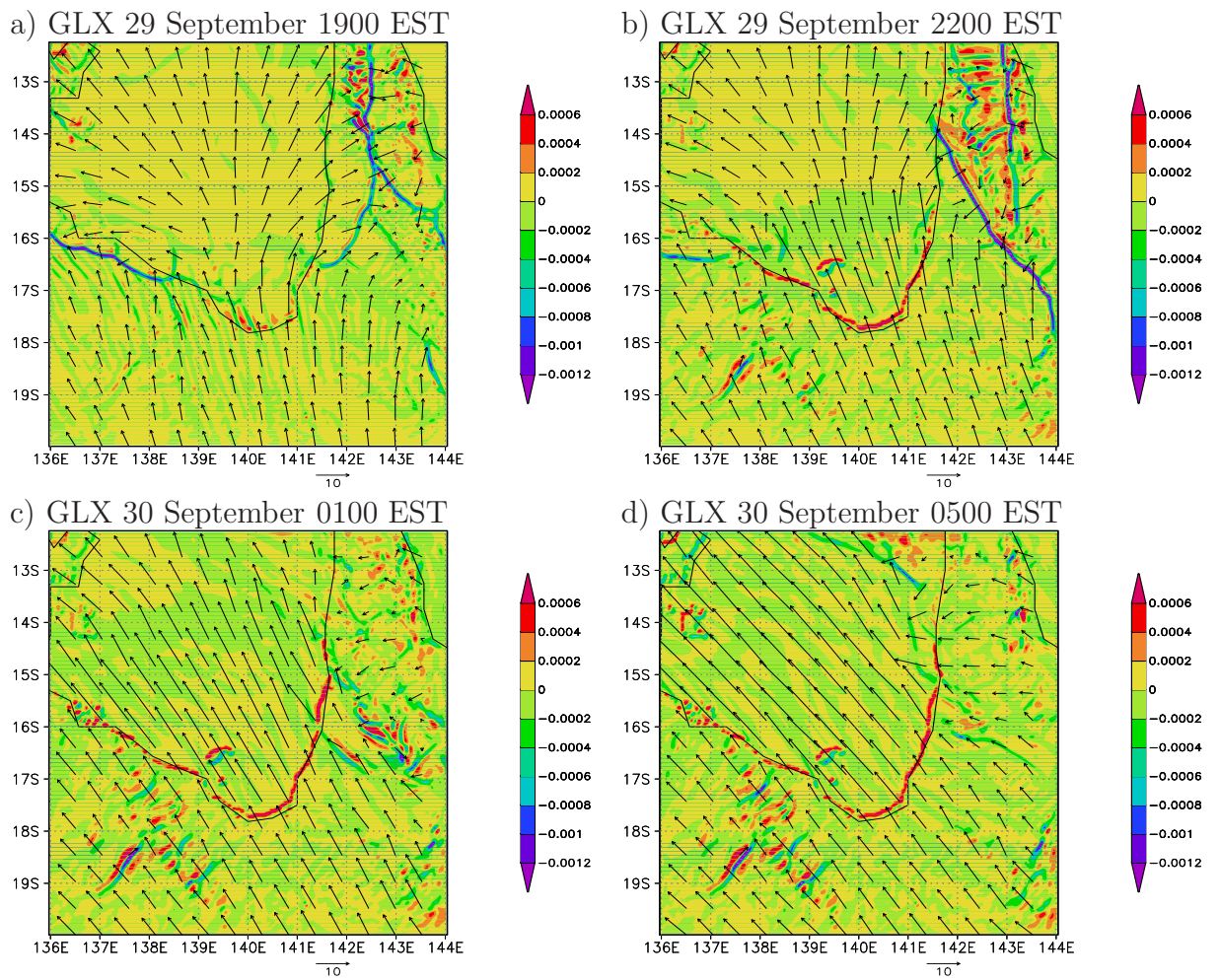


Figure 2.43: Low-level wind vectors (scale  $10 \text{ m s}^{-1}$  below each panel) and divergence (shaded, unit  $\text{s}^{-1}$ ) in the GLX calculation at (a) 1900 EST and (b) 2200 EST on 29 September and (c) 0100 EST and (d) 0500 EST on 30 September. The plots are at  $\sigma = 0.9975$ .

A vertical cross-section of virtual potential temperature,  $\theta_v$ , water vapour mixing ratio and horizontal wind vectors from 141.5°E to 143°E on 14°S at 1800 EST and 1900 EST on 29 September, shortly before and shortly after the collision of the two sea breezes, is shown in Fig. 2.44. Inspection of the 1800 EST cross-section shows that, as in the previous simulations, the depth of the cold air behind the west-coast sea-breeze front is shallower and the air just behind the front is a little moister than that behind the east-coast sea-breeze front. Furthermore the horizontal gradient of  $\theta_v$  near the surface is largest across the west-coast sea-breeze front, suggesting that the east-coast sea breeze will rise above the west-coast sea breeze at collision, again as in the previous cases.

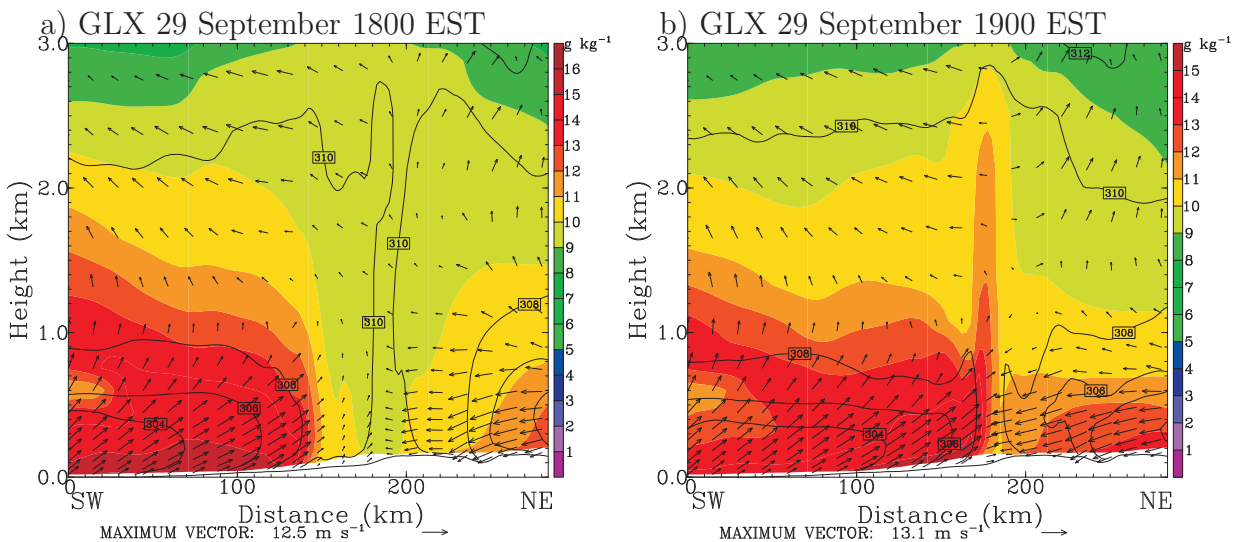


Figure 2.44: Vertical cross-section of virtual potential temperature (contour lines, interval 2 K), water vapour mixing ratio (shaded, in  $\text{g kg}^{-1}$ ) and horizontal wind vectors from the surface to 3 km at (a) 1800 EST, and (b) 1900 EST on 29 September. The cross-sections extend from 141.5°E to 143°E on 14°S. In (a) the two sea breezes are about to collide and (b) is just after the collision.

Figure 2.45 shows the relative flow,  $u - c$ , directly behind the north-easterly morning-glory at a height of  $\sigma = 0.965$  and at selected times, where  $u$  is the wind speed perpendicular to and towards the line in question and  $c$  is the propagation speed of that line. In these calculations the morning-glory line has an orientation of  $\sim 41^\circ \pm 1^\circ$  at 1800 EST and  $\sim 40^\circ \pm 1^\circ$  at 2200 EST on 29 September and  $\sim 48^\circ \pm 1^\circ$  0200 EST on 30 September. The translation speeds of this line at these times are  $5.6 \pm 0.5 \text{ m s}^{-1}$ ,  $9.2 \pm 0.5 \text{ m s}^{-1}$  and  $13 \pm 0.5 \text{ m s}^{-1}$ , respectively. It is seen that the relative flow behind, i.e. to the north-east of the east-coast sea breeze is positive (i.e. towards the line and therefore, as noted earlier gravity-current like) before the collision of the two sea breezes. As noted earlier, a positive value of  $u - c$  is indicative of a gravity current, while a negative value is characteristic of

a bore-like disturbance. Note that  $u - c$  is negative, i.e. bore-like, behind the parts of the disturbance where the collision of the two sea breezes occurred. After about 0200 EST, the relative flow behind the disturbance is negative and its transition to a bore wave is complete.

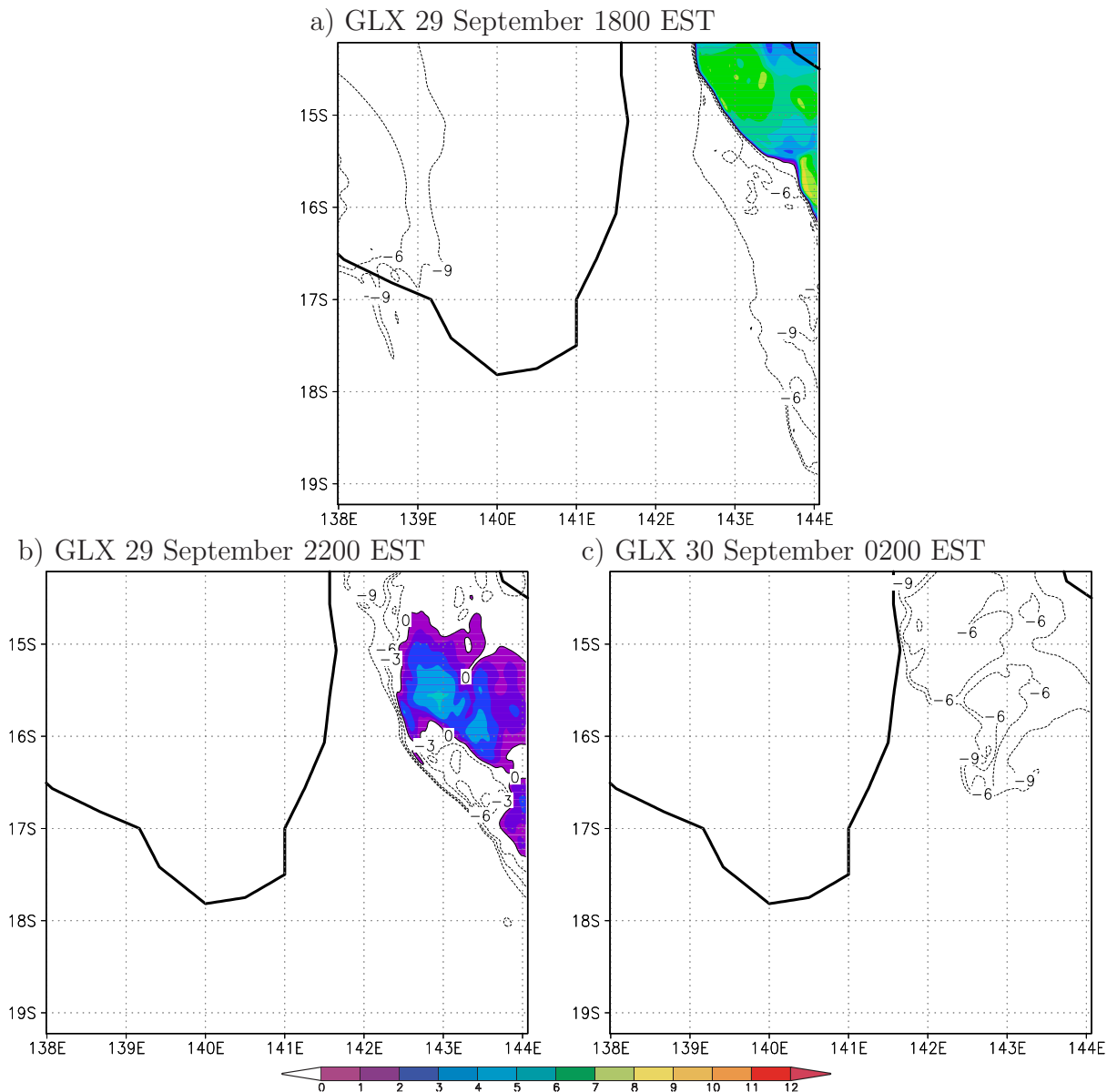


Figure 2.45: Legend as for Fig. 2.7, but for the relative flow normal to and behind the north-easterly morning-glory disturbance on 29 and 30 September. Positive values of  $u - c$  are shaded.

The surface pressure correlation coefficient for this simulation is  $r = 0.96$ . The sim-

ulation of this event shows that the model is able to reproduce also events in which no morning glory or NACL occurred. The course of events in this case suggests that strong southerlys play a significant role in inhibiting the north-easterly disturbances to propagate far into the southern gulf region. This result is consistent with findings of a study by Smith and Noonan (1998). The presence of a trough line and the generation of a cold front at a position allowing a collision with the south-coast sea breeze appears to be crucial for the generation of a southerly disturbance. An analysis of the first event in the Central Australian Fronts Experiment (CAFE) in 1991 by Smith *et al.* (1995) showed that in reality, this might not be generally the case. Following their analysis of the case, a bore-like disturbance formed far south of the Gulf of Carpentaria, before the collision with a sea breeze. Preliminary calculations for this event show that the surface-based stable layer did significantly deepen ahead of the disturbance, but the reasons for this deepening are still under investigation. The results of this study, when completed, will be submitted for publication in due course.

## 2.8 Summary

With a horizontal resolution of 3 km in the finest domain and a commensurate vertical resolution, MM5 in the present configuration has considerable skill in predicting the convergence lines observed in the first four GLEX events that I investigated. The higher resolution and nonhydrostatic formulation allow a more accurate depiction of the lines than the operational mesoLAPS forecasts. Unlike mesoLAPS, MM5 is able to distinguish clearly between the convergence lines corresponding to the north-easterly morning glory and NAEL, showing that the former develops out of the east-coast sea-breeze front on Cape York Peninsula south of about 14°S, while the latter forms from the same sea-breeze front to the north of this latitude. Calculations of the low-level flow towards each of these lines show that both have the character of a gravity current (with the relative flow behind the line and normal to it being positive) during the afternoon and evening, but the morning-glory convergence line progressively acquires the character of a bore as the region of positive relative flow behind it declines overnight. Eventually the relative flow behind the line becomes negative, completing the transition to a bore-like flow. In contrast, the line marking the NAEL retains a gravity-current-like structure. Also in contrast to mesoLAPS, MM5 captured the generation of a bore-like disturbance moving ahead of and separating from the airmass change in the three major southerly disturbances (28/29 September, 08/09 October and 09/10 September).

Despite its accuracy in representing the north-easterly disturbances on 04 October, the model fails to capture a disturbance corresponding to the observed southerly morning glory on this day, but like mesoLAPS, it does predict a northward-moving convergence line about 100 km to the south of where the morning glory has formed. This line does not reach the southern gulf coast before the recommencement of daytime mixing, which would have removed the low-level stable layer required for propagation of the shallow disturbance. The model also fails to produce a south-easterly disturbance on 09 October. These failures probably reside in an inaccurate location of the convergence line over the data-sparse region south of the gulf in the initial analysis. An article by Smith *et al.* (1986) illustrates the difficulties of carrying out a detailed MSLP analysis in this area. These convergence lines form along the northern perimeter of a ridge from an anticyclone as the latter moves eastwards across the continent.

The calculations support a recently proposed conceptual model for the generation of southerly morning glories, in which ageostrophic low-level convergence leads to the formation of a shallow northward-moving cold front in the evening on the southern side of the inland trough. This front collides with an even shallower sea breeze flow from the southern gulf coast and leads to the formation of a bore-like disturbance that moves northwards on the stable layer provided by the sea breeze air. Vertical cross-sections of moisture on days with southerly disturbances show a strong meridional gradient in moisture on the northern side of the inland trough. This moisture gradient corresponds to the dry line, which marks

the maximum inland penetration of the sea breeze south of the gulf.

The calculations for the 29/30 September suggest that the collision of the west- and east-coast sea-breezes over Cape York Peninsula generally produces a bore wave and that southerly winds opposing the direction in which this disturbance propagates have a disruptive effect on the line. The simulation suggests also that a trough line south of the southern gulf coast, and the generation of a cold front at a position which allows a collision with the southerly sea breeze, plays an essential role in generating a southerly morning glory.

While the dry line in the 28/29 September case travelled north of the the southern gulf coast it did not reach the south-coast AWSs on 10 September and on 09 October. In the 03/04 October case, there was no dry line at all in observations or model, suggesting that a dry line is not an important feature of the generation of southerly morning glories in general.

Towards the end of this case study, personal communication with scientists at the Australian Bureau of Meteorology Research Centre in Melbourne and a closer look into model details revealed several possible explanations, other than its hydrostatic setup, for the rather modest skill of mesoLAPS compared with the MM5 calculations presented here. As noted earlier, the radiation scheme is invoked only every 3 h (Dr. Bill Bourke, personal communication) which may delay the effective time of sunrise in the model. An other important point is that the coefficients for the horizontal numerical diffusion have not been modified from a much coarser setup (Dr. Gary Dietachmayer, personal communication). These high diffusion coefficients may smear out an otherwise well-defined convergence line. Last but not least, a closer look into the surface fluxes showed that the land-sea mask is offset by about 50 km into the real ocean. This arrangement has been made for numerical reasons in earlier mesoLAPS configurations (Dr. Noel Davidson, personal communication), but has become obsolete in the meantime. This offset accounts for another significant delay of the collision times both of the two sea breezes over Cape York Peninsula and of the south-coast sea breeze and the cold front over the region south of the gulf coast. Simulations with corrections of all these disturbing effects have not been made by this time.

## Chapter 3

# Sensitivity to boundary layer schemes

### 3.1 Model configuration and experiments

Stull (1988) defines the planetary boundary layer as that part of the troposphere that is directly influenced by the presence of the earth's surface and responds to surface forcing with a timescale of about an hour or less. The bottom 3 km of the troposphere generally includes the planetary boundary-layer (PBL). In the configuration described in Chapter 1, the thickness of the model layers in the lowest 3 km varies from  $\sim 40$  m to  $\sim 400$  m, increasing with height. The most energetic boundary layer eddies, being tens of metres to 1-2 km high, are not sufficiently resolved by this resolution (a typical resolution for simulations with this type of model). In order to compensate this lack of vertical resolution, a parameterisation of the PBL has to be applied. For different purposes (differing in the resolutions of the PBL, the computational needs, the assumptions and approximations), several different parameterisations for the PBL are available in MM5. The aim of the study described in this chapter is to find the most suitable parameterisation for simulating the convergence lines in the Gulf of Carpentaria region. The choice of parameterisation may have a significant impact on the model results since the collision of two air masses leading to the generation of the morning-glory lines occurs in the boundary layer. This study was performed before the calculations described in previous chapters and the optimum scheme was applied in these.

The 08/09 October event is selected for this study. With this choice it is possible to minimise the number of experiments while being able to assess the impact of the choice of PBL parameterisation on as many cloud-line phenomena as possible. On 09 October, all types of morning glories and an NACL occurred (see Chapter 2.3 for details). The satellite image from that event is shown again in Fig. 3.1.

In contrast to the configuration described in Chapter 1, the simulations described here are carried out without a representation of moist vertical diffusion and a soil-moisture

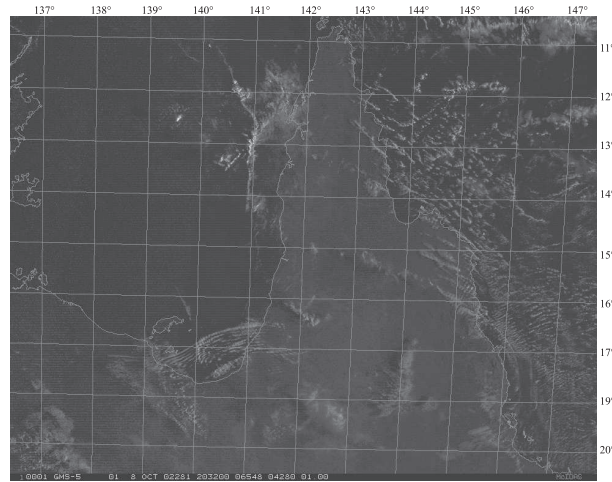


Figure 3.1: Satellite infrared picture of the cloud lines on 09 October at 0632 EST

scheme, since only a few boundary-layer parameterisations in MM5 described here support both these schemes. The removal of the two schemes was necessary in order to isolate the effects resulting solely from the choice of boundary-layer parameterisation. However, the consequences of these removals are described briefly.

Figure 3.1 shows the low-level divergence in four different model configurations at 0400 EST on 09 October. The top left panel shows results from the GLX run described in the previous chapter and the bottom right panel shows results for an identical calculation, but with the soil moisture and moist vertical diffusion schemes excluded. Panel (b) shows model results without the moist vertical diffusion and (c) without the bucket soil moisture scheme. Switching the bucket soil scheme off keeps the soil moisture constant. Since the soil moisture was already set to very low values in the control run the variation in soil moisture is only small (see next chapter for details), and a comparison of the low-level wind divergence field after 20 h of integration time in the top and bottom panels shows hardly any difference at all. Only the MRF and Blackadar PBL schemes have the moist vertical diffusion option. The moist vertical diffusion scheme allows diffusion in cloudy air to mix toward a moist adiabat by basing its mixing on moist stability instead of the dry stability. It can mix cloudy air upwards into clear air in addition to just internally in cloudy layers. The deactivation of this option reduces the intensity of the low-level convergence line corresponding to the southerly morning glory. Therefore, the moist vertical diffusion must play a role in strengthening the intensity of the southerly convergence line. The intensity of the north-easterly morning-glory convergence line seems to be less affected by the deactivation of the moist vertical diffusion option (compare left and right panels).

In the following section, I will describe briefly two land-surface schemes which necessarily interact with the PBL parameterisations. After that, I will give an overview over the

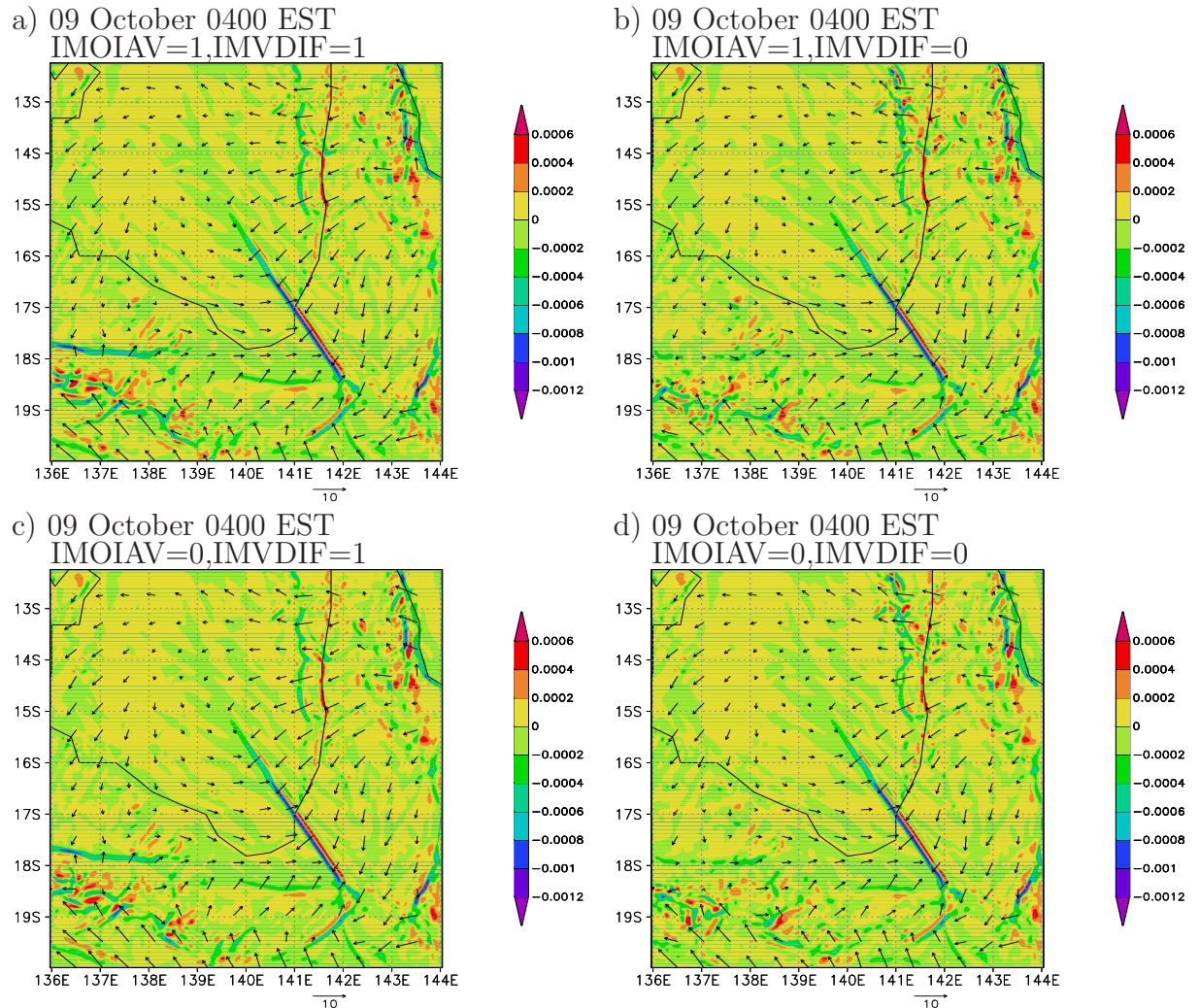


Figure 3.2: Low-level wind vectors (scale  $10 \text{ m s}^{-1}$  below each panel) and divergence (shaded, unit  $\text{s}^{-1}$ ) at  $\sigma = 0.9975$  at 0400 EST on 09 October. In each panel, IMOIAV=1 means the bucket soil scheme is active and IMVDIF=1 means the moist vertical diffusion is active.

boundary layer schemes in MM5, accompanied by a discussion of model results achieved with these parameterisations. In the last section of this chapter I will summarise the results and discuss the choice of parameterisation for further experiments.

## 3.2 Land-surface schemes in MM5

The different PBL parameterisations require certain surface schemes of which are four

available in MM5:

The force/restore (Blackadar) scheme treats the soil as a single slab which is assumed to span the depth over which there is a significant diurnal temperature variation (approximately 10-20 cm). The slab temperature is based on the energy balance at the surface and the substrate-temperature is fixed.

The five-layer soil model predicts the temperature in layers of 1,2,4,8 and 16 cm depth with fixed substrate temperature below applying a vertical diffusion equation. The thermal inertia is derived in a similar way to the force/restore scheme except the diurnal temperature variation is computed in the different layers separately, allowing for a more rapid response of the surface temperature. The five-layer soil model is computationally more stable and allows for a larger timestep than the force/restore scheme.

Both the force/restore and the five-layer soil model use a "look-up"-table for the surface characteristics like albedo, roughness, emissivity and thermal inertia. These surface characteristics are held constant during the model integration.

The NOAH- and the Pleim-Xiu land-surface model are more sophisticated, but are not included in this study for technical reasons. The NOAH land-surface model works only with the MRF- and Eta PBL scheme and requires several additional fields for initialisation. These fields are not generally available from the ECMWF. The Pleim-Xiu land-surface model works only with the Pleim-Xiu PBL parameterisation, which is not available in a massive-parallel version. The memory requirement of a model run in this configuration is too large for the single-processor version of MM5. Apart from these technical reasons, the main focus in this chapter is on the PBL schemes and not on land-surface schemes.

## 3.3 Boundary layer schemes in MM5

### 3.3.1 Explicit

When no PBL parameterisation is implemented, the force/restore land-surface scheme is used and all boundary-layer physics has to be resolved explicitly by the model equations applied in the relatively coarse vertical grid. Figure 3.3 vividly exposes the consequences of a configuration without a boundary-layer parameterisation. The winds are unrealistically strong. There are two distinct convergence lines over the gulf. The north-western, Y-shaped feature of the line matches the north-easterly morning glory at its southernmost end quite well, while its part north of about 16° S was not observed. The easterly convergence line (marked A) presumably corresponds to the NACL, except it is about 100 km too far west. The line marked B corresponds to the southerly morning glory and the line

marked C corresponds to convergence at the northern edge of the region of southerly ageostrophic flow towards the trough. The separation of these two convergence lines is captured surprisingly well by the model, though the positions are about 200 km too far to the south. A convergence line corresponding to a south-easterly morning glory is not captured by the model. The mean sea-level pressure (MSLP) correlation coefficient (see Chapter 2 for details) for this model run is  $r = 0.60$ , reflecting the deficiencies of this particular model configuration.

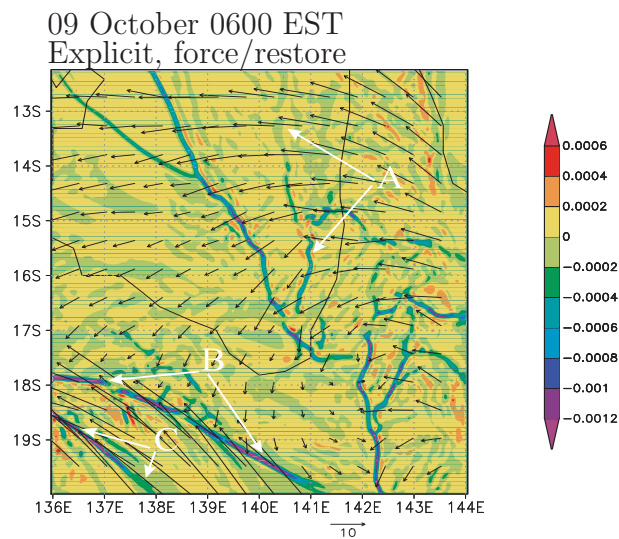


Figure 3.3: Low-level wind vectors (scale  $10 \text{ m s}^{-1}$  below panel) and divergence (shaded, unit  $\text{s}^{-1}$ ) at  $\sigma = 0.9975$  at 0600 EST on 09 October.

### 3.3.2 Blackadar

The Blackadar PBL scheme (Blackadar 1976) was first introduced as a parameterisation scheme for the nocturnal boundary layer. The version used here was extended by Blackadar (1978, 1979) and Zhang and Anthes (1982) to account also for the daytime PBL.

The magnitude of  $|z_h/L|$  and the vertical temperature gradient in the lowest model layer determine which of the two modules (one for the day-time convective and one for the night-time stable PBL stability states) is used. Here,  $z_h$  is the height of the mixed layer and  $L$  is the Monin-Obukhov length and the vertical temperature gradient in the lowest model layer is represented by the bulk Richardson number  $Ri_b$ . The height of the mixed layer is defined as the height at which  $Ri_b$ , the eddy exchange coefficient  $K$ , and the fluxes of heat, moisture and momentum are zero. In the module for the nocturnal PBL, the atmospheric stratification is assumed to be stable, or at most slightly unstable, and a first-order closure scheme is used. To account for the largest gradients which generally occur in the lowest layer, a surface layer of 10 m depth is used based on Monin-Obukhov similarity theory. The module for the nocturnal PBL is subdivided into three PBL stability states: The nighttime stable state ( $Ri_b \geq 0.2$ , state=1) in which all fluxes and scaling parameters at the surface are set equal to zero, the damped mechanical turbulent state at the surface ( $0 < Ri_b < 0.2$ , state=2) in which the scaling parameters are determined by  $Ri_b$  and  $L$  and the forced convection state ( $Ri_b \leq 0 \wedge |z_h/L| \leq 1.5$ , state=3) in which the scaling parameters are determined by the Richardson number  $Ri$  only. In all three stability states local  $K$ -theory is used above the surface ( $K$  is determined by the local Richardson number  $Ri$  in contrast to TKE-prediction used in the Mellor-Yamada-based schemes which are described in the next subsection).

The module for the daytime PBL (active when  $Ri_b \leq 0 \wedge |z_h/L| \geq 1.5$ , state=4) allows for free-convection and discrete matrix forms of nonlocal theory (the vertical transfer of momentum, heat and moisture is not determined by local gradient, but by the thermal structure of the whole mixed layer) are used to parameterise convective circulations. In this study, the Blackadar scheme is the only scheme which applies transilient mixing in one of the PBL stability states, i. e. it allows mixing between non-adjacent vertical layers.

The Blackadar scheme is the only PBL parameterisation in MM5 which works with both the force/restore- and the 5-layer surface scheme. Figures 3.4 and 3.5 show model results with the force/restore- and with the 5-layer surface scheme, respectively. Panels (a) show the low-level divergence field and wind vectors, panels (b) show the predicted boundary layer height and panels (c) show the PBL stability states as determined by the PBL parameterisation. A comparison of both figures indicates that there is virtually no difference with both surface schemes after 16 h of integration. The similarity of these two model runs is reflected in the MSLP correlation coefficient being  $r = 0.93$  in both runs. This relatively good value agrees well with the low-level divergence field. The south-east to

north-west oriented line corresponds to the north-easterly morning glory and the position agrees with the observations within a few km accuracy. The convergence line corresponding to the southerly morning glory has only a weak signature at this time, but its position is clear from the animated fields and is marked by enhanced convergence at a point on the north-easterly convergence line. This position is close to the observed position. The convergence line over the gulf, which is almost parallel to the western coastline of the peninsula, corresponds to the NACL. In comparison with the satellite image in Fig. 3.1 its position is also well captured in these two model runs, but a south-easterly morning glory is not captured.

Panels (a) show that the convergence of the line corresponding to the north-easterly morning glory is stronger over land than it is over the sea. Also, the line is displaced about 25 km north-eastwards on its seaward end compared with its end over land. The region of transition to the retarded section of the line is just over the coast, indicating a different vertical structure of the PBL over land than over sea areas. Panels (b) show that the boundary-layer height is zero over land and in small regions over the gulf. A closer look into the code for the Blackadar scheme<sup>1</sup> shows that the boundary-layer height is computed only in stability states three and four (forced convection and daytime free convection). These states prevail over the gulf during night-time since the air is cooler than the sea-surface at these times and  $Ri_b$  becomes negative. On the other hand, states one and two prevail over land. This difference in the stability states leads to a different treatment of the PBL over land compared with that over sea during the night. It should be pointed out that the PBL parameterisation might not be realistic at these small scales, a statement that is valid for all the boundary-layer schemes described here. Nevertheless, panels (c) show that the PBL heights are elevated along the leading edges of the morning-glory lines in the model, reflecting the increased turbulence at these positions. The PBL height is higher along the position of the NACL convergence line and lower in front (to the west) of the line, reflecting the character of a gravity current.

---

<sup>1</sup>MM5/physics/pbl\_sfc/hirpbl.F

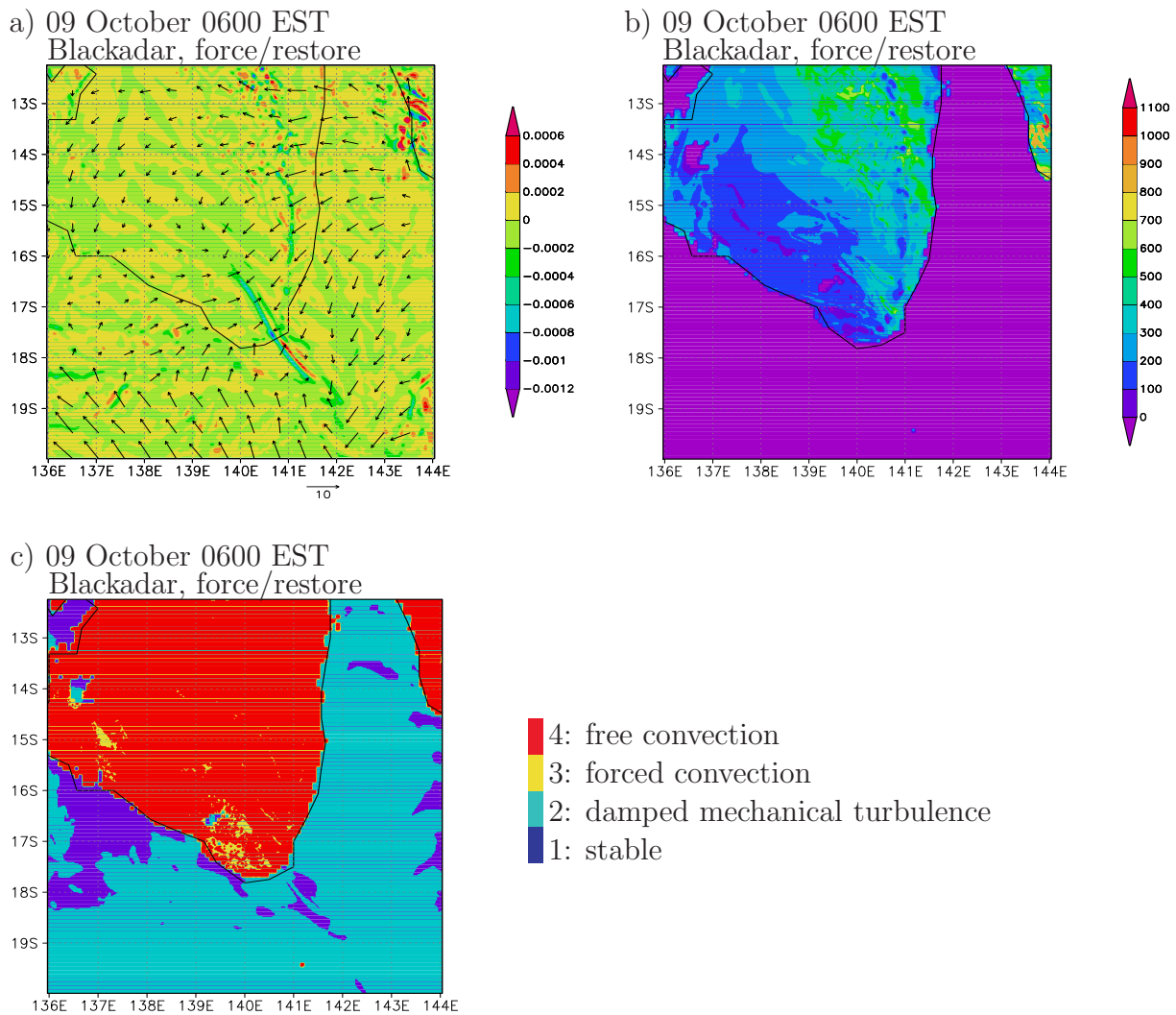


Figure 3.4: a) Low-level wind vectors (scale  $10 \text{ m s}^{-1}$  below panel) and divergence (shaded, unit  $\text{s}^{-1}$ ) at  $\sigma = 0.9975$ , b) Boundary layer height (in  $m$ ), and c) PBL stability states at 0600 EST on 09 October.

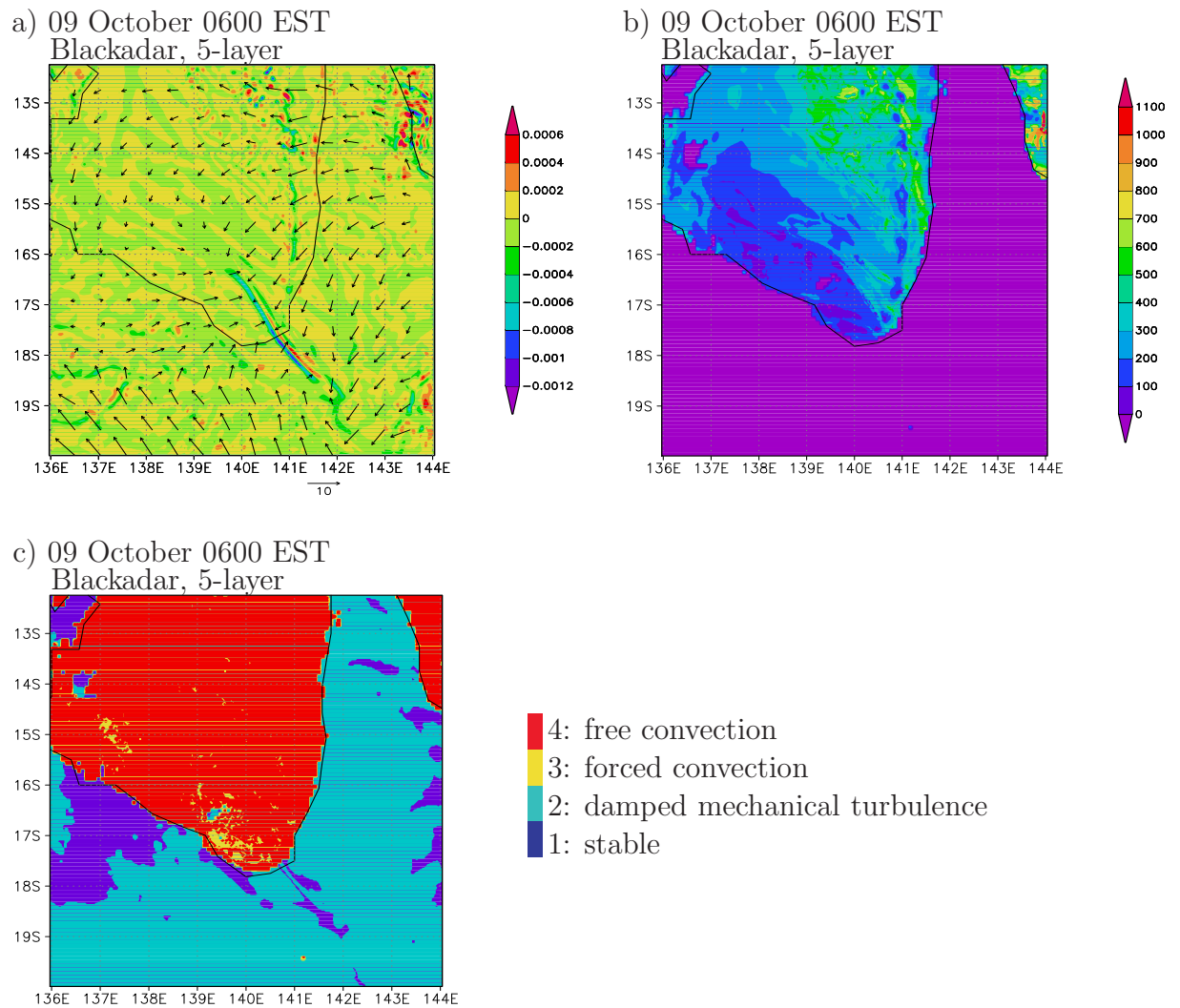


Figure 3.5: a) Low-level wind vectors (scale  $10 \text{ m s}^{-1}$  below panel) and divergence (shaded, unit  $\text{s}^{-1}$ ) at  $\sigma = 0.9975$ , b) Boundary layer height (in  $m$ ), and c) PBL stability states at 0600 EST on 09 October.

### 3.3.3 Mellor-Yamada-based schemes

All three Mellor-Yamada-based boundary-layer schemes described here use a one-and-a-half-order closure, which refers to level 2.5 in the Mellor-Yamada nomenclature. A comprehensive summary of different closures is given by Stull (1988) and Mellor and Yamada presented their nomenclature in 1974. In a one-and-a-half-order closure the eddy exchange coefficient,  $K_a$ , of an adiabatically conserved quantity,  $a$ , is specified by the turbulent kinetic energy (TKE). This kind of scheme is often referred to as a "TKE scheme".

#### Burk-Thompson

The Burk-Thompson boundary layer scheme was originally designed for the marine boundary layer (Burk and Thompson, 1982). While Burk and Thompson introduced both level 2.5 and 3.0 schemes, only the level 2.5 version is implemented in MM5. The early versions of the scheme, which were originally implemented in the US-Navy's NORAPS (Navy Operational Regional Atmospheric Prediction System), existed in a vertically nested version also. This version is not implemented in MM5. The Burk-Thompson-scheme has its own force-restore ground temperature scheme and does not interface with any other MM5 soil models or land use schemes. Neither horizontal advection or diffusion nor vertical advection of TKE are included in this scheme.

Figure 3.6 shows the low-level divergence field and wind vectors at 0600 EST on 09 October. The convergence line corresponding to the north-easterly morning glory in the south-eastern corner of the gulf is close to its position in the satellite picture in Fig. 3.1. As in the Blackadar scheme, the part of the convergence line over sea is shifted backwards (north-eastwards) in relation to the landward end of the line by a few kilometres, but unlike in the Blackadar case, the line is broken over the coast. This break marks the position of the southerly morning-glory convergence line, which is only relatively weak in intensity. The Burk-Thompson scheme does not apply different PBL stability states and the boundary-layer height is also not computed. Neither the literature describing the scheme nor the code of the Burk-Thompson scheme indicate a different treatment of the land- and sea-surface. Thus, the reason for the retardation of the north-easterly convergence line over the sea is assumed to be the impact of the different surface parameters. The model produces a broken line corresponding to the NACL in the north-eastern gulf. The position of this line is in approximately the right position. The trailing edge of the trough line is marked by a convergence line between  $18^\circ$  S and  $19^\circ$  S, a position which is confirmed by surface observations. A south-easterly morning glory is not captured. The MSLP correlation coefficient for this run is  $r = 0.86$ .

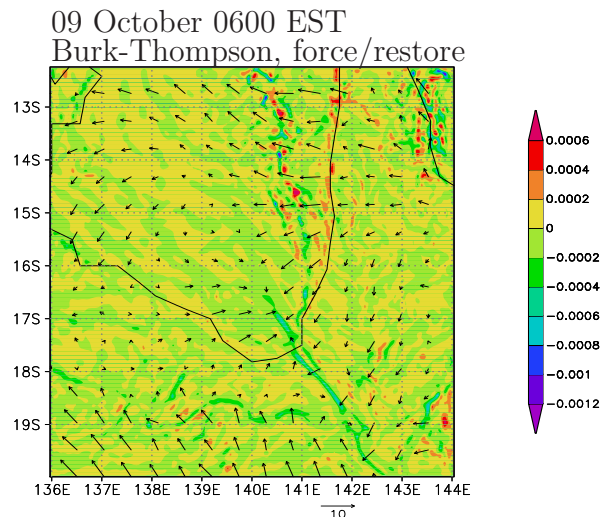


Figure 3.6: Low-level wind vectors (scale  $10 \text{ m s}^{-1}$  below panel) and divergence (shaded, unit  $\text{s}^{-1}$ ) at  $\sigma = 0.9975$  at 0600 EST on 09 October.

### Eta

The Eta-scheme was originally implemented by Janjić (1990, 1994) in the U. S. National Centers for Environmental Prediction (NCEP) Eta (step-mountain) model. It is based on the level 2.5 Mellor-Yamada scheme above the surface layer. The surface layer is treated differently over land than over ocean. As in the Burk-Thompson scheme, horizontal advection and diffusion and vertical advection of TKE are ignored. The Eta-scheme interfaces with the MM5 5-layer soil model, which is necessary because of the long time step of the Eta-scheme.

Figure 3.7a shows the low-level wind-divergence field and wind vectors at 0600 EST on 09 October. As with the Burk-Thompson scheme, NACL, north-easterly convergence line and the line of convergence at the northern edge of the southerly ageostrophic flow towards the trough are captured by the model, while a convergence line corresponding to the southerly morning glory is not so well captured and a south-easterly morning-glory line is not captured at all. The most striking difference to the results with the Burk-Thompson scheme is the coherence of the convergence line corresponding to the north-easterly morning glory at the coast line. This line is delayed by about an hour compared to the observations, which is the largest delay of all schemes tested here. The formulations of the Burk-Thompson and of the Eta scheme are quite similar and the main differences affect the surface layer. It is therefore not surprising that both schemes give similar results and that the MSLP correlation coefficient for the Eta-scheme,  $r = 0.85$ , is close to that for the Burk-Thompson scheme.

In contrast to the Burk-Thompson scheme, PBL stability condition and -height are calculated in the Eta-scheme, but only to interface with the four-dimensional data assimilation (FDDA) option, which is not applied here. Though having no effect on the model results, the occurrence of negative values for the boundary-layer height at many positions is a concern (see Fig. 3.7b). Figure 3.7c shows the PBL stability states. The pattern of PBL stability states is different from the results with the other PBL schemes, which might be a result of the different treatment of the surface layer.

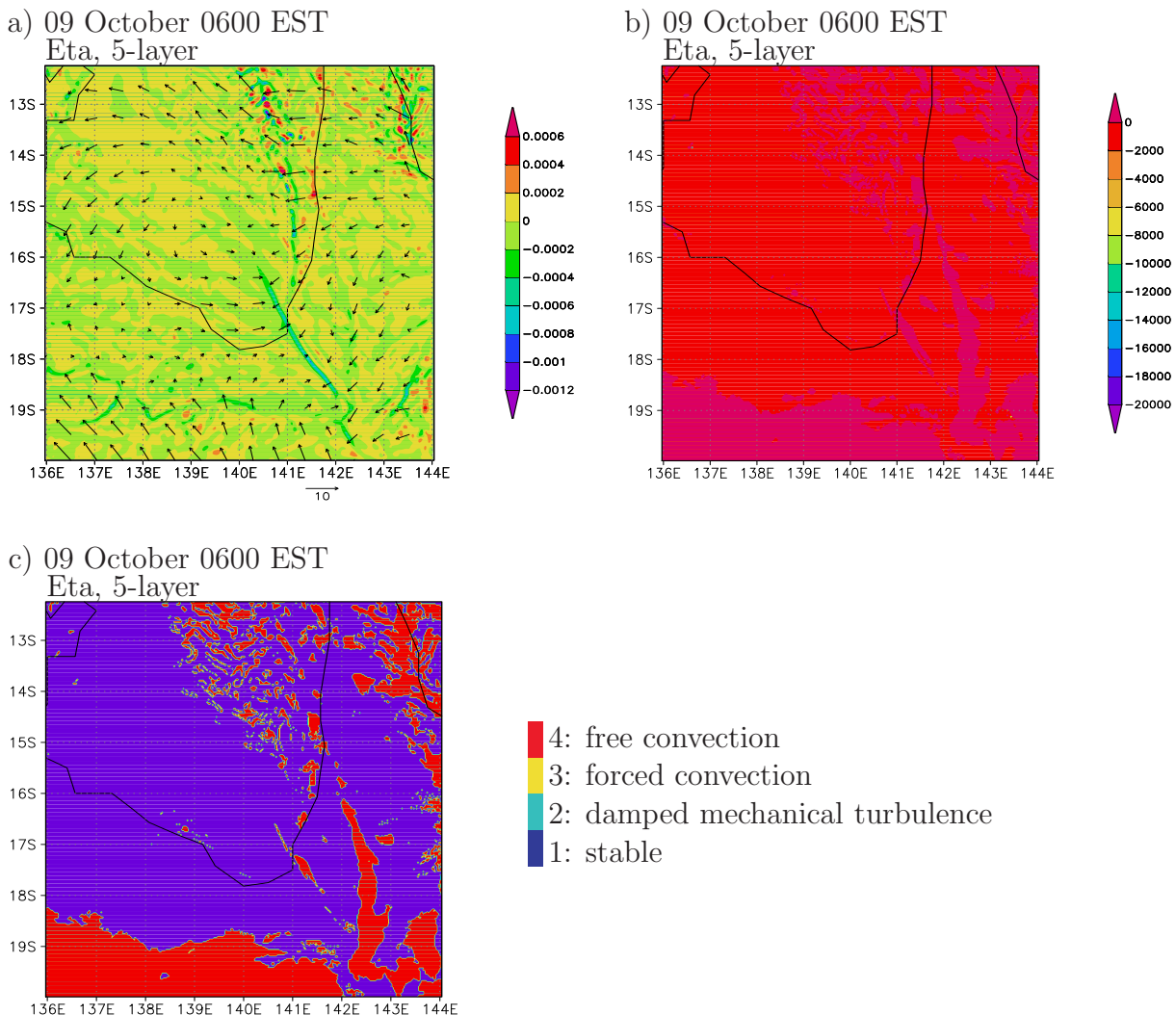


Figure 3.7: a) Low-level wind vectors (scale  $10 \text{ m s}^{-1}$  below panel) and divergence (shaded, unit  $\text{s}^{-1}$ ) at  $\sigma = 0.9975$ , b) Boundary layer height (in  $m$ ) and, c) PBL stability states at 0600 EST on 09 October.

### Gayno-Seaman

The Gayno-Seaman scheme is a level 2.5 Mellor-Yamada based scheme. In order to represent cloud water in a consistent way, the model uses liquid water potential temperature  $\theta_L$  and total water mixing ratio  $q_T$ , which are both conserved thermodynamic variables (Betts, 1973). The second statistical moment  $\overline{w'\theta'_L}$  is parameterised using a countergradient heat flux term  $\gamma_g$ , based on the sensible heat flux, boundary layer height and the convective vertical velocity scale (Therry and Lacarrere, 1983). The Gayno-Seaman scheme is the only PBL scheme within MM5 which advects TKE itself and which calculates both the horizontal and vertical diffusion of TKE. It necessarily interfaces with the force/restore soil model (in fact, MM5 offers the option to run the Gayno-Seaman scheme also with the 5-layer soil model, but the model crashes in this experiment). The surface fluxes for the Gayno-Seaman scheme are based on the same Monin-Obukhov similarity parameterisation used with the Blackadar scheme and the PBL stability states are determined using the same criteria (Shafran et al., 2000). The boundary-layer heights are calculated for all PBL stability states except for the stable state.

Figure 3.7a shows the low-level wind-divergence field and wind vectors at 0600 EST on 09 October. With the Gayno-Seaman scheme, southerly and north-easterly disturbances and a convergence line which corresponds to a NACL are captured with an accuracy of a few kilometres compared with the observations. The broken, north-south oriented line about 100 km west of the west coast of the peninsula corresponds to the NACL. The west-east oriented line in the south-eastern corner of the gulf corresponds to the southerly morning glory and the north-west to south-east oriented line at that position corresponds to the north-easterly morning glory. The region where both morning-glory convergence lines overlap is marked by strong convergence. A south-easterly morning glory is not captured in this model run. The MSLP correlation coefficient for this run is  $r = 0.92$ , which is much better than for the other two Mellor-Yamada based schemes.

Figure 3.8b shows the predicted PBL heights for the PBL stability states two to four, shown in Fig. 3.8c. The boundary-layer height is set to zero in regions where the stable regime is active. The countergradient heat flux is a function of the boundary layer height and takes effect only in regimes two to four. The PBL top is elevated along the morning-glory convergence lines and lowered in front of the NACL disturbance.

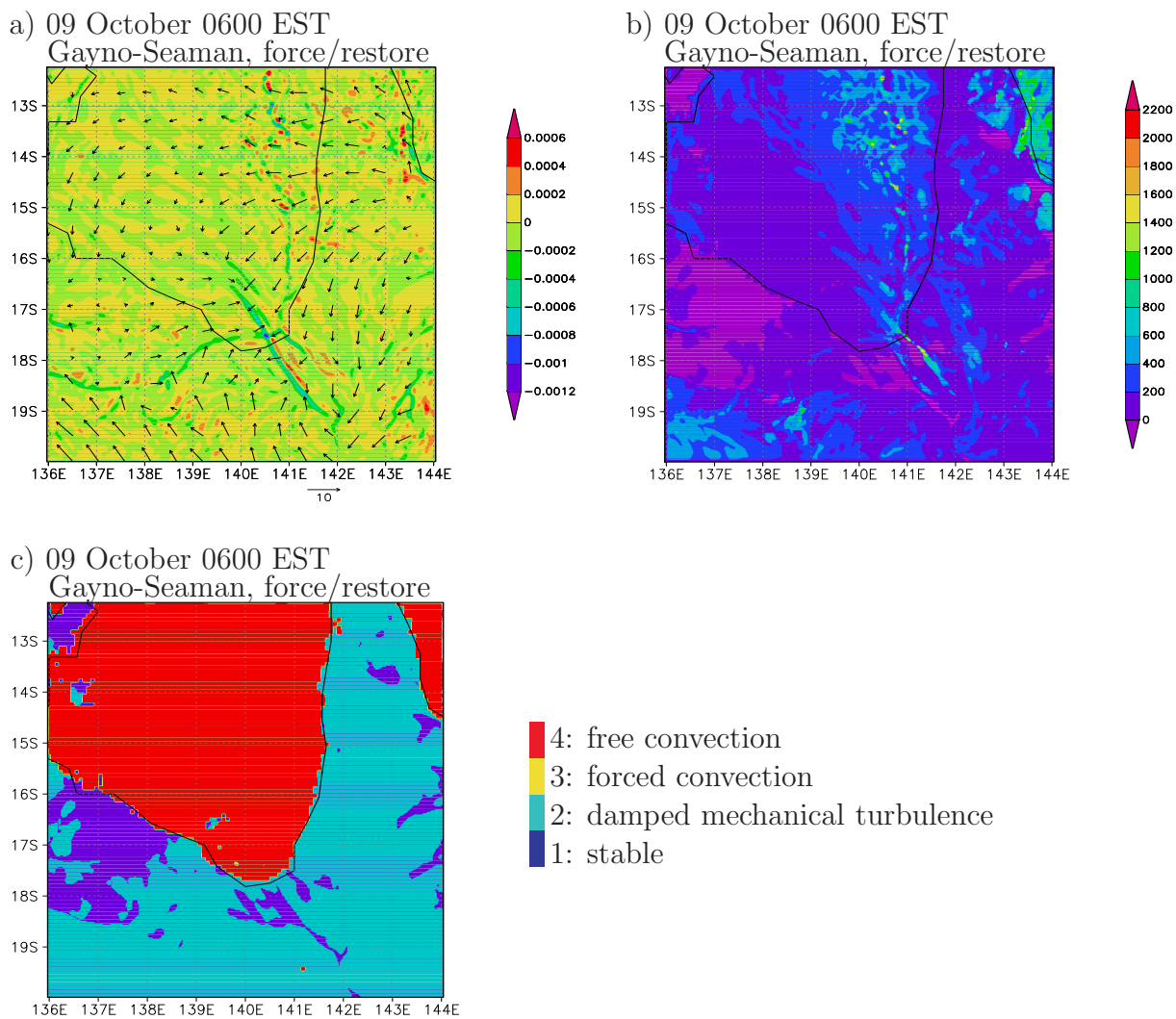


Figure 3.8: a) Low-level wind vectors (scale  $10 \text{ m s}^{-1}$  below panel) and divergence (shaded, unit  $\text{s}^{-1}$ ) at  $\sigma = 0.9975$ , b) Boundary layer height (in  $m$ ), and c) PBL stability states at 0600 EST on 09 October.

### 3.3.4 MRF

The MRF scheme was initially developed for the NCEP Medium Range Forecast system by Hong and Pan (1996) and was implemented in MM5 by Dudhia and Hong in 1996. This scheme applies nonlocal  $K$ -mixing for potential temperature  $\theta$  and water vapour mixing ratio  $q$  in the mixed layer, moist vertical diffusion in clouds (see the first section of this chapter) and local  $K$ -mixing above clouds and mixed layer to account for free atmospheric diffusion. The nonlocal mixing was implemented following a nonlocal diffusion concept by Troen and Mahrt (1986). The term "nonlocal" as it appears in the literature is a little misleading. Nonlocal mixing is the exchange flux between adjacent layers calculated by applying a correction term for the local gradient. This correction term incorporates the contribution of the large-scale eddies to the total flux. The eddy exchange coefficients  $K$  are calculated from a prescribed profile function of boundary layer heights and scale parameters. The surface fluxes are calculated in the same way as in the Blackadar scheme. The PBL stability states are determined using only the bulk Richardson number, again similar to the Blackadar scheme: The night-time stable state is assumed when  $Ri_b \geq 0.2$ . The damped mechanical turbulent state is assumed when  $0 < Ri_b < 0.2$ . The forced convection state is assumed when  $Ri_b = 0$ , and when  $Ri_b < 0$ , the daytime module is active. These changes increase the frequency of the daytime free convection state at the expense of the forced convection state.

Figure 3.9a shows the low-level divergence field and wind vectors at 0600 EST on 09 October. The convergence line over the south-eastern corner of the gulf with a south-east-to north-westward orientation corresponds to the north-easterly morning glory. The line is about 350 km long and broken at one position, close to the coastline. This break marks the position of the convergence line associated with the southerly morning glory. The broken convergence line north in the gulf, at about  $141^\circ\text{E}$ , parallel to the west coast of the peninsula corresponds to the NACL. The position of all these lines agree with the observations within a few kilometres. As in all simulations described here, the south-easterly morning glory is not captured by the model. Figure 3.9b shows the PBL height and Fig. 3.9c shows the PBL stability state at 0600 EST on 09 October. The PBL height is calculated in all PBL stability states and is elevated at the leading morning-glory convergence lines and lowered following their passage. In front the position of the NACL, the PBL height is lowered, as seen with the Gayno-Seaman- and Blackadar schemes. The MSLP correlation coefficient is  $r = 0.94$  for this model run, the highest value obtained in this study.

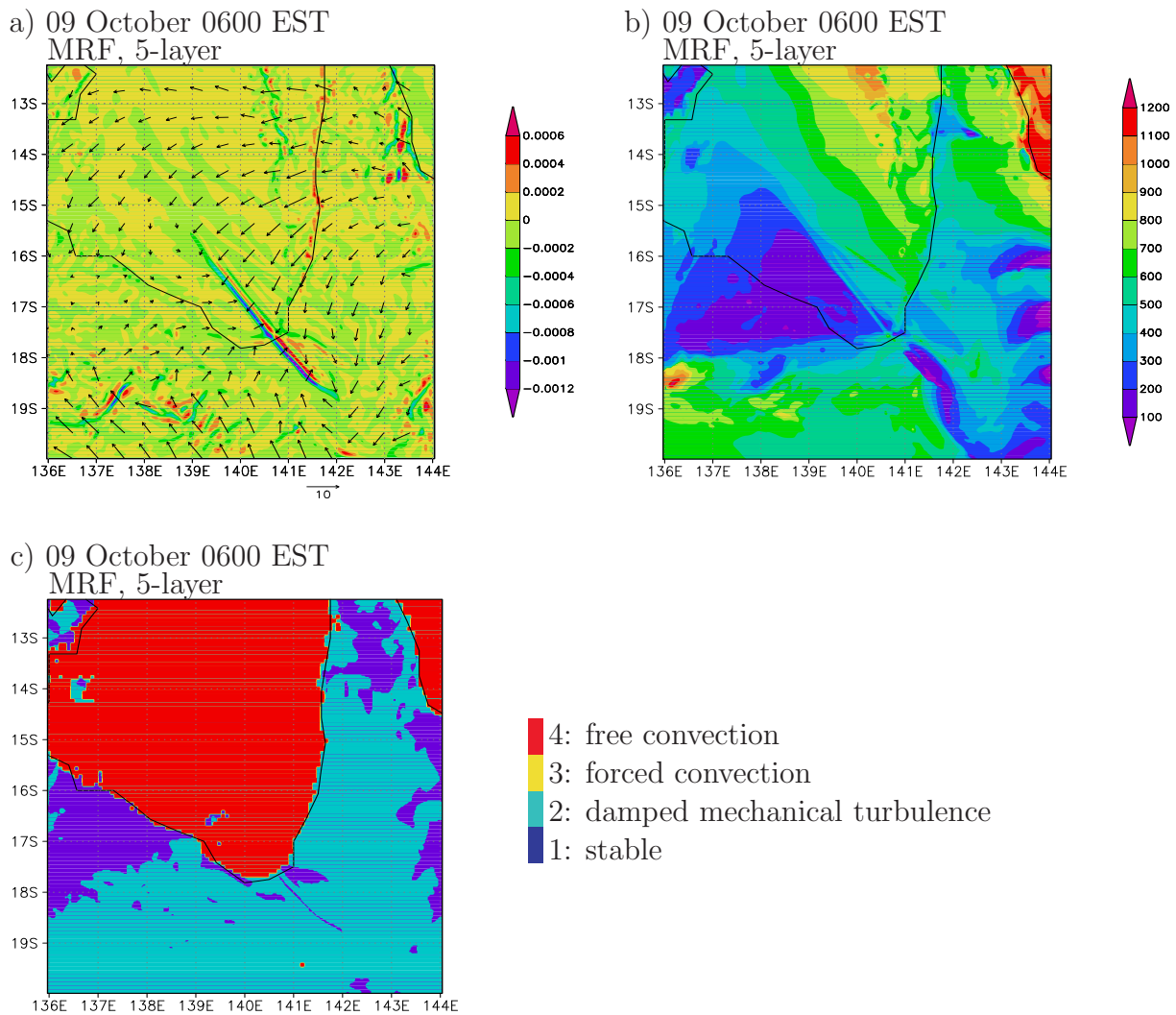


Figure 3.9: a) Low-level wind vectors (scale  $10 \text{ m s}^{-1}$  below panel) and divergence (shaded, unit  $\text{s}^{-1}$ ) at  $\sigma = 0.9975$ , b) Boundary layer height (in  $m$ ), and c) PBL stability states at 0600 EST on 09 October.

### 3.4 Summary

Table 3.1 lists the MSLP correlation coefficients for the experiments with the different PBL parameterisations described in the previous section. The results can be subdivided into three classes in terms of the magnitude of this coefficient, of the accuracy with which the lines were forecasted, and of the coherence of the lines. Based on this assessment, explicit modelling the PBL leads to the worst results, the Burk-Thompson and Eta schemes produce much better results, while the Blackadar, MRF and Gayno-Seaman schemes give the best results. While the weaknesses of explicit modelling are clear, the crucial difference between the best schemes and those that show more modest skill is not obvious. This difference was found to be the application of a term taking into account the countergradient fluxes. These are present in the daytime convective module of all the schemes that achieved a correlation coefficient of  $r > 0.90$  and are absent in all the schemes with  $r < 0.90$ . In the Blackadar scheme, the countergradient fluxes of water-vapour mixing ratio  $q$ , potential temperature  $\theta$ , and horizontal wind speeds  $u$  and  $v$  are handled by the transilient scheme. In the Gayno-Seaman scheme, the turbulent fluxes of the liquid water potential temperature,  $\theta_L$ , are calculated using a countergradient heat flux term. In the MRF scheme, the turbulence diffusion equations for potential temperature  $\theta$  and water vapour mixing ratio  $q$  apply a countergradient correction term. The MSLP correlation coefficient varies only little between these three schemes. All three schemes have in common that they allow for countergradient fluxes of the potential temperature, which suggests that the countergradient flux of this quantity is more important than the flux of moisture and momentum. A comparison of the results with the Eta- the Burk-Thompson- and the Gayno-Seaman schemes shows that the impact of the countergradient fluxes is even larger than the impacts of the different closures and land-surface schemes.

Table 3.1: Mean sea-level correlation coefficients with different PBL schemes and land surface models

Experiment number	Planetary-boundary-layer parameterisation	Land-surface scheme	Correlation coefficient
1	Explicit	Force/restore	0.60
2	Blackadar	Force/restore	0.93
3	Blackadar	Five-layer	0.93
4	Burk-Thompson	Force/restore	0.86
5	Eta	Five-layer	0.85
6	MRF	Five-layer	0.94
7	Gayno-Seaman	Force/restore	0.92

In the plots of the PBL stability states shown in the previous section, the daytime convective module was active only over the gulf, but these plots show the situation at

night-time. During the daytime, when the collision of both sea breezes generally occurs, the daytime convective module is active over land. The collision of the south-coast sea-breeze and the cold front generated by convergence into the trough as a precursor event to the southerly morning glory generally occurs during the night-time, when the nocturnal convective state is active.

Two additional experiments were carried out with the MRF scheme, one with the stable convective state only and one with the free convective state only. Using only the countergradient daytime convective module did not affect the results much, indicating that the collision of south-coast sea breeze and the cold front as well as the movement of both morning-glory lines are well-represented in the nocturnal stable states. With activating only the nocturnal stable state, the north-easterly morning-glory convergence line was significantly delayed (by about 100 km at 0600 EST on 09 October), but with little change in length and intensity. The southerly morning-glory line arrived at about the same time at the gulf coast as observed, while its intensity was weaker in this experiment than in the unmodified MRF model configuration. Thus, in this case the choice of PBL parameterisation has a larger impact on the northerly morning glory, which is generally generated late at daytime, than on the southerly, generally at night-time generated morning-glory line.

Since the best three MSLP correlation coefficients do not vary much, other criteria have to be considered for the choice of PBL parameterization. The Gayno-Seaman PBL scheme does not work with the soil moisture scheme and is therefore unsuitable for this study. The better treatment of the nocturnal boundary layer by the MRF scheme makes this scheme the choice for the simulations that I carried out.

## Chapter 4

# Sensitivity to soil moisture

### 4.1 The relevance of soil moisture in the Gulf of Carpentaria region

The soil moisture is defined as a dimensionless ratio of the volume of liquid water to that of soil. Since sea breezes are an intrinsic feature of the generation of morning glories, the position and speed of the sea-breeze fronts must determine the timing of these lines. The onset and speed of the sea breezes, in turn, are strongly affected by the soil moisture since a dry land surface warms up more rapidly as a result of the incoming solar radiation than a moist one. In the latter case, some of the incoming energy has to be used to evaporate water. Therefore a sea breeze towards a dry land surface with a larger temperature gradient between land and sea surface should be moving faster, all other features being the same. The following section describes briefly the way that soil moisture is treated in MM5 and in the ECMWF model. The subsequent sections give an overview of the model runs described in this chapter. They describe also the relation between soil moisture and the convergence lines in the Gulf of Carpentaria region and the search for optimum soil moisture values.

### 4.2 Soil moisture treatment in the ECMWF model and in MM5

In June 2000 the ECMWF introduced a revised surface model called the Tiled ECMWF Surface Scheme of Exchange processes at the Land surface (TESSEL). The maximum amount of water in any layer defines saturation (assumed to be at a soil moisture of 0.47). However, saturation can occur only during very short periods because the model will lose water due to bottom drainage. Field capacity represents the maximum value of soil moisture that the model can sustain for more than a few hours, in the absence of precipitation. The vegetated fraction of the soil evaporates at the maximum rate for soil

moisture larger than field capacity (assumed to be at a soil moisture of 0.32) and ceases evaporating below the permanent wilting point (assumed to be at a soil moisture of 0.17). A continuous variation of the soil moisture is allowed between the two extremes. The field capacity is defined as the soil water content after gravitational water drainage has become very slow and the water content becomes relatively stable. The term "permanent wilting point" is used in the documentation of TESSEL, but unfortunately is nowhere defined. A similar term, "permanent wilting point" is defined on the glossary web page of the American Meteorological Society. This term refers to the maximum soil moisture at the time when a plant will be under stress as a result of the deficiency in the soil moisture. The exact value of the permanent wilting point in TESSEL has significant effects on the utility of the ECMWF soil moisture data in tropical and subtropical arid areas since the soil moisture can be significantly drier in these regions. MesoLAPS simulations use typical values of soil moisture for the north Australian dry season between 0.012 and 0.015. If the values based on the Bureau's expertise in the Australian region are correct, the lower limit for soil moisture implied by TESSEL is much too low. Instead of soil moisture (SOILM), MM5 computes internally a quantity called moisture availability (MAVA). SOILM is converted to MAVA using a formula by J. Bresch<sup>1</sup>:

$$\text{MAVA} = \text{SOILM} \times 2 + (0.5 - \text{SOILM}) \times 0.09 \quad (4.1)$$

The MM5 bucket soil moisture model keeps a budget of soil moisture, allowing moisture availability to vary with time, particularly in response to rainfall and evaporation rates. In addition, MM5 applies certain minimum values for the wetness of the soil, depending on the vegetation type. In order to use reasonable soil moisture values for the MM5 configuration described in Section 1.5, I use SOILM=0.013 as consistent with the value in mesoLAPS as a reference value and convert into MAVA (=0.07). The lower limit for MAVA is then set to a value of 0.06 to allow for some drying.

### 4.3 Model configuration and experiments

For the same reasons as in Chapter 3, the 08/09 October event was chosen for this set of experiments. The model configuration described in Section 1.5 is used, but with changes to the moisture availability over land. MM5 is set up with moisture availability fields given in Table 4.1 and a minimum value of 0.01 is taken in all experiments described in this chapter. In order to determine timing differences of the various convergence lines with the different soil moisture initialisations, data were output at locations of the GLEX automatic weather stations at every time step.

---

<sup>1</sup>see the subroutine MM5/domain/io/rdinit.F

Table 4.1: Moisture availability (MAVA) and soil moisture (SOILM) in this set of experiments.

MAVA	SOILM	Adapted from
0.01	-0.018	
0.05	0.003	
0.07	0.013	mesoLAPS
0.13	0.044	
0.17	0.065	
0.27	0.118	
0.37	0.170	TESSEL
0.47	0.223	

## 4.4 Soil moisture impacts on the low-level convergence lines

To set the scene for the different model results, Fig. 4.1 and 4.2 show the low-level divergence fields at 0600 EST on 09 October. The south-westward displacement of the line corresponding to the north-easterly morning glory decreases and the convergence line is weaker as the soil moisture increases. The timing of the southerly morning-glory convergence line does not change appreciably, but the magnitude decreases with increasing soil moisture.

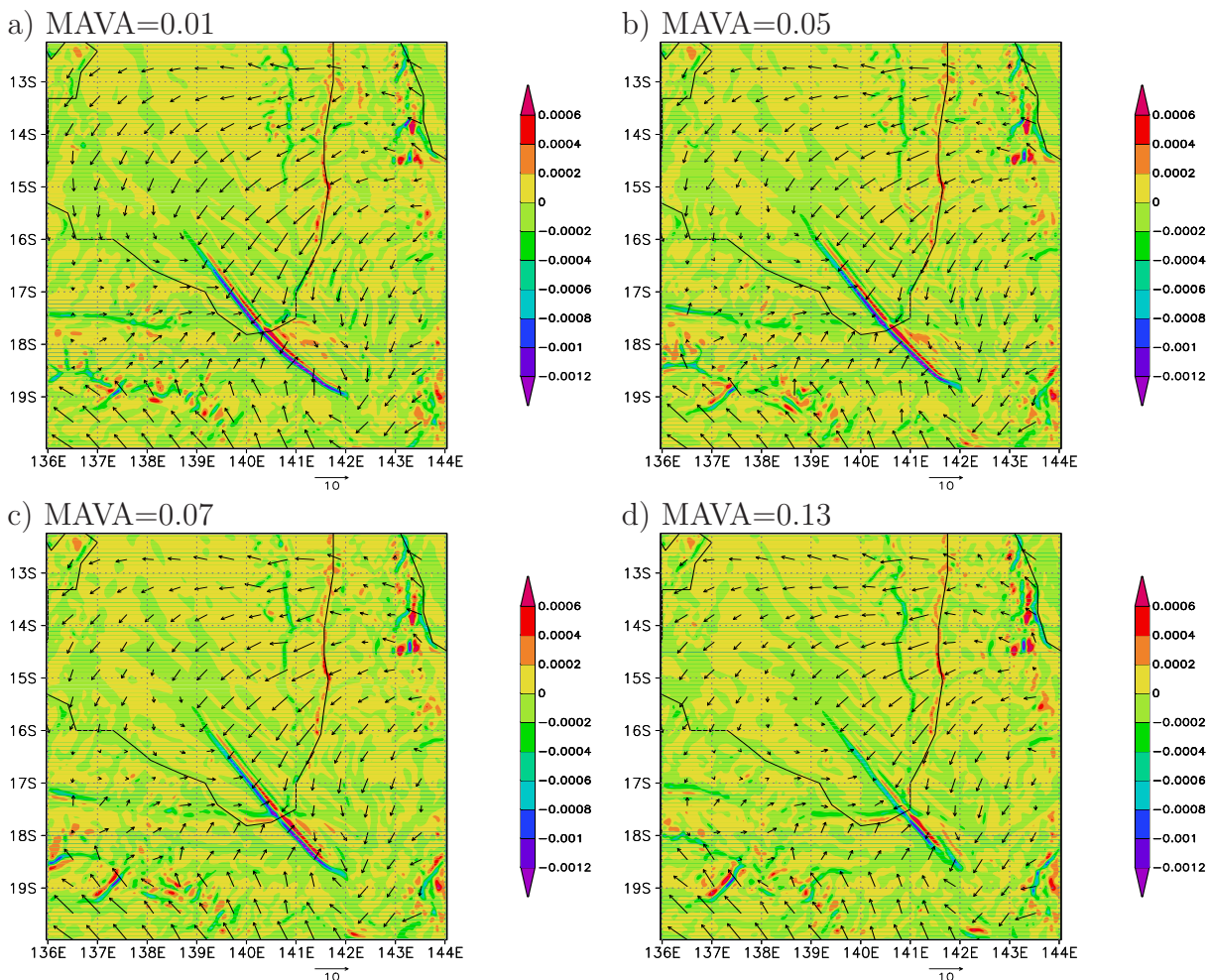


Figure 4.1: Sequence of plots of wind vectors (scale  $10 m s^{-1}$  below each panel) and divergence (shaded, unit  $s^{-1}$ ) at  $\sigma = 0.9975$  for the GLX run at 0600 EST on 09 October. The domain size is  $900 km \times 900 km$ .

#### 4.4. SOIL MOISTURE IMPACTS ON THE LOW-LEVEL CONVERGENCE LINES

The zonal position of the line corresponding to the NACL does not vary much with increasing soil moisture, but the magnitude of the low-level convergence increases. Plots at subsequent model output times not shown here indicate that the longevity of the NACL increases with increasing soil moisture. The explanation for this relationship is that the atmosphere above a moister ground becomes moister, promoting convective processes. The NACL, being a convective line, benefits from this circumstance. Indeed, the model produces cloud water at the position of the NACL convergence line, even in the driest soil moisture experiments. The amount of vertically integrated cloud water in the moistest case is about three times that in the driest case. As in the control experiment described in Section 2.5, none of the runs in this set of experiments produces a south-easterly morning-glory convergence line, indicating that there is no connection between soil moisture and the inability of the model to produce this line.

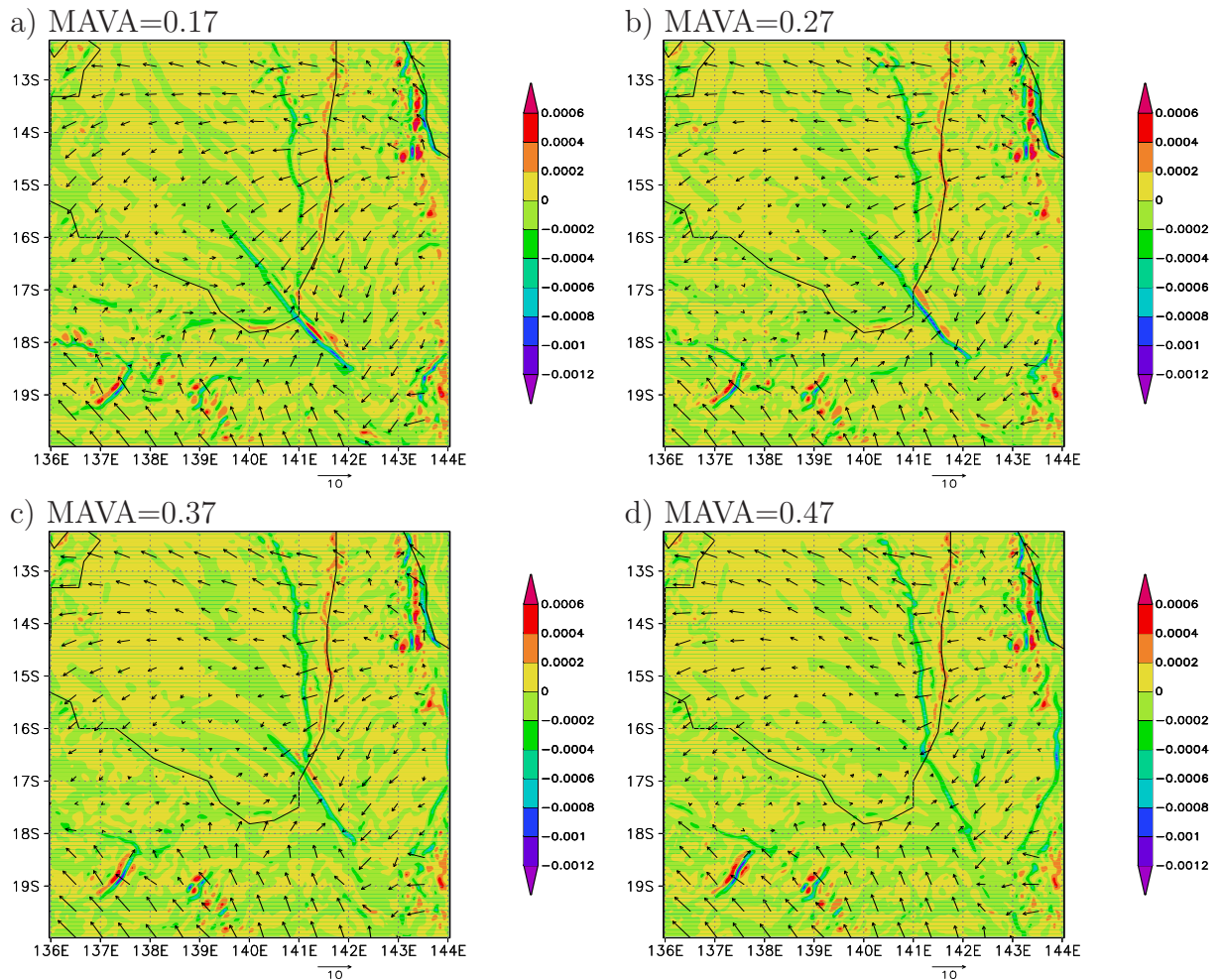


Figure 4.2: Continued from Fig. 4.1

Figure 4.3 shows the speed of the west-coast sea breeze between 1700 EST and 1900 EST on 08 October at  $14^\circ$  S. The error in the speed is estimated to be less than  $0.3 \text{ m s}^{-1}$ . The regression line was found using an implementation of the nonlinear, least-squares, Marquardt-Levenberg algorithm (Marquardt, 1963).

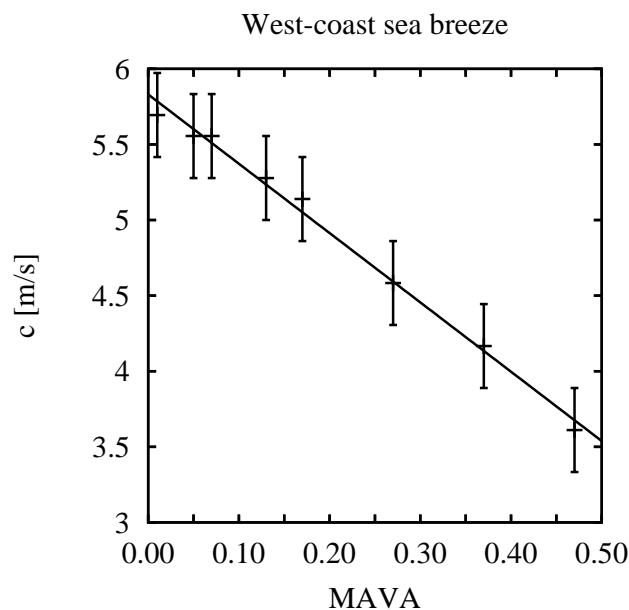


Figure 4.3: Average speed of the west-coast sea breeze between 1700 EST and 1900 EST on 08 October at  $14^\circ$  S with error bars and linear regression line.

The speed of the east-coast sea breeze does not vary much with increasing soil moisture, presumably because the easterly background flow over Cape York Peninsula is a strong drive for this sea breeze. The increase of speed of the west-coast sea breeze with decreasing soil moisture leads to collision points of the two sea breezes moving eastwards with decreasing soil moisture.

Figure 4.4 shows the average propagation speed of the north-easterly morning-glory convergence line between Dunbar and Van Rook in the model. Not only is the west-coast sea breeze slowed down with increasing soil moisture, but also the north-easterly morning glory. The propagation speed was calculated taking the time of the peak wind speed following the maximum increase of the 10-m wind speed associated with the morning-glory disturbance at Dunbar and Van Rook. The resulting speed was multiplied with the sine of the angle between the line Dunbar-Van Rook and the convergence line. The error in the angle was estimated to be less than  $5^\circ$ . The relative flow behind the line as calculated in Chapter 2 shows that for all soil moisture values, the north-easterly morning-glory

disturbance has a bore-like character at this stage.

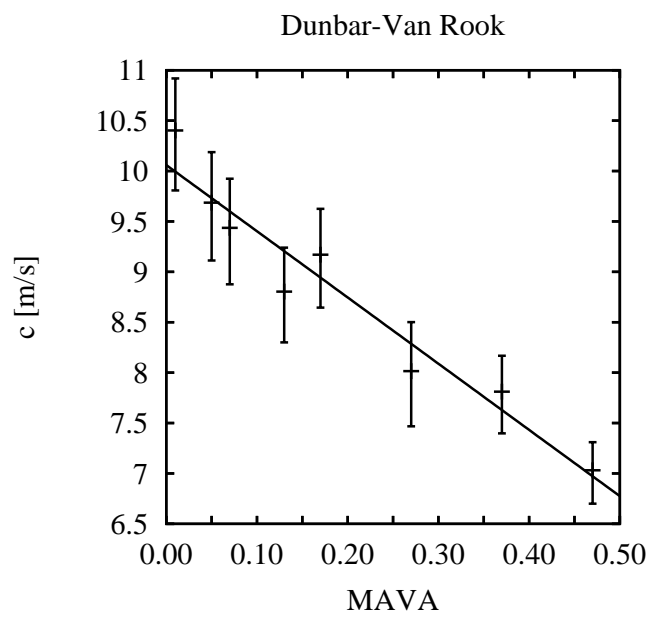


Figure 4.4: Propagation speed of the north-easterly morning-glory line between Dunbar and Van Rook with error bars and linear regression line.

Figure 4.5a shows the average inland speed of the south-coast sea breeze at  $140^\circ$  E between 2100 EST and 2300 EST. The error was estimated to be less than  $0.3 \text{ m s}^{-1}$ . The translation speed of the south-coast sea breeze decreases with increasing soil moisture. Figure 4.5b shows the distance of the cold front from the coastline at  $140^\circ$  E at 2300 EST on 08 October. The error was estimated to be less than 5 km. The cold front moves northwards more rapidly with increasing soil moisture. This is as would be expected since the south-coast sea breeze and the cold front are opposing flows.

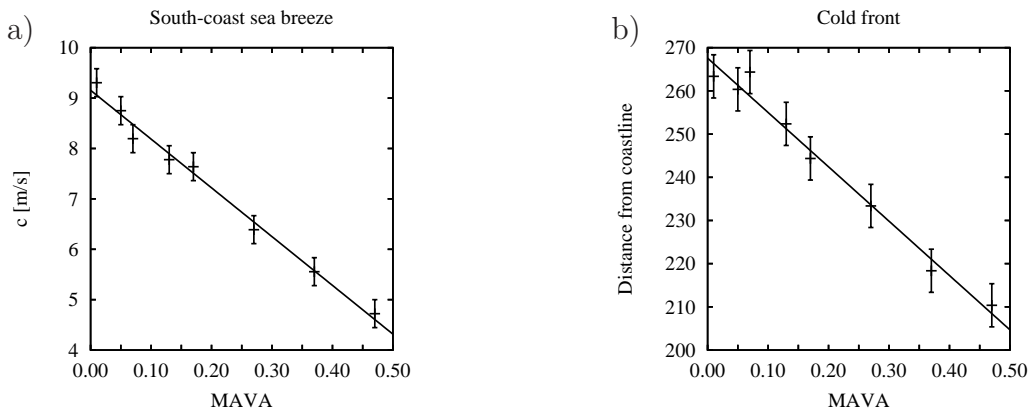


Figure 4.5: Left panel shows the speed of the south-coast sea breeze between 2100 EST and 2300 EST on 08 October at  $140^\circ$  E with error bars and linear regression line. The right panel shows the distance of the cold front at  $140^\circ$  E from the coast at 2300 EST on 08 October with error bars and linear regression line.

The increase in speed of the cold front and the reduction in speed of the south-coast sea breeze with increasing moisture lead to a collision point of the cold front and the sea breeze further north. From the one-hour model output the exact time of collision cannot be determined, but animations of the low-level divergence fields indicate that the collision occurs slightly earlier (less than one hour) with increasing soil moisture.

Figure 4.6a shows the time of arrival of the southerly morning-glory disturbance at Augustus Downs on 09 October. The difference between earliest and latest arrival times of this disturbance is less than 30 min. The southerly disturbance arrives earlier at Augustus Downs with increasing soil moisture because Augustus Downs is located close to the collision point of the cold front and the south-coast sea breeze. The point of intersection of the line corresponding to the observation and the regression line is at  $\text{MAVA} = 0.22$  and will be discussed in the next section.

Figure 4.6b shows the average propagation speed of the southerly line between 0200

EST and 0600 EST at 140° E on 09 October as a function of soil moisture. The speed of the southerly morning-glory convergence line is reduced also with increasing soil moisture. An analysis of the relative flow behind the line shows that within this time frame, the southerly disturbance retains a bore-like character in all experiments.

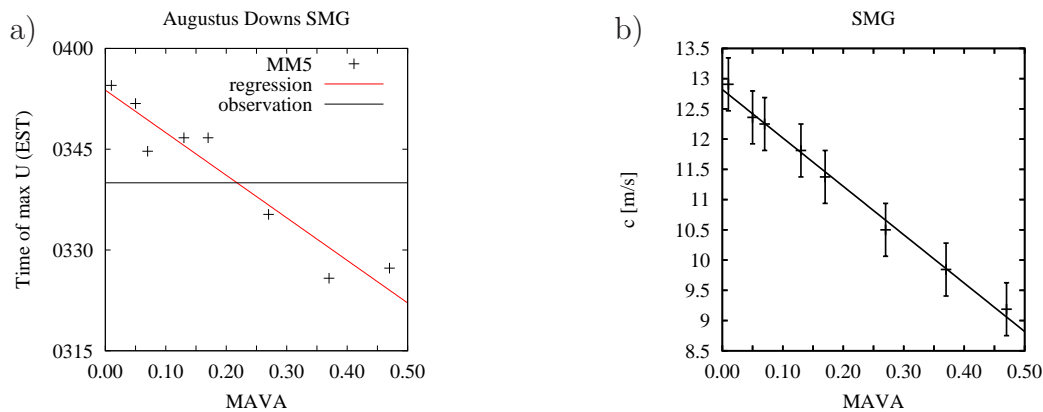


Figure 4.6: The left panel shows the time of arrival of the southerly morning-glory disturbance at Augustus Downs on 09 October with regression line and a line corresponding to the observation (0340 EST). The right panel shows the propagation speed of the southerly morning-glory convergence line between 0200 EST and 0600 EST on 09 October at 140°E and the regression line.

Figure 4.7 shows the time at which the dry line arrives at Augustus Downs as measured by the time of maximum decrease in 2-m water-vapour mixing-ratio within the time frame 0500 EST to 0800 EST on 09 October. The dry line was observed at Augustus Downs at 0715 EST on 09 October. The arrival time in the model does not change until the soil moisture exceeds a certain wetness, above which the dry line arrives earlier with increasing soil moisture. The reason for this increase is that the speed of sea-breeze front declines with increasing soil moisture. The sea breeze opposes the southerly flow which precedes the dry line. The cold front is directly followed by the dry line and one would expect analogous speed changes with varying soil moisture. The insensitivity in arrival times for low soil moisture values is indicated by animations of the low-level moisture field. At these low values, the dry line is quite curvy and, by chance, it arrives at same times at Augustus Downs. Nevertheless the mean translation speed of the line does decrease with increasing soil moisture. At higher soil moisture values, the dry line becomes straighter. For this reason, only the four data points from MAVA = 0.17 to MAVA = 0.47 were used to obtain the regression line. The intersection point of the regression line and the observed arrival time at MAVA = 0.06 will be discussed in the following section.

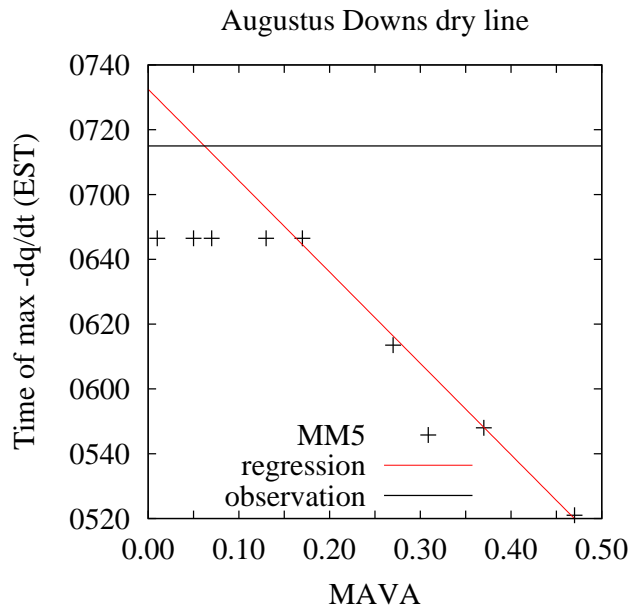


Figure 4.7: Arrival time of the dry line, associated with the maximum 2-m moisture gradient, at Augustus Downs on 09 October and regression line for data points at  $MAVA \geq 0.17$ .

## 4.5 Finding the "optimum" soil moisture value

For an optimum soil moisture initialisation, for which the model results agree as closely as possible with the observations, a four-dimensional data assimilation (4DDA) is needed. The 4DDA would provide an optimum moisture distribution with many degrees of freedom. Such an analysis is beyond the scope of this study, and the problems in using much simpler approaches are described in this section. The first approach would be to find just one optimum value for the initialisation of the whole land surface in the model.

Figure 4.6a, Fig. 4.7 and Fig. 4.8 show the arrival time of the north-easterly and southerly morning glory disturbance and the dry line for different soil moisture initialisations at different stations in the model, a regression line and a line corresponding to the observation. The point of intersection of these two lines indicates an optimum soil moisture value for the particular morning glory disturbance or the dry line at the particular station. The points of intersection of the regression line with the line corresponding to the observed time of the passage of the southerly morning glory in Fig. 4.6a and of the dry line in Fig. 4.7 at different soil moisture values (at  $MAVA = 0.22$  and  $MAVA = 0.06$  respectively) highlights the problem of finding an optimum soil moisture initialisation.

Figure 4.8 shows that even for a particular disturbance, the MAVA value at the points of intersection in this figure (at  $MAVA = 0.23$  for Dunbar and at  $MAVA = 0.13$  for Van Rook) can vary significantly. The left panel shows the arrival time of the north-easterly morning-glory disturbance at Dunbar and the right panel at Van Rook (associated with the peak wind speed following the maximum increase of the 10-m wind speed between 2000 EST on 08 October and 0600 EST on 09 October at Dunbar and between 0000 EST and 0500 EST on 09 October at Van Rook). The large variance in moisture values at intersection points of lines corresponding to the observations and regression lines precludes the use of these intersection points to determine an optimum soil-moisture value.

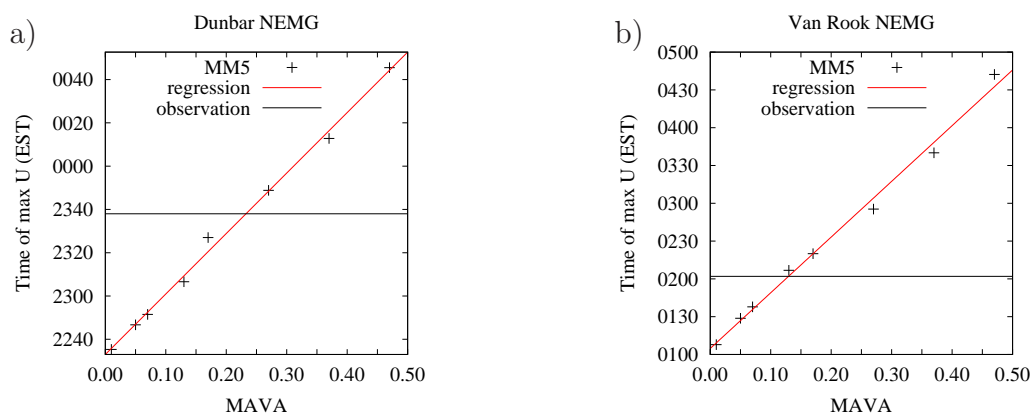


Figure 4.8: Arrival time of the north-easterly morning-glory disturbance and linear regression line at Dunbar (left panel) and Van Rook (right panel) with observations.

Another possible approach to find an optimum soil moisture is to consider the average soil moisture trend over a certain time period (one day in this case). During the integration time, the moisture fluxes in the model from and towards the surface may balance and give an optimum value for the soil moisture. Figure 4.9 shows the soil moisture averaged over domain 2 (see Fig. 1.7b) over a 24 h integration time. Even in the unrealistically dry soil case ( $SOILM = 0.00$ ), the soil moisture still decreases. Only in the experiment with  $MAVA = 0.01$  initialisation does the soil not dry out any further. In fact, the average soil moisture even doubled after half a day caused by condensation at the surface. A further drying of the soil in this experiment was prevented by the lower limit of  $MAVA_{min} = 0.01$ . All possible values for the minimum soil moisture applied in TESSEL and in MM5 are determined empirically and may not be realistic for the Gulf of Carpentaria region. Therefore this approach cannot be used here either.

Figure 4.9b shows the MSLP correlation coefficients for the different soil moisture initialisations. The regression line was calculated assuming a quadratic function. The correlation coefficient increases monotonically with decreasing soil moisture.

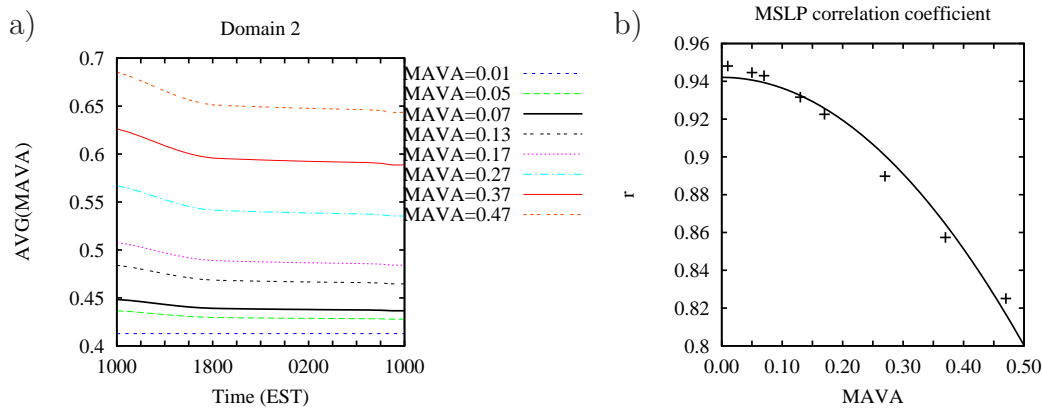


Figure 4.9: Soil moisture average for domain 2 (constant moisture of ocean areas included) for different soil moisture initialisations (left panel) and MSLP correlation coefficients with quadratic regression line.

Hess (2001) describes a way of finding soil moisture values through the 2-m dewpoint field. A simple comparison of the 2-m dewpoints in the model with the observations at certain times at certain stations as described earlier for the arrival times of the lines would be problematic for the same reason as described earlier for the timing of particular events. A four-dimensional data assimilation of the 2-m dewpoint field as by Hess is beyond the scope of this study.

An appropriate approach for finding optimum soil moisture values is not available and there are no measurements of actual soil moisture values from the GLEX experiment. For this reason, I rely on the values provided by the Australian Bureau of Meteorology for the soil moisture initialisation.

## 4.6 Summary

The treatment of soil moisture in the MM5 and ECMWF models was briefly introduced and the model configuration for the experiments in this set of experiments was described. The extent to which the different soil moisture initialisations influence the low-level convergence lines in the Gulf of Carpentaria region was discussed. The speed of the morning-glory convergence lines was found to increase linearly and the speed of the nocturnal front and of the dry line was found to decrease linearly with decreasing soil moisture. The variation of the MSLP correlation coefficients and of the position of the convergence lines was discussed in the previous section. The results provide a basis for the choice of soil moisture values in the calculations described in earlier chapters.

# Chapter 5

## The role of orography

### 5.1 Motivation

This chapter examines the impact of the orography in the Gulf of Carpentaria region on the low-level convergence lines in this study. A theoretical study by Porter and Smyth (2002) using the weakly-nonlinear Benjamin-Ono theory suggested that the morning glory could be generated by the interaction of the east-coast sea breeze and the Great Dividing Range on Cape York Peninsula. Also, the results described in Chapter 2 suggest that the orientation of the coastline on the eastern side of Cape York Peninsula plays a significant role in the separation of the NACL- and morning-glory convergence lines. In order to study these two effects as well as the impact of the orography in the Mount Isa region on southerly morning glories, I describe below a series of calculations in which the MM5 orography is modified. A technical description of the modifications and their impacts to the model initialisation is given in Appendix C.

### 5.2 Model configuration and experiments

As in the previous two chapters, the 08/09 October event is chosen for the experiments described in this chapter. Three sets of experiments are carried out as listed in table 5.1. In the first set, the height of the orography is scaled while everything else remains unchanged. In the first experiment, orography is totally flattened (set to 1 m everywhere on land), while in the second experiment orography is elevated by a factor of two. In the second set, the orography is flat and the shape of Cape York Peninsula is modified. There are two experiments of different length of the peninsula at uniform width and one experiment with a triangular shape. In the third set, terrain height is unmodified and the Gulf of Carpentaria is filled with land (of 1 m height above sea level). Apart from the modifications given in table 5.1, no changes have been made to the general model configuration described in Section 5 of Chapter 1.

Table 5.1: Overview of the experiments described in this chapter.

Experiment number	Terrain height factor	Cape York Peninsula modification	Gulf of Carpentaria modification
1	0		
2	2		
3	1		filled (1 m height above sea level)
4	0	coast at 141.6°E and 143.54°E north of 14.7°S	
5	0	coast at 141.6°E and 143.54°E north of 17.5°S	
6	0	triangle-shaped	

Figure 5.1 shows the terrain height fields in experiments 1 to 6. Where the coastline has been modified (the real coast line is indicated in all plots), the land-use type was set to "Savannah", a common soil type in north Australia.

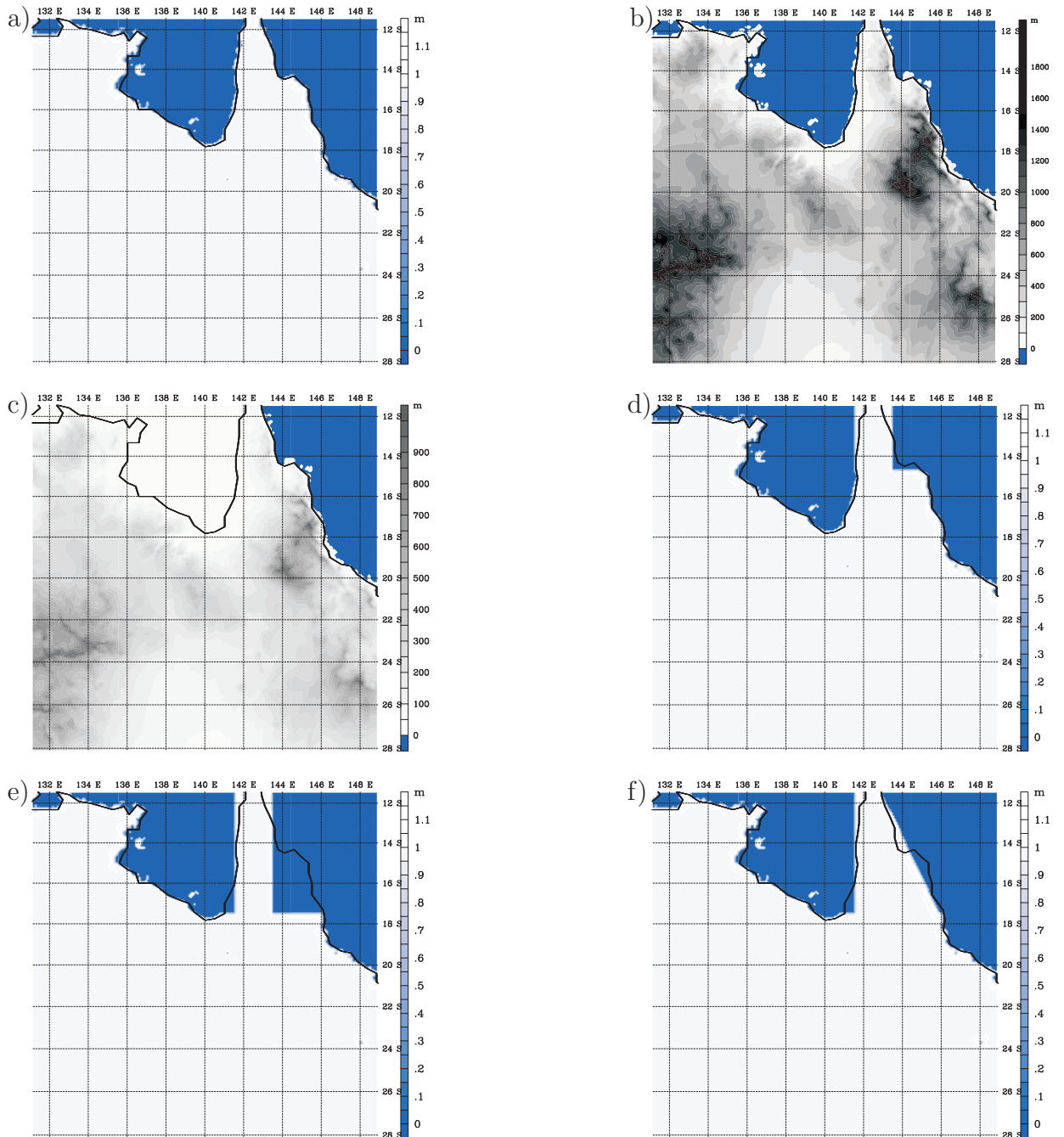


Figure 5.1: Panels a) to f) show the terrain height in the large domain in experiments 1 to 6.

### 5.3 The impact of the orography surrounding Mount Isa and the Great Dividing Range

Figure 5.2 shows the low-level wind divergence and wind vectors at two different times for three different terrain elevation factors. The MM5 terrain height, which is close to the real terrain height, is multiplied by 0, 1 and 2 where the factor 1 refers to the GLX experiment described in Chapter 2.

The plots in the left panels show the situation at 2000 EST on 08 October. By this time, the gulf-coast sea breeze, marked by an arc of strong convergence surrounding the Gulf of Carpentaria, as well as the east-coast sea breeze have travelled far inland. The collision of both sea breezes has commenced in panels (a) and (e) and is about to begin in panel (c). There is no systematic dependency of the speed of the sea breezes on the topography height. The sea breezes are displaced furthest inland in experiment 2 and least far in the GLX experiment. If the upslope winds play a significant role in this case or not cannot be determined with this few experiments as a blocking effect might play a role as well with increasing topography height.

The right panels show the situation at 0600 EST on 09 October. By this time, convergence lines corresponding to north-easterly and southerly morning glories and to an NACL have formed. The lines corresponding to the north-easterly disturbance are located in the south-eastern corner of the gulf and are oriented in a north-west to south-eastward direction. The line captured by the GLX experiment with the most realistic terrain height is stronger than in the other two experiments. The convergence line has travelled furthest into the southern gulf area in experiment 2 and least far in the GLX experiment. The lines corresponding to the southerly morning glory are situated close to the southern gulf coast in all three experiments. This line has moved furthest to the north in experiment 2 while there is little variation in its intensity. The line corresponding to the NACL is at about  $141^\circ$  E in all three model runs. The line is more coherent in the GLX experiment and experiment 1 than in experiment 2.

The generation of the convergence lines associated with the NACL and the morning glories in the calculation with a flat surface show that the flow over orography is not necessary for the generation of these lines. This result is consistent with the findings of Noonan and Smith (1987).

Plots of the relative flow behind the lines indicate that both morning-glory convergence lines undergo a transition to a bore-like flow character. This transition occurs after the west-coast sea breeze collides with the east-coast sea breeze for the north-easterly disturbance and after the collision of the cold front with the south-coast sea breeze for the southerly disturbance. The convergence lines corresponding to the NACL maintain a

gravity-current like flow after the collision of the west- and east-coast sea breeze. These plots are not shown here.

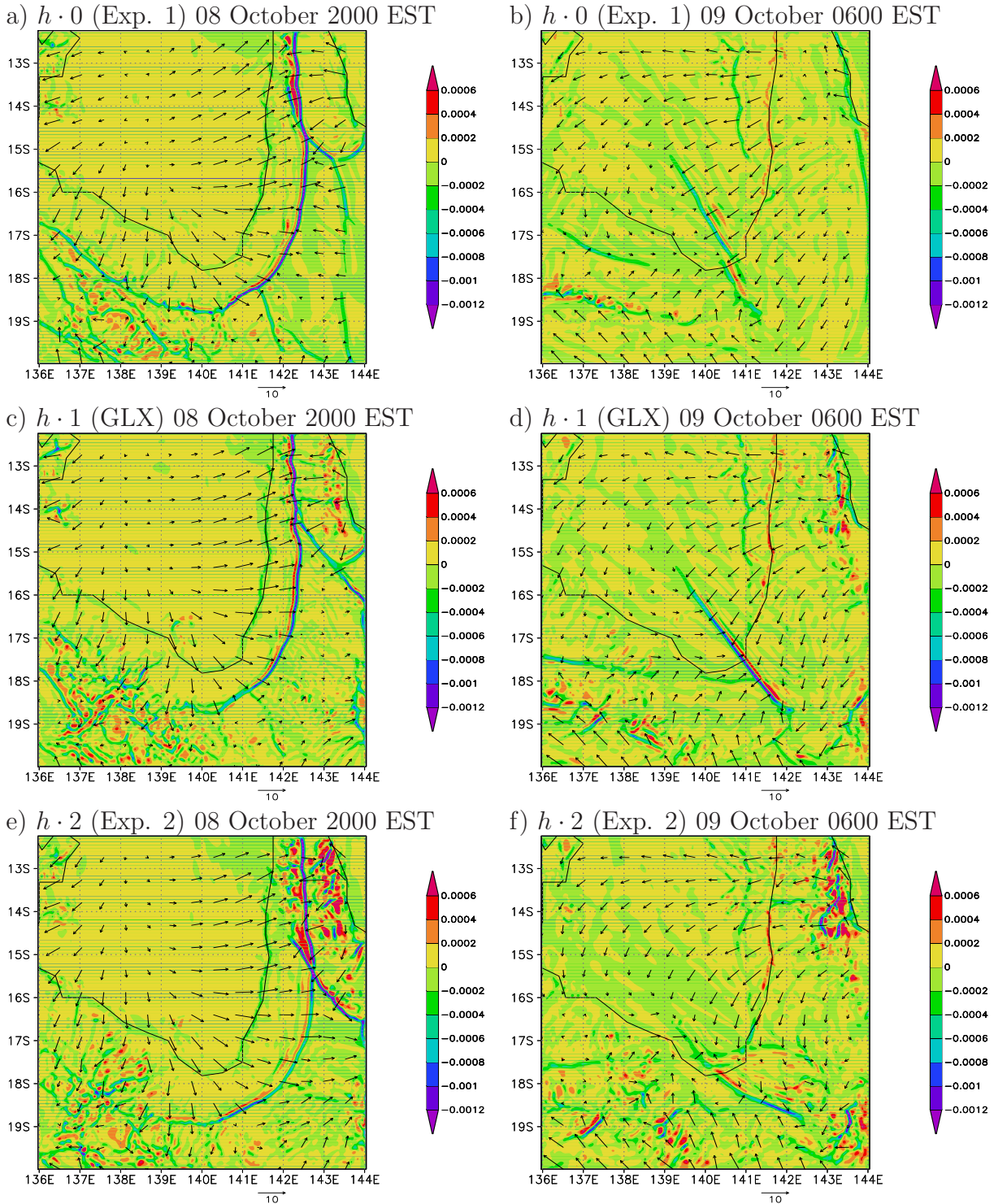


Figure 5.2: Sequence of plots of wind vectors (scale  $10 \text{ m s}^{-1}$  below each panel) and divergence (shaded, unit  $\text{s}^{-1}$ ) at  $\sigma = 0.9975$  for experiment 1 (panels a) and b)), experiment 2 (panels e) and f)) and the general model configuration (panels c) and d)). The terrain elevation factor is stated at the top of each plot.

## 5.4 The impact of the Gulf of Carpentaria

The experiment with the filled Gulf of Carpentaria (experiment 3) was designed to investigate the impact of the Gulf of Carpentaria sea breeze on the formation of morning-glory convergence lines. By filling the Gulf of Carpentaria and northern sea areas with land of 1 m height above sea level, the formation of sea breezes around the gulf is suppressed. Then the collision of the west-coast sea breeze and the east-coast sea breeze does not occur. Likewise the collision of the cold front and the south-coast sea breeze does not occur.

Figure 5.3 shows the low-level divergence field and the air temperature at a height of 2 m at 0400 EST on 09 October. The convergence line at about  $18^\circ$  S is associated with ageostrophic flow towards the trough line. The deformation associated with this flow has generated a cold front, marked by a sharp temperature gradient. The north-west to south-east oriented convergence line is associated with the east-coast sea breeze. The position of the east-coast sea breeze is marked also by a sharp temperature gradient. The convergence line between  $14^\circ$  S and  $15^\circ$  S is not of interest here because it corresponds to the artificial north-coast sea breeze.

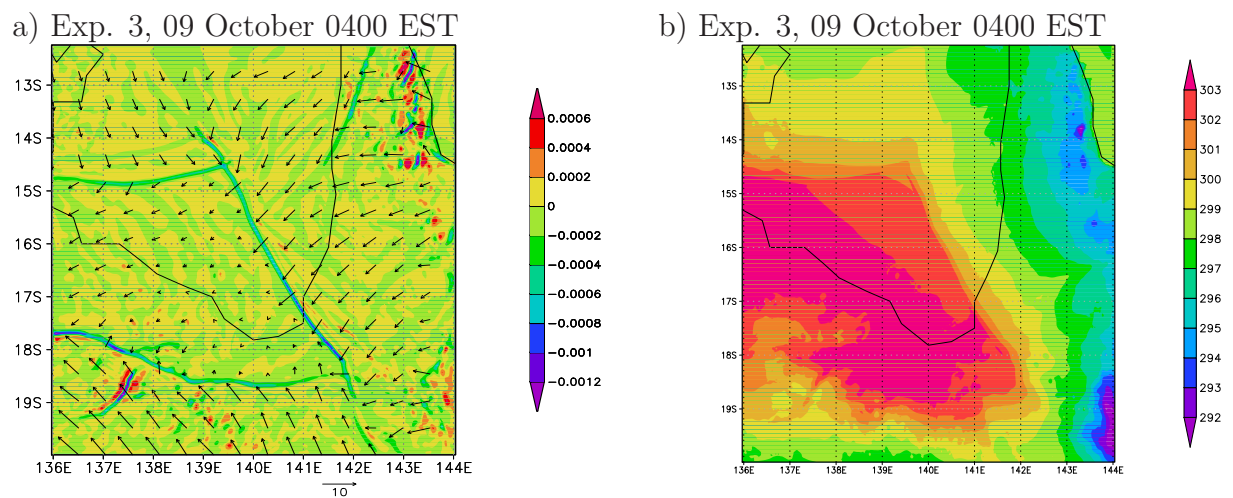


Figure 5.3: Wind vectors (scale  $10 \text{ m s}^{-1}$  below each panel) and divergence (shaded, unit  $\text{s}^{-1}$ ) at  $\sigma = 0.9975$  (left panel) and water vapour mixing ratio (kg/kg) (right panel) for experiment 3.

Figure 5.4 shows the relative flow,  $u - c$ , behind the convergence lines associated with the east-coast sea breeze (left panel) and the cold front (right panel) at 0400 EST on 09 October. In these calculations the angle of the convergence line corresponding to the cold

front is  $90^\circ \pm 1^\circ$  and the angle of the east-coast convergence line corresponding to the sea breeze is  $20^\circ \pm 1^\circ$  measured anticlockwise from north. The mean propagation speeds of the lines are  $\sim 10.8 \pm 0.5 \text{ m s}^{-1}$  and  $\sim 10.0 \pm 0.5 \text{ m s}^{-1}$ , respectively. Neither east-coast sea breeze nor the cold front undergo a transition to a bore-like flow disturbance.

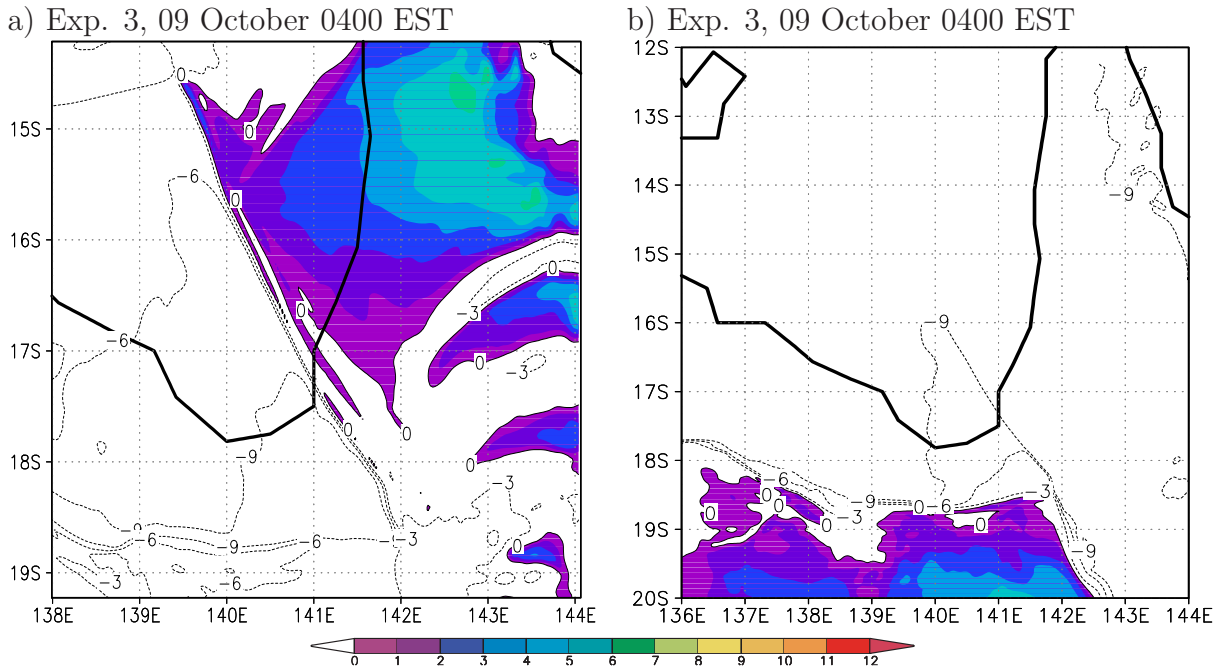


Figure 5.4: Calculations of the relative flow,  $u - c$  (in  $\text{m s}^{-1}$ ), normal to and behind the north-easterly sea-breeze convergence line (left panel) and the cold front (right panel) at  $\sigma=0.965$ . Positive values of  $u - c$  are shaded.

In this experiment, the convergence line corresponding to the east-coast sea breeze and the line of convergence associated with ageostrophic flow into the trough coincide with strong moisture gradients. Both lines retain a gravity-current-like flow behaviour and no morning-glory disturbance is generated even though there is orography in this case.

## 5.5 The impact of the shape of Cape York Peninsula

Experiments 4 to 6 were designed to investigate the effect of the shape of the peninsula on the formation and separation of the north-easterly morning glory and the NACL. In the experiments described in Chapter 2 the NACL convergence line is approximately parallel to the east coast north of  $14^{\circ}\text{S}$ , while the north-easterly morning-glory convergence line is approximately parallel to the east coast south of this latitude. This suggested that both lines originate from the east-coast sea breeze at the particular latitudes. Experiments 4 and 5 seek to investigate the influence of the latitude of the east-coast bend on the separation point of these two convergence lines. The latitude where the east coast has a sharp bend is varied in these two experiments (see again Fig. 5.1). In experiment 6 the east coast is uniform throughout the length of the peninsula. This experiment serves to answer the question if distinct convergence lines corresponding to an NACL and a north-easterly morning glory form without the sharp bend of the east coast close to  $14^{\circ}\text{S}$ .

Figures 5.5 to 5.7 show the temporal evolution of the convergence lines in the three experiments 4 to 6. Panel (a) of Fig. 5.5 shows the situation at 1800 EST on 08 October. The arc of strong convergence (marked A) south-west of the bend in the coast line of the modified Cape York Peninsula is the sea breeze penetrating inland from that position. The gulf-coast sea breeze has already formed and is marked by an arc of strong convergence (marked B) inland from the gulf. By 2200 EST, the collision of the east- and west-coast sea breezes has commenced. Two distinct convergence lines have formed to the north-west of the collision point (marked C). The northern part (marked D) has formed after the collision of the west-coast sea breeze and the east-coast sea breeze north of the arc of convergence marked A. The (short) southern part (marked E) has formed after the collision of the west-coast sea breeze and this arc of convergence. By 0200 EST on 09 October, a southerly morning glory, two distinct north-easterly morning-glory convergence lines and an NACL have formed. Animations of the low-level divergence field between 2200 EST on 08 October and 0200 EST on 09 October show that the southernmost of the two north-easterly convergence lines (marked F) has formed after the collision of west-coast sea breeze and the east-coast sea breeze south of the bend in the coast line. The northerly of the two north-easterly convergence lines (marked G) has formed after the collision of the west-coast sea breeze and the sea-breeze arc marked A. The NACL (marked H) has formed after the collision of the west-coast sea breeze and the east-coast sea breeze north of this bend. The southerly morning glory convergence line is marked I. Panel (d) shows the situation at 0600 EST. By this time, the two north-easterly convergence lines propagated further to the south-west. The convergence lines corresponding to the southerly morning glory and the NACL have propagated further into the gulf.

In this configuration, the artificial east-coast bend is close the latitude of its real counterpart. The model produces results which are comparable to the experiment described in Chapter 2, despite of the rectangular shape of the peninsula.

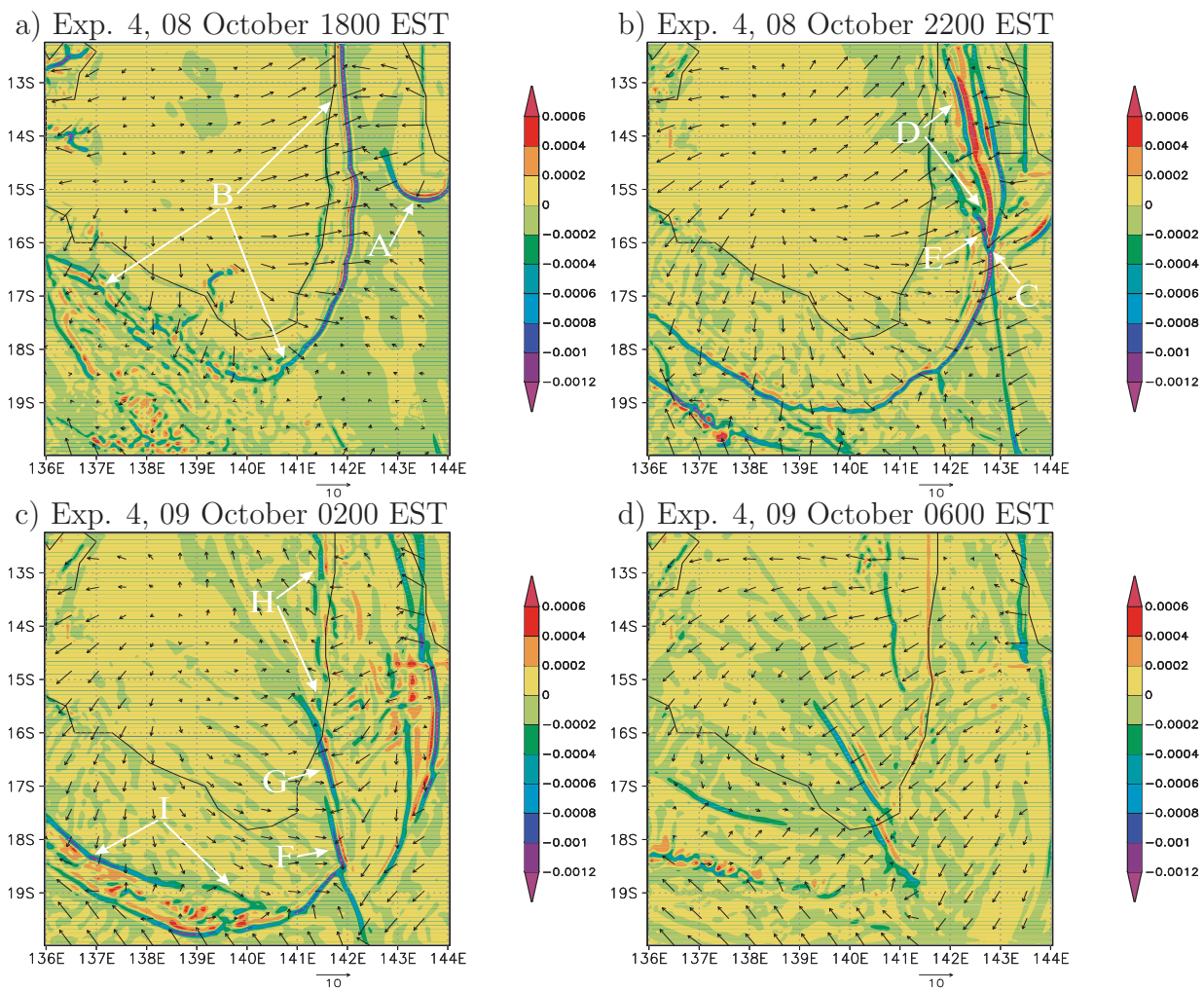


Figure 5.5: Sequence of plots of wind vectors (scale  $10 \text{ m s}^{-1}$  below each panel) and divergence (shaded, unit  $\text{s}^{-1}$ ) at  $\sigma = 0.9975$  for experiment 4 at different times.

In experiment 5, the bend in the east coast has been moved further to the south. Panel (a) of Fig. 5.6 shows that, also in this experiment, an arc of strong convergence (marked A) indicates the position of the sea breeze moving inland from this bend. This arc of convergence is prolonged by a line of weaker convergence (marked B) at its northern end. This extension marks the sea-breeze front north of the bend. Horizontal wind shear caused the north-west to south-eastward orientation of this line. By 2200 EST, the west- and east-coast sea breezes have collided and a north-easterly disturbance has formed (marked C). An animation of the low-level divergence field shows that this convergence line has been generated by the collision of the sea breeze north of the bend of the east coast and the west-coast sea breeze. The sea-breeze front from this bend is still visible at the south-eastern end of the north-easterly morning-glory convergence line (marked D). By 0200 EST on 09 October, a distinct NACL (marked E) has been generated by the collision of the west-coast sea breeze and the east-coast sea breeze from north of the bend in the coast line. The north-easterly morning-glory convergence line has propagated further to the south-west. A southerly morning-glory convergence line has formed (marked F) and is visible to the west of the north-easterly morning-glory line. By 0600 EST the convergence lines corresponding to the morning glories have propagated further towards the southern gulf coast and the convergence line corresponding to the NACL has travelled further westward.

In this experiment, the convergence lines corresponding to the north-easterly morning glory and the NACL separate about  $1.5^\circ$  north of the position of the east-coast bend, close to the latitude at which both lines separate in the previous experiment. The insensitivity of the latitude at which the separation occurs to the latitude of the east-coast bend suggests that the existence of such a bend might not be crucial for the separation.

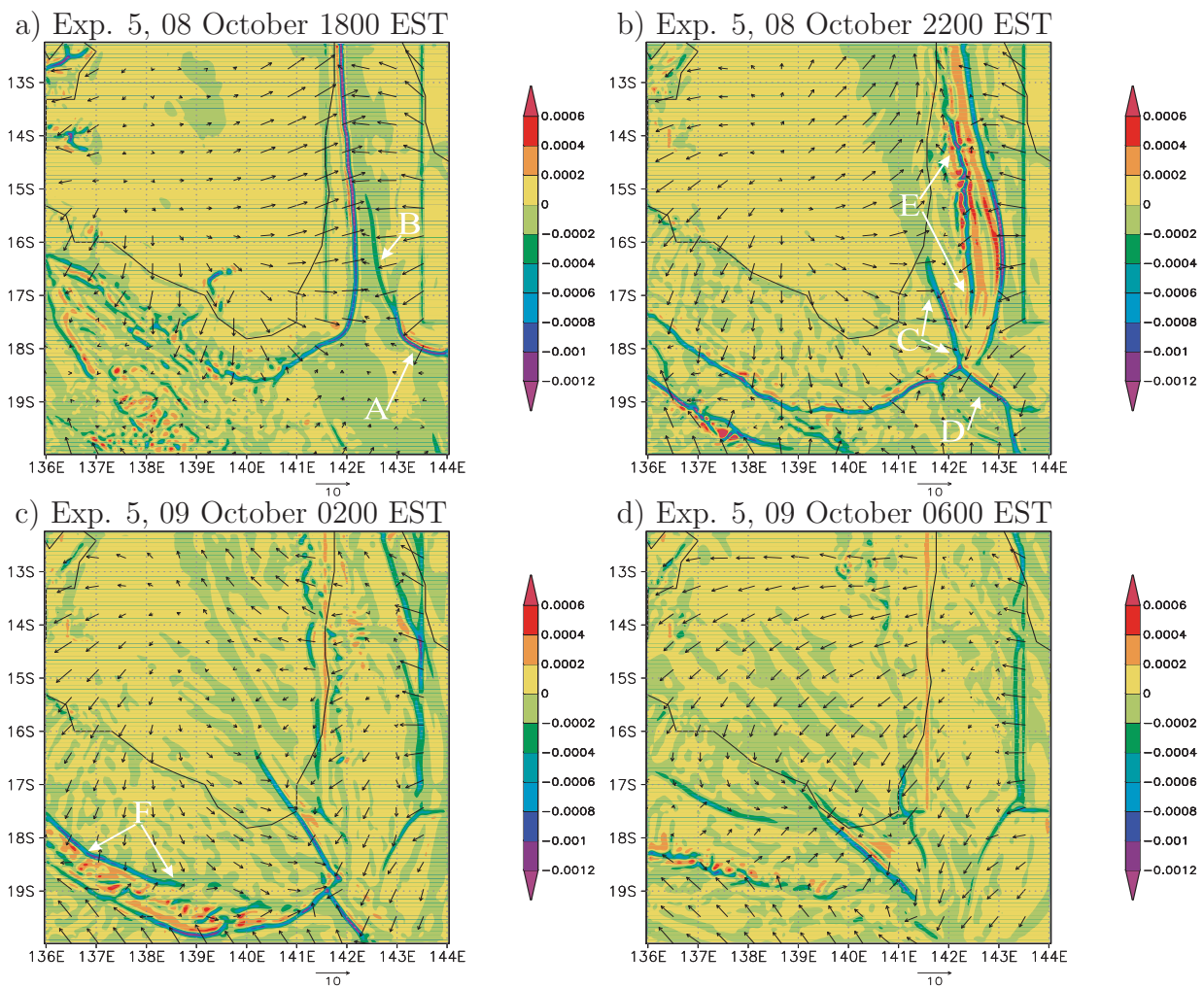


Figure 5.6: Sequence of plots of wind vectors (scale  $10 \text{ m s}^{-1}$  below each panel) and divergence (shaded, unit  $\text{s}^{-1}$ ) at  $\sigma = 0.9975$  for experiment 5 at different times.

Experiment 5 indicated that the separation of the north-easterly morning glory and the NACL might not be caused by the bend in the east coast. The time series of low-level wind divergence in Fig. 5.7 shows that two distinct convergence lines corresponding to the NACL and the north-easterly morning glory form in experiment 6, with a straight east coast. Panel a) shows the gulf- and east-coast sea breezes at 1800 EST on 08 October. The orientation of the convergence lines marking the sea-breeze fronts (in particular the west-coast sea breeze) over the peninsula indicates the presence of a strong horizontal wind shear. By 2200 EST, the two sea breezes have collided over the peninsula, but no separation into two distinct lines is visible by this time. By 0200 EST on 09 October, two distinct convergence lines corresponding to an NACL (marked A, close to the west coast in the north) and a north-easterly morning glory (marked B, crossing the coast line in the south of the peninsula) have formed. A southerly morning glory (marked C) is indicated by the convergence line west of the north-easterly disturbance. By 0600 EST, the convergence line associated with the NACL has moved further over the gulf and the north-easterly morning-glory convergence line has propagated further in south-westerly direction. The convergence line corresponding to the southerly morning glory has almost reached the southern gulf coast. The results of this experiment give further reason for the assumption that the east-coast bend is not the reason for the separation of north-easterly morning glory and NACL.

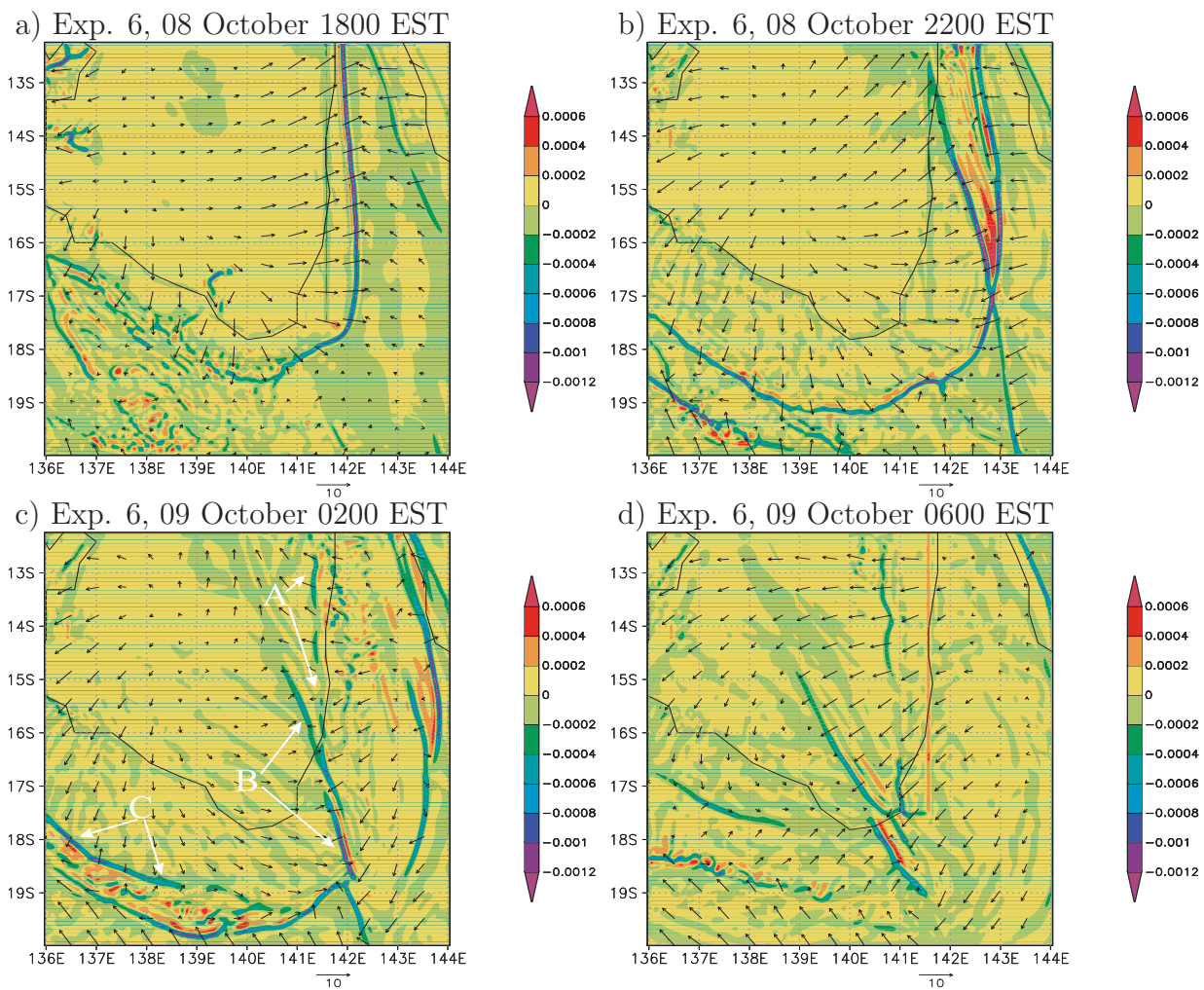


Figure 5.7: Sequence of plots of wind vectors (scale  $10 \text{ m s}^{-1}$  below each panel) and divergence (shaded, unit  $\text{s}^{-1}$ ) at  $\sigma = 0.9975$  for experiment 6 at different times.

The results of experiments 4 to 6 point to the horizontal wind shear as the reason for the separation of the north-easterly morning glory and the NACL. Noonan and Smith (1987) and Smith and Noonan (1998) used a uniform flow and did not find a separate morning-glory and NACL convergence line. To pursue this matter further, an experiment with a uniform easterly flow across the domain was carried out (referred to as experiment 7). The initialisation of this experiment uses a modified version of a program by Dr. Günther Zänagl (personal communication). This program begins with prescribed three-dimensional temperature and relative-humidity field, a prescribed height of the 1000 mb surface, and prescribed surface temperature. The program then calculates the surface pressure and the geopotential field in geostrophic balance with the flow. The Coriolis parameter is set to a constant value (the average value of the largest domain) due to mass conservation considerations. The temperature and relative humidity correspond roughly to the situation at Highbury on 08/09 October. The surface temperature is set to a value of 302 K at 1000 EST, 312 K at 1600 EST, 302 K at 2200 EST and 300 K at 0200 EST. The relative humidity is set to 75 % from the surface to the 800-mb level, then linearly decays to 10 % to the 650-mb layer and remains constant up to the model top. The sea-surface temperature is set to 300 K, corresponding to the temperature of the Coral Sea east of the Cape York Peninsula.

Figure 5.8 shows the low-level divergence and wind vectors at 0200 EST, 16 h after the initial time. A long south-east to north-westward oriented convergence line has formed over the south-eastern part of the gulf. This line resembles a northeasterly morning-glory line in a real-case simulation, but extends much further into the northern gulf. At these latitudes a NACL would have formed in a real case. In this experiment the model has failed to produce a separate line corresponding to a NACL. The line corresponding to a north-easterly morning glory is followed by an other convergence line about  $1^\circ$  to the north-east, which could be interpreted as a line resembling an NACL, but with a different orientation. In the south-western corner of the domain the divergence pattern is rather noisy. In this area, precipitating deep convection has developed in the model, presumably triggered by sea breeze flow over the local orography. A comparison of the sounding for this experiment with ECMWF data showed that the air is moister in this area in the experiment than it is realistic. Nevertheless, the influence of this feature should not have a big influence on the convergence lines over Cape York Peninsula and the eastern Gulf of Carpentaria.

Figure 5.9 shows the relative flow behind the convergence lines resembling a rotated NACL (panel a) and the north-easterly morning glory (panel b) at a height of  $\sigma = 0.965$  and at the same time as figure 5.8. In these calculations the orientation of the line corresponding to a rotated NACL is  $\sim 42^\circ \pm 1^\circ$  and the orientation of the line corresponding to the north-easterly morning glory is  $\sim 30^\circ \pm 1^\circ$ . The speed of the lines is  $\sim 11.4 \pm 0.5 \text{ m s}^{-1}$  and  $\sim 13.4 \pm 0.5 \text{ m s}^{-1}$ , respectively. The plots show a bore-like flow characteristic for both lines at this time. While morning-glory convergence lines appear always to have a bore-like character, the convergence lines corresponding to the NACL appear to not have. Thus, the

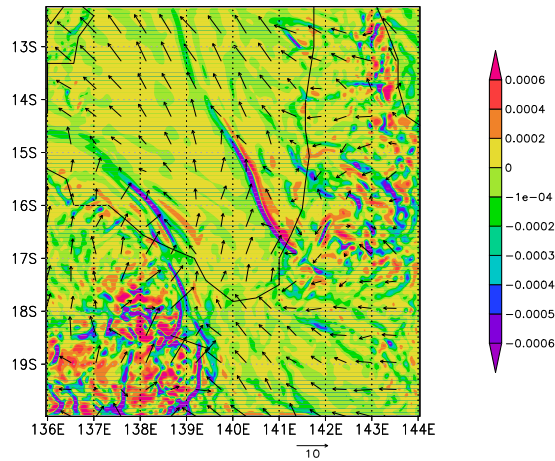


Figure 5.8: Wind vectors (scale  $10 \text{ m s}^{-1}$  below the panel) and divergence (shaded, unit  $\text{s}^{-1}$ ) at  $\sigma = 0.9975$ .

assumption of a formation of a rotated NACL is no longer sustainable. This experiment shows, however, that with uniform flow conditions the MM5 does not produce two distinct lines corresponding to a NACL and a north-easterly morning glory. Rather the model produces a north-easterly morning-glory convergence line which extends exceptionally far into the northern gulf. This result further strengthens the thesis that horizontal wind shear over Cape York Peninsula is the cause for the separation of both lines. The model run for this experiment was terminated after 48 h integration time. On the second day of this simulation, the initially uniform flow over the domain has changed and resembles flow conditions which are comparable to conditions in the real-case simulations. Under these conditions the model produces two distinct lines corresponding to NACL and north-easterly morning glory again.

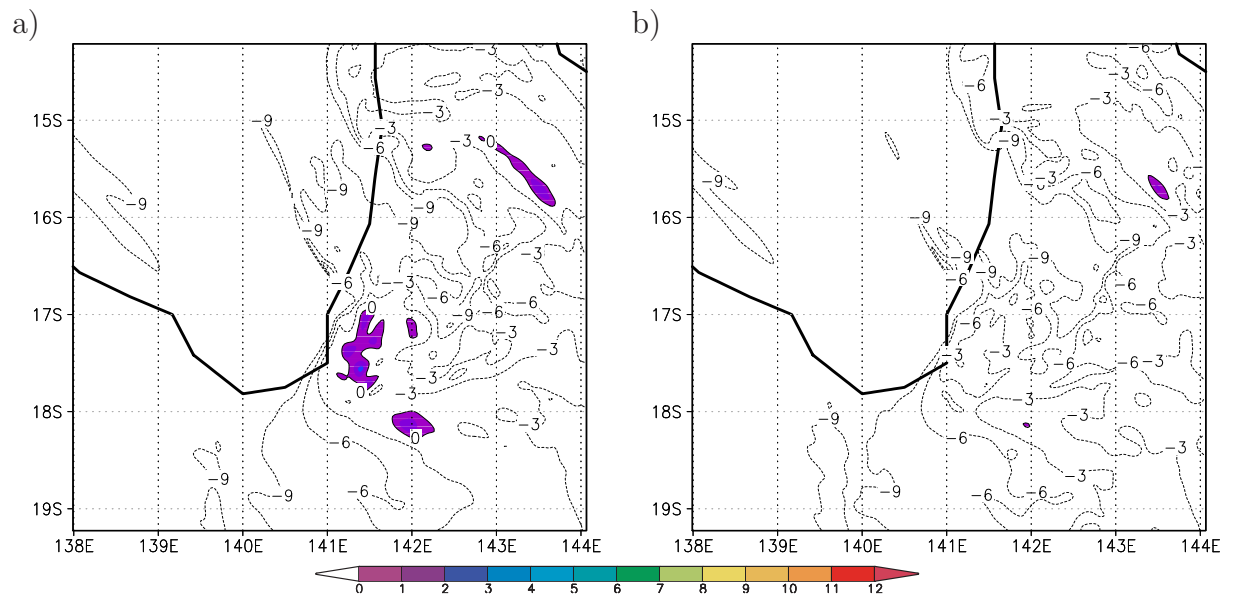


Figure 5.9: Calculations of the relative flow,  $u - c$  (in  $\text{m s}^{-1}$ ), normal to and behind the convergence line resembling a rotated NACL (left panel) and the north-easterly morning glory convergence line (right panel) at  $\sigma=0.965$ . Positive values of  $u - c$  are shaded.

## 5.6 Summary

This chapter sought to investigate the impact of orography in the Gulf of Carpentaria region on morning-glory and NACL convergence lines.

Experiments 1 to 3 were designed to investigate a theory by Porter and Smyth which predicted that the north-easterly disturbance was generated by flow over the northern foothills of the Great Dividing Range. The results of these experiments do not give support to this theory. In contrast, experiment 3 further strengthens the idea that the north-easterly morning glory is generated only by virtue of the collision of the east-coast and west-coast sea breezes. This experiment indicated also that the southerly morning glory is generated in an analogue way when the south-coast sea breeze and a cold front collides. In this experiment, there is no gulf-coast sea breeze and as a consequence neither morning-glory convergence lines nor an NACL form.

Experiments 4 to 6 were designed to study the formation of two distinct convergence lines corresponding to the north-easterly morning glory and an NACL. To this end, the shape of Cape York Peninsula was modified. These experiments show that the bend in the east coast is not the reason for this separation as suggested by the experiments described in Chapter 2. In Experiments 4 and 5 the east coast of the peninsula has a sharp bend at different latitudes. This bend is close to the latitude of the bend in the real coast line in experiment 4 and  $2.8^\circ$  further south in experiment 5. Both lines separate close to the same latitude as described in the case study in Chapter 2. Also in experiment 6, in which the east coast is straight, two distinct convergence lines corresponding to the NACL and the north-easterly morning glory form and separate close to the same latitude.

These experiments raised the possibility that the horizontal wind shear over the peninsula might play a role in the separation of the lines. To investigate this possibility, an experiment (experiment 7) was carried out, in which the model was initialised with a uniform easterly flow. The model did not produce two distinct lines corresponding to a morning glory and an NACL on the first day of this run. However, on the second day, the broadscale flow conditions have changed to stronger horizontal shear of the easterly flow. The model developed two separate lines. This behaviour supports the hypothesis that the horizontal shear is the important factor in producing two separate lines.

## Chapter 6

# Summary and conclusions

I have shown that the MM5 model in the chosen configuration has considerable skill in reproducing most convergence lines corresponding to north-easterly and southerly morning glories, as well as to NACLs. Convergence lines associated with north-easterly morning glories and NACLs form following the collision of the west- and east-coast sea breeze over Cape York Peninsula in the simulations and most probably in reality. The convergence lines corresponding to southerly morning glories are generated following the collision of the south-coast sea breeze and a cold front approaching from the south. This front is generated by strong ageostrophic flow towards a trough line during night and forms along this line. The southerly disturbances are often followed by a dry line, which is initially located north of the inland trough and which marks the maximum inland penetration of the sea breeze south of the gulf. The predicted position of this line and its northward movement agree well with the observations.

The simulations show for the first time the generation of two distinct lines corresponding to a north-easterly morning glory and an NACL. While the former develops out of the east-coast sea-breeze front on Cape York Peninsula south of about  $14^{\circ}\text{S}$ , the latter forms from the same sea-breeze front to the north of this latitude. At this position, there is a bend in the coast line which was initially assumed to cause the separation of the north-easterly morning glory and the NACL.

In the cases studied, the relative flow behind the sea-breeze fronts and the nocturnal cold front is that of a gravity current. The morning glory lines studied here always evolved into a bore-like disturbance. The convergence line corresponding to the NACL retains the character of a gravity current. The model failed to reproduce the south-easterly disturbance which was observed on 09 October, but it produced a southerly in its place. The model also failed to capture the southerly morning glory of 04 October, but it produced a convergence line about 100 km south of the observed position. The cause for this shortcoming may be attributable to the inaccurate position of the trough line over the data-sparse region south of the gulf in the initial data provided by the ECMWF.

In one of the cases, no cloud lines were observed in satellite images and no disturbances were recorded at AWS stations except for the two northernmost stations in the station network. Both of these recorded a north-easterly disturbance, which was, indeed, captured by the model. Moreover, the continued propagation far into the southerly gulf region was inhibited by strong southerly winds. The model results in this case agree with the observations and suggest that north-easterly disturbances generally form after the collision of the west- and east-coast sea breeze over Cape York Peninsula, but do not always propagate far into the southern gulf region.

The sensitivity of the convergence lines to the choice of boundary-layer parameterisation schemes were examined in Chapter 3. The schemes were subdivided into three groups according to the accuracy with which the lines were forecasted, the coherence of the lines, and the correlation of surface pressure with measured values during the GLEX experiment. The group that performs best includes the Blackadar, Eta and MRF schemes. Significantly, all these schemes take into account countergradient fluxes in their daytime convective module. The MRF scheme was marginally superior to the other two based on these criteria. For this reason, the MRF scheme was chosen for all the experiments described in the earlier chapters. The results highlight the importance of including the counter gradient fluxes in the boundary layer schemes for numerical studies of low-level convergence lines.

The sensitivity of the calculations to variations of soil moisture were examined in Chapter 4. It was found that the speed of the sea-breeze fronts and of the morning-glory and NACL convergence lines decrease linearly with increasing soil moisture, while the speed of the cold front and of the dry line increases linearly with increasing soil moisture. An "optimum" soil moisture could not be found and the problems in finding such a value were discussed. However, the correlation between the mean sea-level pressure at the stations in the model and the observations increased quadratically with decreasing soil moisture. Since the lowest possible soil moisture values are not realistic, the value adapted from the Australian Bureau of Meteorology was chosen for the soil moisture. This value is evidently an important consideration for future experiments.

The influence of the height of the orography and the shape of the coast lines was studied in Chapter 5. No systematic dependency of the intensity or speed of morning-glory or NACL convergence lines on the height of the orography was found. An experiment in which the Gulf of Carpentaria was filled with land of one metre height above sea level was performed to study the effect of the gulf-coast sea breeze. In this case, no morning-glory or NACL convergence lines were generated. These results cast doubt on a theory by Porter and Smyth, who suggested that orographic forcing was the key mechanism for the formation of morning-glory waves.

Three experiments over flattened orography and with different shapes of the Cape York Peninsula were performed to investigate the separation of the NACL from the north-

easterly morning-glory convergence line. In contrast to the model results discussed in Chapter 2, this set of experiments showed that both lines also separate with a straight east coast. Instead of the bend in the coast line, horizontal wind shear was proposed as the mechanism which separates both lines. This idea was supported by the results of an experiment, in which the model was initialised with a uniform easterly flow across the domain. In this experiment, the model produced only a single convergence line on the first day of the simulation. Only the convergence line corresponding to the north-easterly disturbance was produced and this line extended far into the area where the NACL usually forms. However, on the second day, the model developed a flow pattern over Cap York Peninsula, which generated two separate lines corresponding to these two cloud lines.

# Appendix A

## List of symbols

Only the principal symbols are listed. Symbols formed by adding primes, overbars, or subscripted indices are not generally listed separately and are explained in the text where they appear.

$f$	Coriolis parameter ( $\equiv 2\Omega \sin \lambda$ )
$g$	Gravity
$k$	Von-Karman constant
$m$	Map-scale factor
$p$	Pressure
$q$	Water vapour mixing ratio
$t$	Time
$u$	x-component (eastward) velocity
$v$	y-component (northward) velocity
$w$	z-component (upward) velocity
$x$	Eastward distance
$y$	Northward distance
$z$	Upward distance
$A$	Arbitrary scalar
$D$	Horizontal diffusion
$K$	Eddy exchange coefficient
$L$	Monin-Obukhov length
$Q$	Heat
$S$	Vertical wind shear
$T$	Temperature
$c_{def}$	Horizontal deformation
$c_p$	Specific heat of dry air at constant pressure
$c_v$	Specific heat of dry air at constant volume
$r_{earth}$	Radius of the earth
$z_h$	Height of the mixed layer

---

$K_H$	Horizontal diffusion coefficient
$K_z$	Eddy diffusivity
$R_d$	Gas constant for dry air
$Ri$	Richardson number
$Ri_b$	Bulk-Richardson number
$Ri_c$	Critical Richardson number
$\vec{u}$	Three-dimensional velocity in height-coordinates
$\alpha$	Arbitrary prognostic variable
$\gamma$	Ratio of specific heats ( $\equiv c_p/c_v$ )
$\theta$	Potential temperature
$\lambda$	Latitude
$\rho$	Density
$\sigma$	Vertical coordinate
$\phi$	Longitude
$\Omega$	Angular velocity of the earth
$\wedge$	Logical and

## Appendix B

### Table of $\sigma$ -levels

To give the reader a rough idea of the height and pressure levels of different  $\sigma$ -levels, the  $\sigma$ -levels are first converted to pressure-levels, and then converted to height in metres assuming fixed surface pressure and temperature and a fixed lapse rate.

The pressure levels are calculated from  $\sigma$ -levels based on

$$\sigma = (p - p_t)/(p_s - p_t), \quad (\text{B.1})$$

where the pressure at the model top is  $p_t = 100$  mb and at the pressure at the surface is  $p_s = 1000$  mb.

The heights above mean sea-level are approximated from pressure levels based on

$$p(h) = p_s \left( 1 - \frac{\Gamma h}{T_s} \right)^{\frac{Mg}{R\Gamma}}, \quad (\text{B.2})$$

where  $M = 0.02896$  kg mol<sup>-1</sup> is the mean molar mass of the atmosphere,  $R = 8.314$  J K<sup>-1</sup> mol<sup>-1</sup> is the universal gas constant,  $g$  is the acceleration due to gravity,  $T_s = 275$  K is the surface temperature and  $\Gamma = 5$  K km<sup>-1</sup> being the lapse rate. Surface pressure, surface temperature and lapse rate are chosen to be consistent with the MM5 initialization.

---

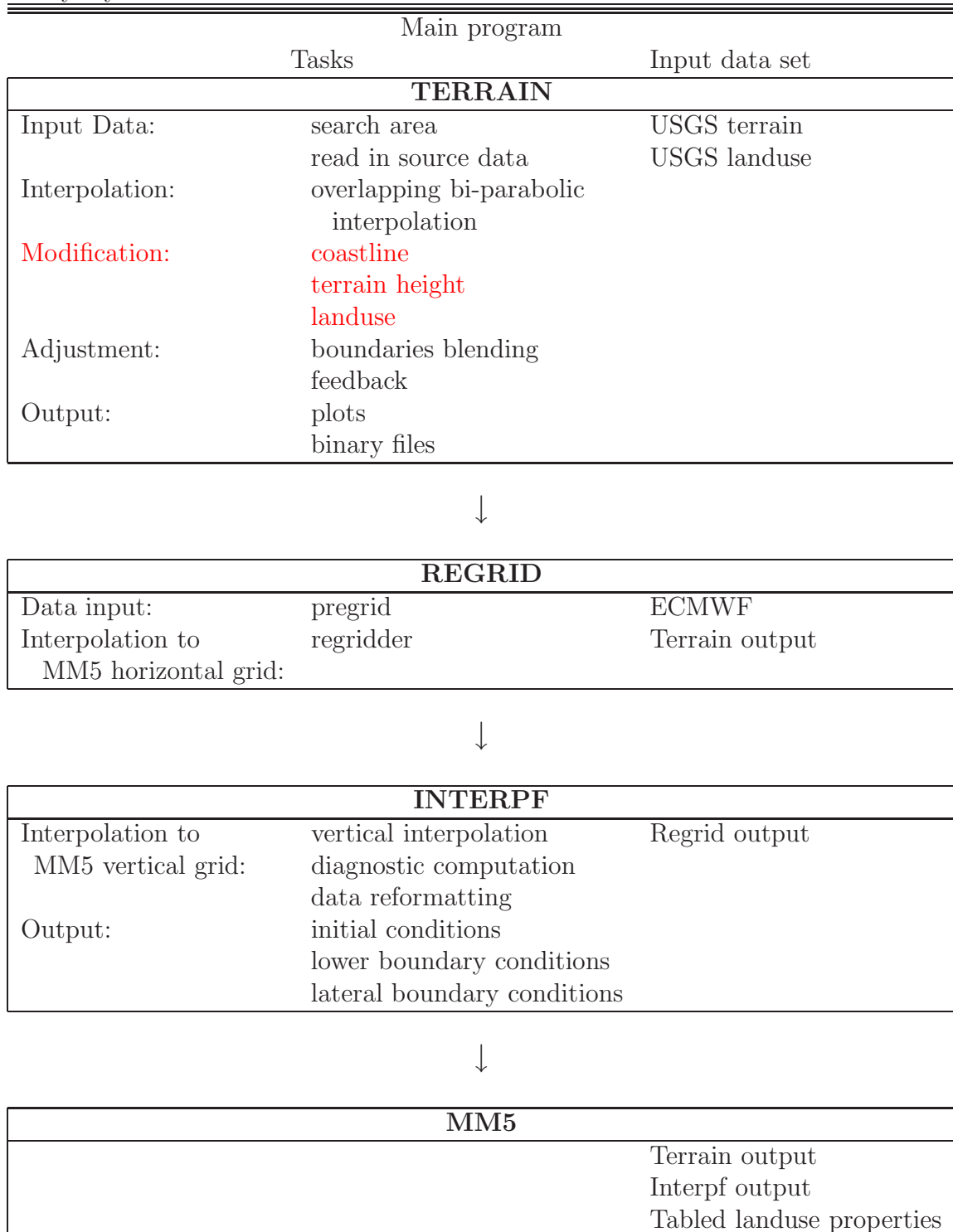
$\sigma$ -level	pressure-level (mb)	height above mean sea-level (m)
0.000	100.0	15737.1
0.150	235.0	10506.2
0.300	370.0	7449.4
0.450	505.0	5234.3
0.490	541.0	4730.1
0.530	577.0	4253.8
0.570	613.0	3802.2
0.610	649.0	3372.8
0.650	685.0	2963.2
0.690	721.0	2571.5
0.730	757.0	2196.3
0.770	793.0	1835.9
0.810	829.0	1489.3
0.850	865.0	1155.3
0.890	901.0	832.9
0.910	919.0	675.9
0.930	937.0	521.4
0.950	955.0	369.5
0.960	964.0	294.4
0.970	973.0	219.9
0.980	982.0	146.0
0.990	991.0	72.7
0.995	995.5	36.3
1.000	1000.0	0.0

## Appendix C

# Modified orography with MM5 and its preprocessors

Table C.1 shows a flow chart of the MM5 preprocessors (programs which produce the necessary data files for initial- and boundary conditions) and highlights the implementations in one of the main subroutines in the TERRAIN program (`TERRAIN/src/terdrv.F`) which have been done to the end of terrain modification. While changes to the coastline and to the land-use fields do not have a large impact on the MM5 initialization (only the land-surface properties change), the variation of the terrain elevation plays a larger role since a different orography is present in the initial data from the ECMWF model and in the MM5 model. Flow patterns in the initial data might be caused by orography in the ECMWF model which is not present in the MM5 run. While changed orography may lead to unrealistic flow patterns in the model, the initialization itself is rather uncomplicated. The INTERPF program interpolates the ECMWF data (in pressure coordinates) to the terrain-following  $\sigma$ -coordinates in MM5. Where the inconsistency between the orography in the ECMWF and the MM5 model causes missing data in the lower pressure surfaces, INTERPF extrapolates the missing data to the lowest model layers. After inter- and extrapolation, INTERPF removes the integrated mean divergence to reduce the amount of initial-condition noise that the ECMWF data contains. By doing this, the orographic effects (orography usually causes noisy divergence patterns) are reduced also. The base state and vertical velocity for the initial data are computed after the mean divergence have been removed.

Table C.1: Flow chart of the MM5 preprocessors, red text highlights implementations coded by myself.



The experiments described in Chapter 5 showed that the model adjusts to the changed orography within the first few hours of integration. The use of the land- and sea-surface temperature (SST) for the daily mean at the lower boundaries could be problematic where the model surface has been changed from water to land, but the experiment results show that the surface temperature is initialised with values resembling the temperature at positions of land in the ECMWF data set. These temperatures over land are about five to ten °C warmer than over the ocean. Only the low-level moisture field is initialized with too high values (water vapour mixing ratio  $q \sim 17$  g/kg) over these artificial land areas, but the moisture adjusts to values which are more typical for a land area after about 5 h of integration ( $q \sim 10$  g/kg).



# Bibliography

- Betts, A. K. (1973). Non-precipitating cumulus convection and its parameterization. *Quart. J. Roy. Meteor. Soc.*, 99:178–196.
- Blackadar, A. K. (1976). Modeling the nocturnal boundary layer. *Third Symp. on Atmospheric Turbulence, Diffusion and Air Quality*, pages 46–49.
- Blackadar, A. K. (1978). Modelling pollutant transfer during daytime convection. *Fourth Symp. on Atmospheric Turbulence, Diffusion and Air Quality*, pages 443–447.
- Blackadar, A. K. (1979). High resolution models of the planetary boundary layer. *Advances in Environmental Science and Engineering*, 1:50–52.
- Burk, S. D. and Thompson, W. T. (1982). Operational Evolution of a Turbulence Closure Model Forecast System. *Mon. Wea. Rev.*, 110:1535–1543.
- Christie, D. R. (1989). Long Nonlinear waves in the Lower Atmosphere. *J. Atmos. Sci.*, 46:1462–1491.
- Clark, T. L. (1977). A small scale numerical model using a terrain following coordinate transformation. *J. Comput. Phys.*, 24:186–215.
- Clarke, R. H. (1983). Fair weather nocturnal inland wind surges and atmospheric bores: Part I Nocturnal wind surges. *Aust. Met. Mag.*, 31:133–145.
- Clarke, R. H. (1984). Colliding sea-breezes and the creation of internal atmospheric bore waves: two-dimensional numerical studies. *Aust. Met. Mag.*, 32:207–226.
- Clarke, R. H. (1986). Several atmospheric bores and cold fronts over southern Australia. *Aust. Met. Mag.*, 34:65–76.
- Crook, N. A. (1986). The effect of ambient stratification and moisture on the motion of atmospheric undular bores. *J. Atmos. Sci.*, 43:171–181.
- Crook, N. A. and Miller, M. J. (1985). A numerical and analytical study of atmospheric undular bores. *J. Atmos. Sci.*, 111:225–242.
- Dudhia, J. (1989). Numerical study of convection observed during the winter monsoon experiment using a mesoscale two-dimensional model. *J. Atmos. Sci.*, 46:3077–3107.

- ECMWF. Tiled ECMWF Surface Scheme of Exchange processes at the Land surface. [http://www.ecmwf.int/products/data/technical/soil/discret\\_soil\\_lay.html](http://www.ecmwf.int/products/data/technical/soil/discret_soil_lay.html).
- Egger, J. (1983). The Morning Glory: A Nonlinear Wave Phenomenon. In Lilly, D. K. and Gal-Chen, T., editors, *Theories, Observations and Models*, pages 339–348. D. Reidel Publishing Company.
- Egger, J. (1984). On the Theory of the Morning Glory. *Beitr. Phys. Atmosph.*, 57:123–134.
- Egger, J. (1985). Die Berliner Nebelwellen. *Meteorol. Rdsch.*, 38:103–108.
- Geophysical Memoirs (1914). The South Wales tornado of October 27, 1913, with a note on remarkable pressure oscillations observed on Aug. 14, 1914. volume 11, pages 1–17. Meteorological Office, London, Neill and Co., Edinburgh.
- Goler, R. A. (2004). *Numerical model of cloud lines over Cape York Peninsula*. PhD thesis, Centre for Dynamical Meteorology and Oceanography, Monash University, Melbourne.
- Goler, R. A. and Reeder, M. J. (2004). The generation of the morning glory. *J. Atmos. Sci.*, 61:1360–1376.
- Grell, G. A. (1993). Prognostic Evaluation of Assumptions Used By Cumulus Parameterizations. *Mon. Wea. Rev.*, 121:764–787.
- Grell, G. A., Dudhia, J., and Stauffer, D. (1995). A Description of the 5th Generation Penn State/NCAR Mesoscale Model (MM5). Technical Report 398, NCAR.
- Haase, S. and Smith, R. K. (1989). The Numerical Simulation of Atmospheric Gravity Currents. Part II. Environments With Stable Layers. *Geophys. Astrophys. Fluid Dynamics*, 46:35–51.
- Hess, R. (2001). Assimilation of screen-level observations by variational soil moisture analysis. *Meteorology and Atmospheric Physics*, 77:145–154.
- Hong, S.-Y. and Pan, H.-L. (1996). Nonlocal Boundary Layer Vertical Diffusion in a Medium-Range Forecast Model. *Mon. Wea. Rev.*, 124:1322–2339.
- Jackson, G. E., Smith, R. K., and Spengler, T. (2002). The prediction of low-level mesoscale convergence lines over northeastern Australia. *Aust. Met. Mag.*, 51:13–23.
- Janjić, Z. I. (1990). The Step-Mountain Coordinate: Physical Package. *Mon. Wea. Rev.*, 118:1429–1443.
- Janjić, Z. I. (1994). The Step-Mountain Eta Coordinate Model: Further Developments of Convection, Viscous Sublayer, and Turbulence Closure Schemes. *Mon. Wea. Rev.*, 122:927–945.

- Liu, C. and Moncrieff, M. W. (1996). A numerical study of the effects of ambient flow and shear on density currents. *Mon. Wea. Rev.*, 124:2282–2303.
- Marquardt, D. W. (1963). An algorithm for least squares estimation of nonlinear parameters. *J. Indust. Appl. Math.*, 11:431–441.
- McNider, R. T. and Pielke, R. A. (1981). Diurnal boundary-layer development over sloping terrain. *J. Atmos. Sci.*, 38:2198–2212.
- Mellor, G. L. and Yamada, T. (1974). A Hierarchy of Turbulence Closure Models for Planetary Boundary Layers. *J. Atmos. Sci.*, 31:1791–1806.
- Mesinger, F. and Arakawa, A. (1976). Numerical Methods used in Atmospheric Models. volume 14, page 64 pp. WMO/ICSU Joint Organizing Committee.
- Miles, J. W. (1980). Solitary waves. *Annu. Rev. Fluid Mech.*, 12:11–43.
- Noonan, J. A. and Smith, R. K. (1985). Linear and Weakly Nonlinear Internal Wave Theories Applied to "Morning Glory" Waves. *Geophys. Astrophys. Fluid Dynamics*, 33:123–143.
- Noonan, J. A. and Smith, R. K. (1986). Sea-Breeze Circulations over Cape York Peninsula and the Generation of Gulf of Carpentaria Cloud Line Disturbances. *J. Atmos. Sci.*, 43:1679–1693.
- Noonan, J. A. and Smith, R. K. (1987). The generation of North Australian cloud lines and the 'morning glory'. *Aust. Met. Mag.*, 35:31–45.
- Physick, W. L., Noonan, J. A., McGregor, J. L., Hurley, P. J., Abbs, D. J., and Manins, P. C. (1994). LADM: A Lagrangian Atmospheric Dispersion Model. Technical report, CSIRO Division of Atmospheric Research. Tech. Paper 24, 137 pp. [Available from The Chief, CSIRO Division of Atmospheric Research, Private Bag 1, Mordialloc, Victoria, 3195, Australia.
- Pielke, R. A. (1974). A three-dimensional model of the sea breezes over south florida. *Mon. Weath. Rev.*, 102:115–139.
- Porter, A. and Smyth, N. F. (2002). Modelling the morning glory of the Gulf of Carpentaria. *J. Fluid Mech.*, 454:1–20.
- Puri, K., Dietachmayer, G. S., Mills, G. A., Davidson, N. E., Bowen, R. A., and Logan, L. W. (1998). The new BMRC Limited Area Prediction System, LAPS. *Aust. Met. Mag.*, 47:203–223.
- Reeder, M. J., Christie, D. R., Smith, R. K., and Grimshaw, R. (1995). Interacting "Morning Glories" over Northern Australia. *Bull. Amer. Met. Soc.*, 76(7):1165–1171.

- Reeder, M. J. and Smith, R. K. (1998). Mesoscale meteorology. In Koroly, D. J. and Vincent, D. G., editors, *Meteorology of the Southern Hemisphere*, volume 27, chapter 5, pages 201–241. American Met. Soc., 45 Beacon Street, Boston, Massachusetts 02108.
- Shafran, P. C., Seaman, N. L., and Gayno, G. A. (2000). Evaluation of Numerical Predictions of Boundary Layer Structure during the Lake Michigan Ozone Study. *Journal of Applied Met.*, 39:412–426.
- Simpson, J. E. (1997). *Gravity Currents in the Environment and in the Laboratory*, second edition. Cambridge University Press.
- Skyllingstad, E. D. (1991). Critical layer effects on atmospheric solitary and cnoidal waves. *J. Atmos. Sci.*, 48:1613–1624.
- Smagorinsky, J., Manabe, S., and Holloway, J. L. (1965). Numerical results from a nine level general circulation model of the atmosphere. *Mon. Wea. Rev.*, 93:727–768.
- Smith, R. K., Coughlan, M. J., and Lopez, J.-L. (1986). Southerly Nocturnal Wind Surges and Bores in Northwestern Australia. *Mon. Weath. Rev.*, 114:1501–1518.
- Smith, R. K., Crook, N. A., and Roff, G. (1982). Morning Glory: an extraordinary atmospheric undular bore. *Quart. J. Roy. Met. Soc.*, 198:937–956.
- Smith, R. K. and Noonan, J. A. (1998). Generation of Low-Level Mesoscale Convergence Lines over Northeastern Australia. *Mon. Wea. Rev.*, 126:167–185.
- Smith, R. K. and Page, M. A. (1985). Morning glory wind surges and the Gulf of Carpentaria cloud line of 25-26 October 1984. *Aust. Met. Mag.*, 33:185–194.
- Smith, R. K., Reeder, M. J., May, P., and Richter, H. (2006). Low-level convergence lines over northeastern Australia. I. Southerly disturbances. *Mon. Wea. Rev. (in press)*.
- Smith, R. K., Reeder, M. J., Tapper, N. J., and Christie, D. R. (1995). Central Australian Cold Fronts. *Mon. Wea. Rev.*, 123(1):16–38.
- Spengler, T., Reeder, M. J., and Smith, R. K. (2005). The Dynamics of Heat Lows in Simple Background Flows. *Quart. J. Roy. Met. Soc.*, *in press*, ??
- Stull, R. B. (1988). *An Introduction to Boundary Layer Meteorology*, chapter 6. Kluwer Academic Publishers.
- Therry, G. and Lacarrere, P. (1983). Improving the eddy kinetic energy model for planetary boundary layer description. *Bound.-Layer Meteor.*, 25:63–88.
- Troen, I. B. and Mahrt, L. (1986). A Simple Model of the Atmospheric Boundary Layer; Sensitivity to Surface Evaporation. *Boundary-Layer Meteorology*, 37:129–148.

- Weinzierl, B., Smith, R. K., Reeder, M. J., and Jackson, G. (2006). MesoLAPS predictions of low-level convergence lines over northeastern Australia. *Submitted to Wea. Forecasting in April 2006, ????*
- Zhang, D. and Anthes, R. A. (1982). A High-Resolution Model of the Planetary Boundary Layer - Sensitivity Tests and Comparisons with SESAME-79 Data. *J. of appl. Met.*, 21:1594–1609.



# Acknowledgement

I am grateful to the following people and institutions:

- Prof. Roger Smith for supervising me with this thesis, for supporting my ideas, for his patience with my writing and his generosity when writing something supportive for me
- Michael Riemer for always being open for a professional discussion and for playing a game of darts with me when I needed some distraction
- My parents for giving me all the support I needed
- Dr. Wolfgang Ulrich for being a brilliant teacher and for always knowing a solution
- Heinz Lösslein for being not too impatient with me when my data sets once again grew too large and for generally supplying my computational needs as much as possible
- My colleagues Andreas Pfeiffer, Sang Van Nguyen, Seol Eun Shin and Dr. Günther Zängl for helping me with setting up the model
- My Girlfriend Katharina for always giving me support
- The Ludwig-Maximilians University for giving me financial support
- The Royal Meteorological Society for enabling me to visit important research sites in Australia



# Curriculum Vitae

- 14.05.1977 : Born in Reinbek
- 1983-1987 : Elementary school of the Oberstadtschule in Geesthacht
- 1987-1996 : Attendance of the Otto-Hahn-Gymnasium in Geesthacht
  - 1993 : Practical in the branch for central computation at the GKSS
  - 1995 : Practical at the Dacom GmbH
  - 1996 : General qualification for university entrance
- 1996-1997 : Basic military service at the Panzerpionierkompanie 400 in Hagenow, function as confidant, commander of a mine launcher
- 1997-2003 : Studies in meteorology at the Meteorological Institute Munich
  - 1999 : Intermediate diploma
- Since 2000 : Member of the German Meteorological Society
  - 2000 : Gliding-meteorological practical in Coburg
  - 2000 : Practical at the geophysical consulting service of the light aircraft regiment 6 in Hohenlockstedt
  - 2001 : Studies for one semester at the University of Reading in England
  - 2002 : Cooperation with the Vertikator projekt
  - 2002-2003 : Diplomathesis (in German, English version of the introduction and conclusions also available), subject: "Numerical extension of a tropical cyclone model formulated in sigma-coordinates to a staggered grid", supervision by Dr. Wolfgang Ulrich
    - 2003 : Degree with the diploma in meteorology
    - 2003 : Preparations for the DROFLOCODS-projekt
    - 2003 : Work on projects associated with the Gulf Lines Experiment (GLEXP), model simulations with MM5
- Since 2003 : Ph.D. Student, subject:"Numerical Simulations of low-level convergence Lines over north-eastern Australia", supervised by Prof. Roger K. Smith and financed with the aid of a scholarship granted by the Ludwig-Maximilians-University Munich
  - 2004 : Award:"The Atmospheric Prize" by the Australian Meteorological and Oceanographic Society for an excellent student paper presentation
  - 2005 : Visit at the Regional Office of the Australian Bureau of Meteorology in Darwin and at the Centre for Dynamical Meteorology and Oceanography at Monash University in Melbourne, financed with the aid of a "Rupert Ford

Travel Award” from The Royal Meteorological Society.